# RADIATION RESPONSE OF OXIDE DISPERSION STRENGTHENED ALLOY

A Dissertation

by

TIANYI CHEN

Submitted to the Office of Graduate and Professional Studies of
Texas A&M University
in partial fulfillment of the requirements for the degree of

DOCTOR OF PHILOSOPHY

| | |
|---|---|
| Chair of Committee, | Lin Shao |
| Committee Members, | Sean M. McDeavitt |
| | Pavel V. Tsvetkov |
| | Xinghang Zhang |
| Head of Department, | Yassin A. Hassan |

December 2015

Major Subject: Nuclear Engineering

# ABSTRACT

Ferritic-martensitic (F/M) steels are known to have greater resistance to void swelling, higher thermal conductivities and lower thermal expansion coefficients than austenitic steels do. The strength and swelling resistance of F/M alloys can be further improved through adding fine dispersions of various yttria oxides. The majority of such oxide-dispersion-strengthened (ODS) alloys introduce dispersoids in ferrite phases. However, previous studies have shown that in the absence of dispersoids, the ferrite phase is significantly less swelling resistant than the tempered martensite phase.

A dual-phase 12Cr ODS alloy with improved corrosion and oxidation resistance exhibits promising microstructural stability and void swelling resistance under 3.5 MeV $Fe^{2+}$ ion irradiation at elevated temperatures. Dispersoids were originally present in both ferrite and tempered martensite grains, with the latter having a wider range of dispersoid sizes. In both phases dispersoids larger than 10 nm in diameter are incoherent with the matrix, while smaller dispersoids exhibit coherency. Beyond radiation damage of 60 displacements per atom (dpa), dispersoids in both phases appear to approach a near-identical equilibrium size, which depends on irradiation temperature. The evolution of dispersoids under irradiation was found to be related to the interface configuration. Grain morphology was found to be stable under irradiation up to a peak dpa of 800. Compared to other ferritic-martensitic alloys, the ion-induced swelling of this alloy is quite low, arising from swelling resistance associated with both tempered martensite and dispersoids in both phases. The swelling in tempered martensite is an order of magnitude less than in the ferrite

phase.

# DEDICATION

Dedicated to:

My dear parents, for all their love and support and everything they have offered to me.

My dear Luanjing, who is not only a loving girlfriend but also a great companion and best friend.

# ACKNOWLEDGEMENTS

I would like to give my sincere gratitude and respect to my advisor and committee chair, Dr. L. Shao. Ever since I came to know him in 2010, I've been impressed by his hard work on building up our group and laboratory, as well as leading and helping everyone of the group. He encouraged me and many of his other students to think critically and independently, take responsibilities and chances, and collaborate seamlessly. It is in the past five years working with him that I found my interest in research, became a better researcher with expertise, and gained stronger personality. I am so glad and proud to be working with him. His guidance will always influence and help me as researcher in the future.

I would like to offer great thanks to Dr. F.A. Garner, who worked with me on the projects related to this dissertation. He educated and inspired me with his endless knowledge in the nuclear material field. He also makes full use of every chance to help me to become a more professional researcher. He helped me to improve scientific writing, presentation skills, communication skills in science society, etc. I feel so honored that I had a chance to work with him when pursuing my Ph.D.

Thanks to Dr. S. Ukai for providing the material and discussing with me regarding material designing and fabrication.

Thanks to Dr. X. Zhang, who is always very helpful whenever I go for advice from him. He provided me with great knowledge related to material science and TEM analysis. I would also like to acknowledge my committee members, Dr. S. McDeavitt and Dr. P. Tsvetkov, who provided very inspiring advice on my project and broadened my knowledge to make me see the big picture.

I would also thank Dr. Y. Bisrat, Dr. A. Holzenburg, Dr. H. Kim and X. Wang who assisted me to carry out the experiment, provided me a lot of advice on experiment design, and provided access to experiment instruments.

Finally, thanks to my dear colleagues, especially E. Aydogan, Dr. D. Chen, J. Gigax, H. Kim, P. Lloyd and J. Wang, who offered me invaluable help during my research.

# NOMENCLATURE

| | |
|---|---|
| ODS | Oxide Dispersion Strengthened |
| SFR | Sodium-cooled Fast Reactor |
| GFR | Gas-cooled Fast Reactor |
| LFR | Lead-Cooled Fast Reactor |
| VHTR | Very High Temperature Reactor |
| SCWR | Supercritical Water Reactor |
| MSR | Molten Salt Reactor |
| U | Uranium |
| Pu | Plutonium |
| F/M | Ferritic-Martensitic |
| Fe | Iron |
| Ni | Nickel |
| Cr | Chromium |
| dpa | Displacements per Atom |
| He | Helium |
| C | Carbon |
| FCC | Face-Centered-Cubic |
| BCC | Body-Centered-Cubic |
| BCT | Body-Centered Tetragonal |
| CCT | Continuous Cooling Transformation |
| MD | Molecular Dynamics |
| SIA | Self Interstitial Atom |
| FIB | Focused Ion Beam |

| | |
|---|---|
| SEM | Scanning Electron Microscope |
| TEM | Transmission Electron Microscope |
| TAMU | Texas A&M University |
| SNICS | Source of Negative Ions by Cesium Sputtering |
| Ar | Argon |
| APT | Atom Probe Tomography |
| PSD | Position Sensitive Detector |
| HRTEM | High Resolution Transmission Electron Micrograph |
| EDS | Energy-Dispersive X-ray Spectroscopy |
| EELS | Electron Energy-Loss Spectroscopy |
| BF | Bright Field |
| DF | Dark Field |
| O | Oxigen |
| Ti | Titanium |
| Y | Yttrium |
| WBDF | Weak-beam Dark Field |
| Pt | Platinum |
| GIS | Gas Injection System |

TABLE OF CONTENTS

Page

LIST OF FIGURES

FIGURE Page

LIST OF TABLES

# 1. INTRODUCTION AND BACKGROUND

This chapter provides a general introduction to the topic of this dissertation: Oxide Dispersion Strengthened (ODS) alloys that will be used as cladding/structural material in Generation IV reactors. The introduction starts with an overview of the increasing demand of energy world-widely, and the role nuclear power would play to meet the energy need. As a result of the need to being more efficient and producing less nuclear waste, the challenges to nuclear materials becomes a critical issue for Generation IV reactors, which were discussed in the following section. In the last section of this section, the concept of ODS alloy was provided as a potential solution to the challenges to cladding/structural materials in Generation IV fast reactors.

## 1.1 Generation IV Reactors

### *1.1.1 Overview*

The development of technologies and the increase in populations are always requiring a larger supply of energy. Meanwhile, to reduce pollution as well as the amount of greenhouse gases emission, clean energy is on demand instead of traditional fossil fuel energies. Although the ideas of polar energy and wind energy are popular and seems promising, the resource is limited by natural and geological conditions; in addition, they are not that reliable to provide energy constantly.

Given the advantages of low cost, high efficiency and less limitations from geology and weather conditions, nuclear power is certainly a necessary part of current and future energy sources. Currently, nuclear power is providing more than 16% of the total energy of the world, and approximately 20% of the energy in the U.S. In

countries such as France and Hungary, nuclear power is providing more than 50% of their total electricity supply.

With an annual increase rate of 1.6% in worldwide electricity demand, the power demand will be doubled by the year of 2060. This provides opportunities as well as challenges to nuclear energy. To being able to supply energy more efficiently, concepts of Generation IV reactors have been proposed with the the following advantages:
First, the energy yield from the same amount of nuclear fuel is proposed to increase by 100 times.
Second, Generation IV reactors will potentially have the ability to consume existing nuclear waste for energy.
Third, the amount of high-level waste produced will be greatly reduced.

Three fast reactors and three thermal reactors have been selected as the most promising candidates to meet the goals of the Generation IV initiative. They are: Sodium-cooled Fast Reactor (SFR), Gas-cooled Fast Reactor (GFR), Lead-cooled Fast Reactor (LFR), Very High Temperature Reactor (VHTR), Supercritical Water Reactor (SCWR) and Molten Salt Reactor (MSR). Some details of Generation IV reactors can be found in Table 1.1 [24].

In the past decades, more research have been put into two types of Generation IV reactors, i.e., VHTR and SFR, than the rest of Generation IV reactor candidates, primarily because of the large amount of historical effort associated with technologies related to VHTR and SFR. In the following subsections, more details about these two types of reactor will be given, not only due to the more systematic knowledge

Table 1.1: Generation IV reactors

| System | Neutron Spectrum | Coolant | Temperature | Fuel Cycle |
|---|---|---|---|---|
| SFR | Fast | Sodium | 550 | Closed |
| GFR | Fast | Helium | 850 | Closed |
| LFR | Fast | Lead | 480-800 | Closed |
| VHTR | Thermal | Helium | 900-1000 | Open |
| SCWR | Thermal/fast | Water | 510-625 | Open/closed |
| MSR | Thermal/fast | Fluoride salts | 700-800 | Closed |

about them, but also because the materials discussed in this dissertation are candidate cladding/structural materials in these two types of reactors.

### *1.1.2 Sodium-cooled Fast Reactor*

Figure 1.1 shows a typical design of a SFR [1]. Fast neutron has the capability to fission all transuranic elements and covert Uranium (U) 238 to Plutonium (Pu) 239. So that in a fast reactor, the energetic potential of fuel is maximized and the energy density generated is very high. Liquid sodium has been chosen as the heat transfer fluid over mercury and lead because of its low neutron capture cross section, low abundance of fission produces, nice compatibility with both structural materials and fuel, etc. One reason that SFR has been paid much attention to is its capability to transmute the transuranic elements from nuclear waste.

In a SFR, structural and cladding materials will not only undergo a relatively high temperature but also very high level of neutron irradiation, especially the cladding materials, which are in the core part of the reactor. As shown in Fig. 1.2, the metal fuel used in a fast reactor has a cladding tube surrounding the fuel. The temperature, radiation and pressure at the cladding tube are all extreme, which introduce

great challenges to the material, as will be discussed later in this section.

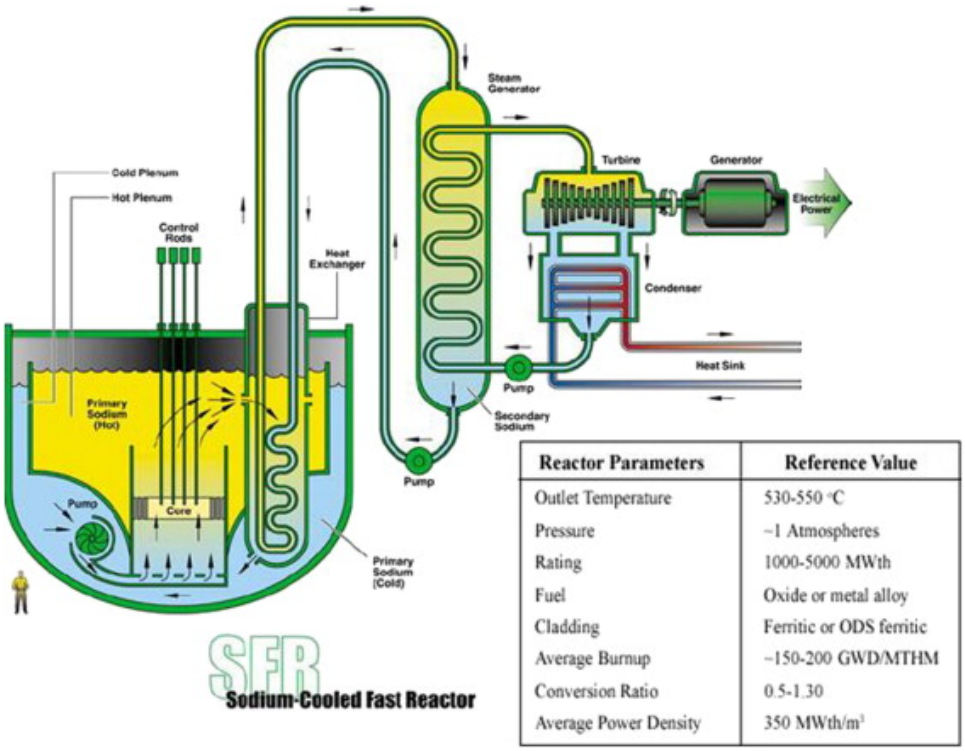


| Reactor Parameters | Reference Value |
|---|---|
| Outlet Temperature | 530-550 °C |
| Pressure | ~1 Atmospheres |
| Rating | 1000-5000 MWth |
| Fuel | Oxide or metal alloy |
| Cladding | Ferritic or ODS ferritic |
| Average Burnup | ~150-200 GWD/MTHM |
| Conversion Ratio | 0.5-1.30 |
| Average Power Density | 350 MWth/m$^3$ |

Figure 1.1: A schematic diagram of Sodium-cooled Fast Reactor [1]

### *1.1.3 Very High Temperature Reactor*

A schematic of VHTR is shown in Fig. 1.3. As suggested by the term of "very high temperature" in its name, the gas-outlet temperatures can be higher than 900 °C, which is a result of the unique fuel used in VHTR is quite: coated fuel particles embedded in a graphite matrix, located in a graphite core cooled by helium. The fuel and core materials are refractory so that high gas temperatures can be reached, which enable a high electricity and/or heat generation efficiency.

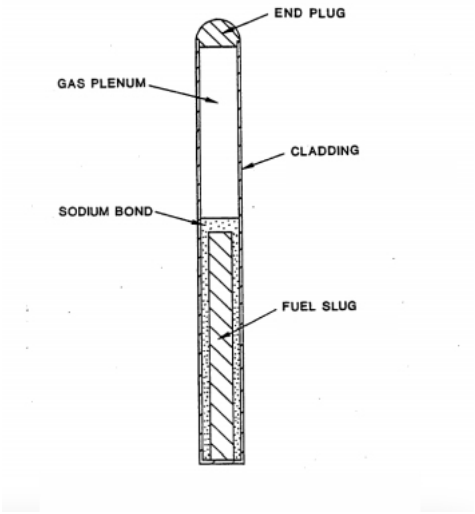


Figure 1.2: A schematic diagram of the metal fuel [2]

Structural materials used in VHTR, such as in helium turbines or heat exchanger, must be able to maintain the high strengths, especially creep resistance, at elevated temperatures. Depend on the part where the material is used, the environmental temperature that the material need to tolerate ranges from 350 to 1650 °C. The reactor pressure vessel and internals have a typical temperature of 350-550 °C, where ferritic-martensitic (F/M) steels are chosen as candidate material; For materials of the primary circuit, turbine and heat exchangers, desirable properties should be maintained in a temperature range of 650-950 °C. iron (Fe) and nickel (Ni) based ODS alloys are being developed to fill in such requirement. For core structure, where the temperature will be 950-1650 °C, graphite grades and composite ceramics are undergoing development, tests and characterizations [25].The typical maintenance interval in current gas turbine is in the order of 20 months; while VHTR is targeting operation time of more than three times longer than that without major attentions

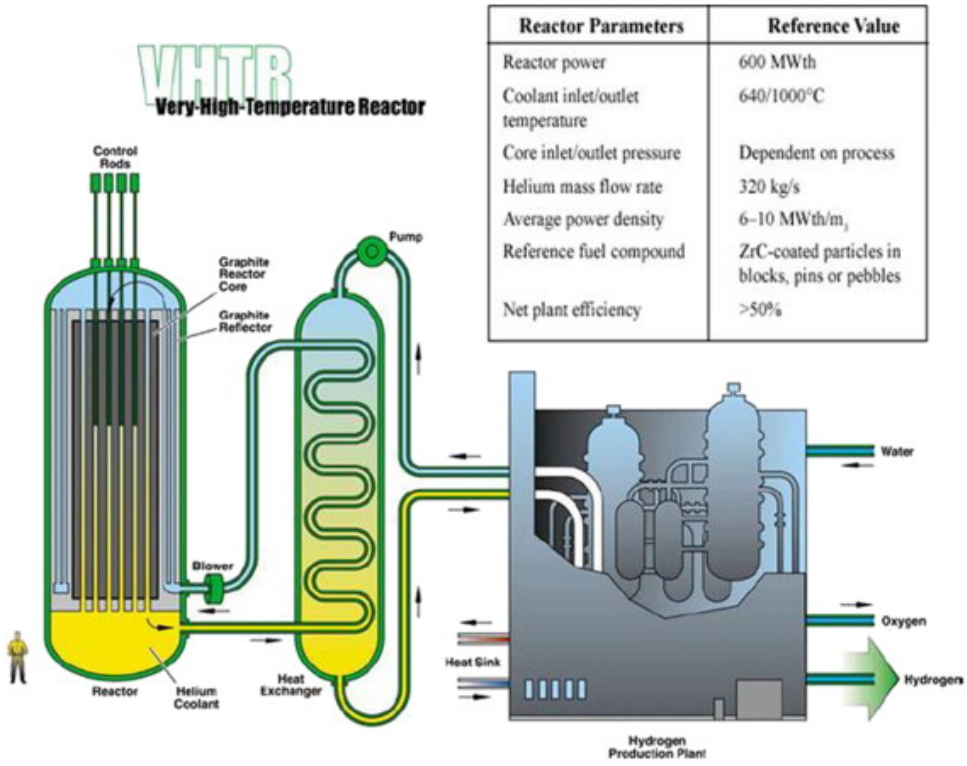


| Reactor Parameters | Reference Value |
|---|---|
| Reactor power | 600 MWth |
| Coolant inlet/outlet temperature | 640/1000°C |
| Core inlet/outlet pressure | Dependent on process |
| Helium mass flow rate | 320 kg/s |
| Average power density | 6–10 MWth/$m_3$ |
| Reference fuel compound | ZrC-coated particles in blocks, pins or pebbles |
| Net plant efficiency | >50% |

Figure 1.3: A schematic diagram of Very High Temperature Reactor [1]

to the turbine needed. Again, the challenge to material is presented.

## 1.2 Material Challenges

### *1.2.1 Extreme Environments in Reactors*

As discussed in last section, the desires for higher efficiency and longer operation time for Generation IV reactors bring in new challenges to nuclear materials. Overall, the high operating temperatures and large amount of irradiation are two major reasons for the challenges. Figure 1.4 summaries the temperature and radiation damage received by structural material in Generation IV reactors, as compared to current (Generation II) and fusion reactors [3]. Note that compared to structural materials, cladding materials are closer to the core of nuclear reactor, where the neutron flux is way higher. As a result, cladding materials receive a much higher level of radiation damage.

Materials in such environment are at great challenge. For example, neutron radiation can change the chemistry of coolant and make them more chemical active. Thus the cladding materials will be in a very corrosive environment. As a result, the interaction between the material and coolant lead to cracking in cladding material. If the cracking continues, eventually the fuel will be exposed to the coolant and contaminate it.

### *1.2.2 Desirable Properties for Nuclear Materials*

As discussed above, materials will be in a very harsh environment in reactor. The hope of utilizing materials for a more elongated time at more elevated temperatures demands reliable materials with desirable properties. While there is no prefect mate-

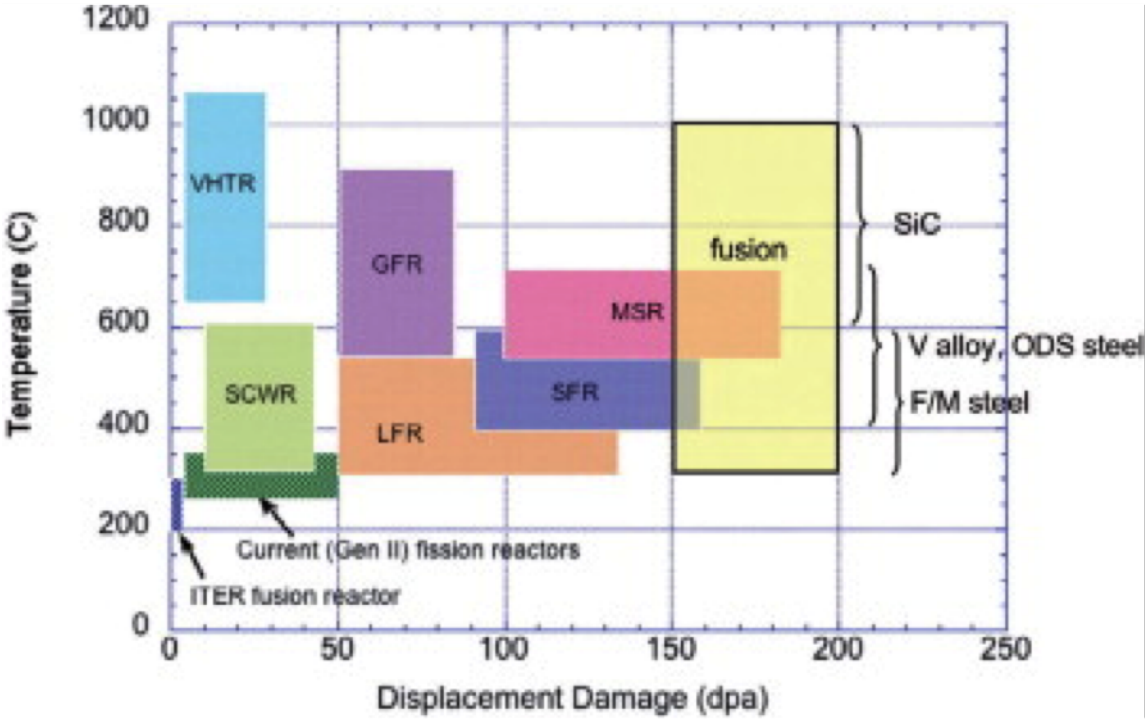


Figure 1.4: Operating temperatures and displacement damage dose regimes for structural materials in nuclear reactors [3]

rial for everything, in this section, a few properties of importance will be nominated and discussed.

Thermal stability is very important given the high environmental temperature. Such stability include but not limited to a low thermal expansion coefficient and microstructural stability. Thermal expansion may lead to increase of pressure, unwanted touch and enhanced chemical interactions with the materials. The microstructural stability is related to the sustaining of many critical properties of the material. For example, grain morphology is very critical to radiation tolerance, material strength and creep resistance [19, 20, 26]. However, high temperature can lead to grain growth, for example in some of the severe-plastically-deformed materials.

Having a high thermal conductivity is also critical for fuel materials and some of the cladding materials. In SFR, one of the reasons of choosing F/M steel as cladding material is its higher thermal conductivity. Being able to conduct heat generated by fission reaction is very important for high efficiency and reactor safety.

The strength of material is desirable almost everywhere. Particularly for cladding and structural materials in nuclear reactor, creep resistance is very critical for the relatively long service time at high temperature. In general, there are two mechanisms that can lead to creep in nuclear material, i.e., irradiation induced creep and thermal creep. Compared to austenitic steel, F/M steel has better resistance agains irradiation creep; while its thermal creep resistance is not as strong as that of austenitic steel, because of its higher atomic diffusivity [27].

Radiation tolerance is of course necessary for a material used in neutron radiation

environment. Despite that most, if not all, materials will eventually degraded and destroyed under neutron irradiation, some materials appears to be more radiation tolerant than others. For example fine grain and ultra fine grain materials having high density of grain boundaries as defect sinks, ODS and multi-layer materials providing extra interfaces for defect annihilation, metallic glass and other amorphous materials which have no crystal structure for neutron irradiation to destroy, etc.

Corrosion resistance is also critical for some materials used in a corrosive environment. For F/M steels used as cladding material in SFR, the corrosion resistance can be improved by increasing the content of chromium (Cr).

### *1.2.3 Material Degradation from Radiation Damage*

In a fission reactor, materials degrade because of direct neutron scattering and the energetic fission fragments. Damage cascades were created in material, displacing atoms from their original position, leading to point defects, amorphization, etc. The amount of radiation damage can be evaluated in term of displacements per atom (dpa). Defects created by neutron damage cascades can migrate and cluster to form dislocations and dislocation loops. Enhanced vacancy density in material due to irradiation can increase the diffusivity, which may speed up precipitation, radiation-induced segregation, phase transformation, etc. In this section, some key issues of material degradation due to irradiation will be discussed.

Void swelling introduced by neutron irradiation has drawn attentions of researchers long time ago. Interstitials and vacancies created by neutron irradiation migrate and cluster to form dislocations and voids. And void swelling is a main reason to cause

volume increase in materials. As shown in Fig. 1.5, the swelling in austenitic steel can be very significant. The swelling rate of austenitic steel can be as high as 1% per dpa [4, 5]. As will be discussed later in this section, swelling resistance is one of the considerations that makes the determination of using F/M steel instead of austenitic steel in future fast reactors as cladding material. In general, F/M steels have a swelling rate lower than 0.2% per dpa, as shown in Fig. 1.6 [5, 28].

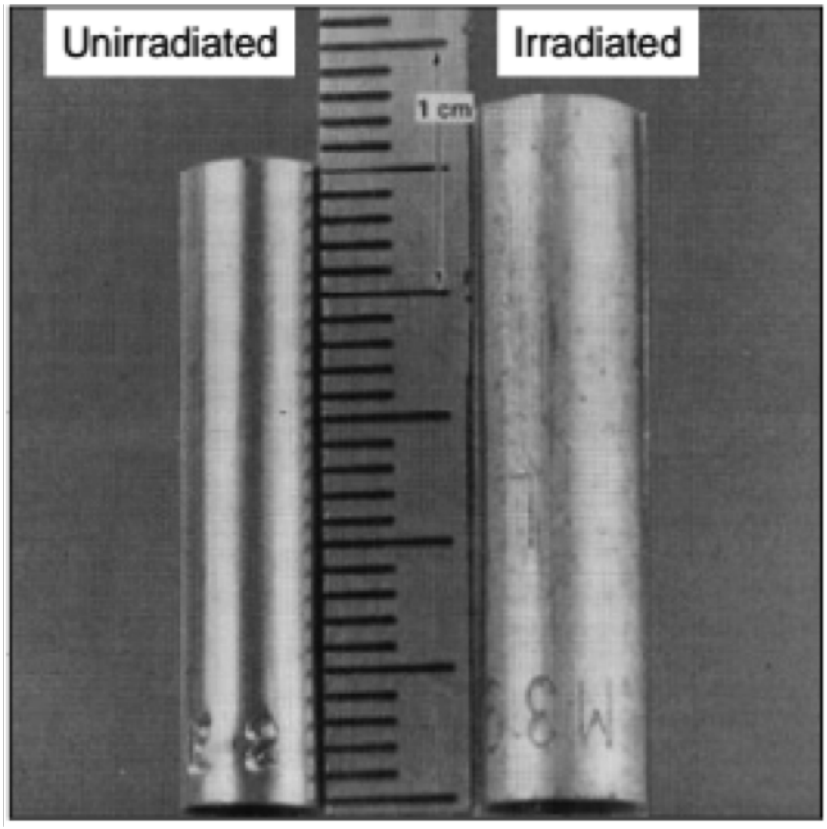


Figure 1.5: 316 stainless steel rod volume change after fast neutron irradiation at 533 °C [4]

The changes in mechanical property due to irradiation is also a problem. As

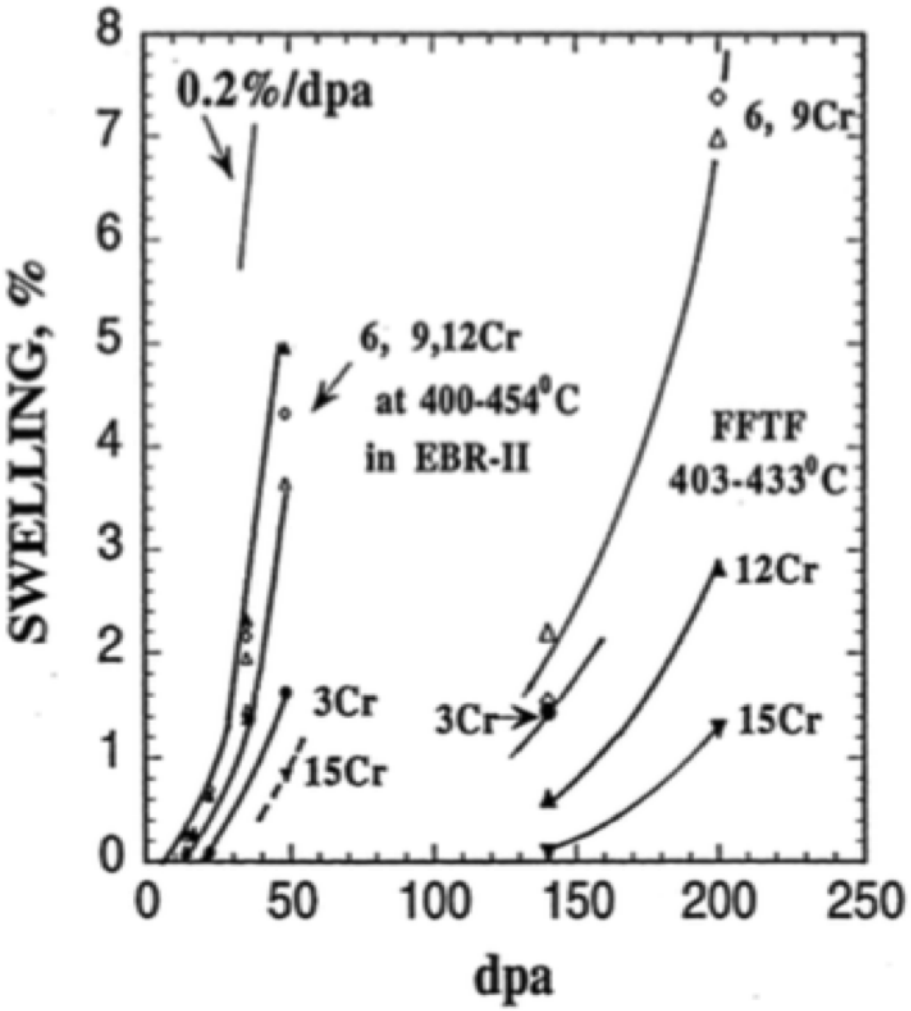


Figure 1.6: Swelling as a function of neutron radiation damage for different F/M steels [5]

shown in Fig 1.7, exposure to neutron irradiation leads to radiation hardening to material. Reasons of radiation hardening includes point defect clustering, small cluster and precipitate formation and impenetrable cluster formation. Although radiation hardening increases the strength of material, it reduces the tensile elongation and the fracture toughness of the material.

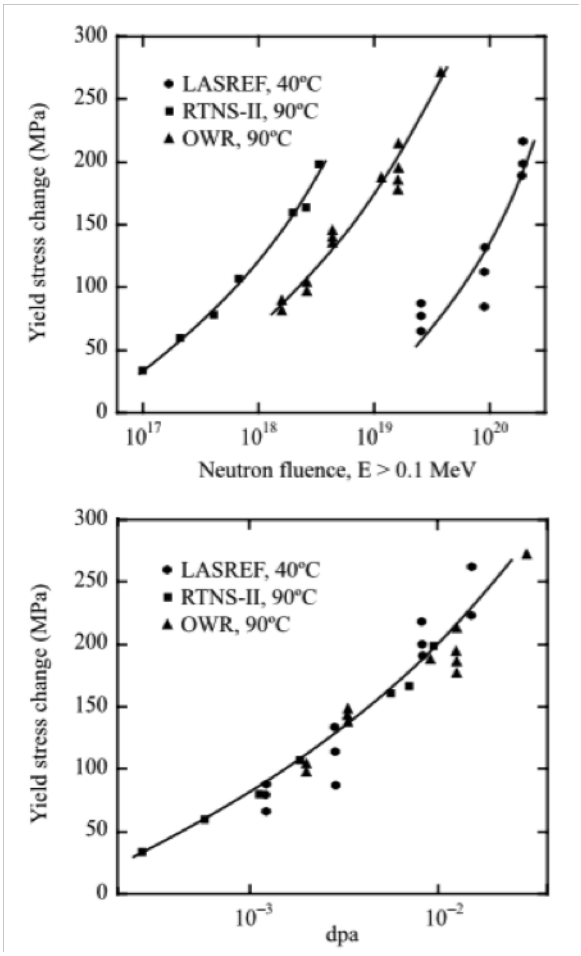


Figure 1.7: Yield stress change as function of neutron damage [6]

## 1.3 Oxide Dispersion Strengthened Ferritic-Martensitic Steels

As discussed above, the extreme conditions in reactors require different materials for different uses. Among them, F/M steel and/or ODS F/M alloy have been considered as candidate for cladding of SFR and structure of VHTR. In this section, the pros and cons of F/M steel will be discussed, followed by the need of ODS technique. Finally, issues to be addressed in this dissertation will be provided by the end of this section.

### *1.3.1 Ferritic-Martensitic Steels*

As told by its name, F/M steel contains ferrite and/or (tempered) martensite phases. The phase diagram of Fe and carbon (C) in Fig. 1.8 shows the phase of Fe-C system due to C content and temperature. Austenite ($\gamma$-Fe) phase has a face-centered-cubic (FCC) structure while ferrite ($\alpha$-Fe) phase has a body-centered-cubic (BCC), with lattice constants near 0.3591 and 0.2863 nm, respectively.

As shown in Fig. 1.8, a $\gamma$-$\alpha$ phase transformation occurs when temperature drops below certain temperature. C has a much higher solubility in $\gamma$-Fe than in $\alpha$-Fe. So that when $\gamma$-$\alpha$ phase transformation occurs, C need to diffuse out of the transferred $\alpha$-Fe. At certain C close to the eutectoid composition and under equilibrium condition, where the diffusivity of both Fe and C atoms are high enough and the time for a large scale movement of Fe and C is sufficient, a equilibrium microstructure of pearlite will form. As shown in Fig 1.9, Pearlite is a lamellar structure composed of alternating layers of Fe and $Fe_3C$ [7].

However, if the cooling rate is too fast during $\gamma$-$\alpha$ phase transformation, there

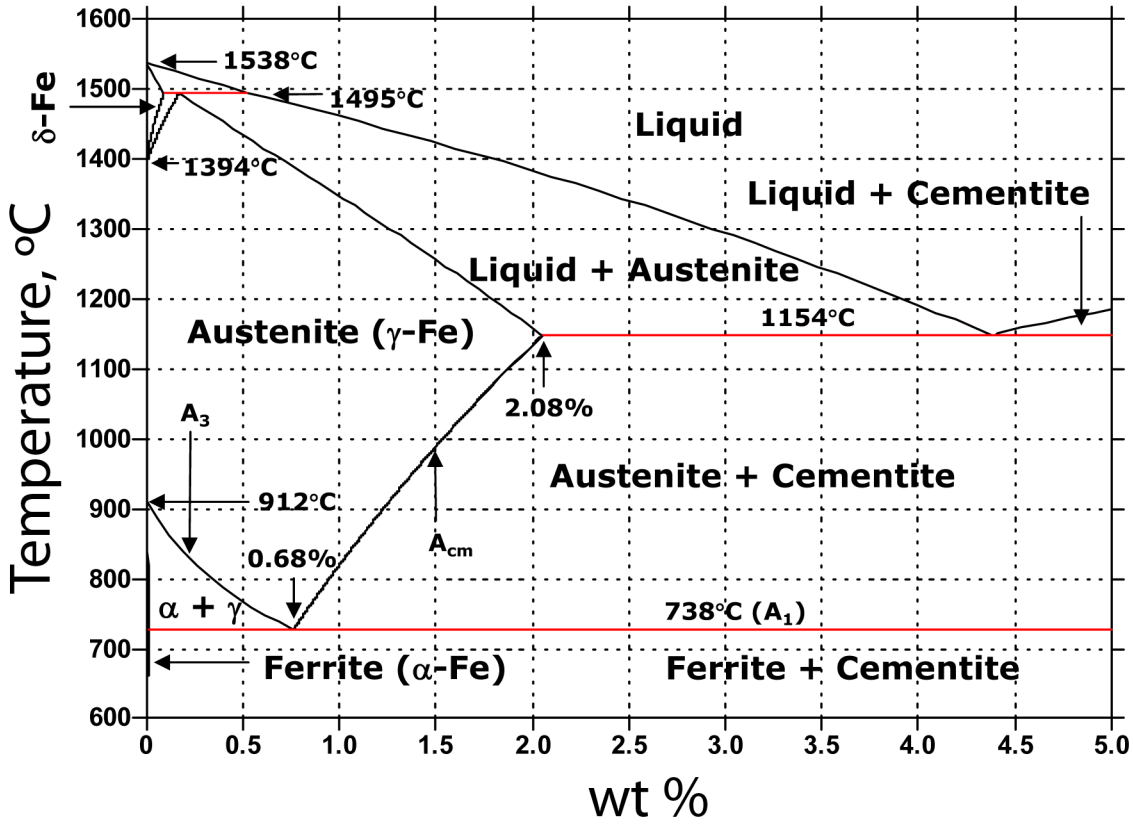


Figure 1.8: Metastable Fe-C phase diagram

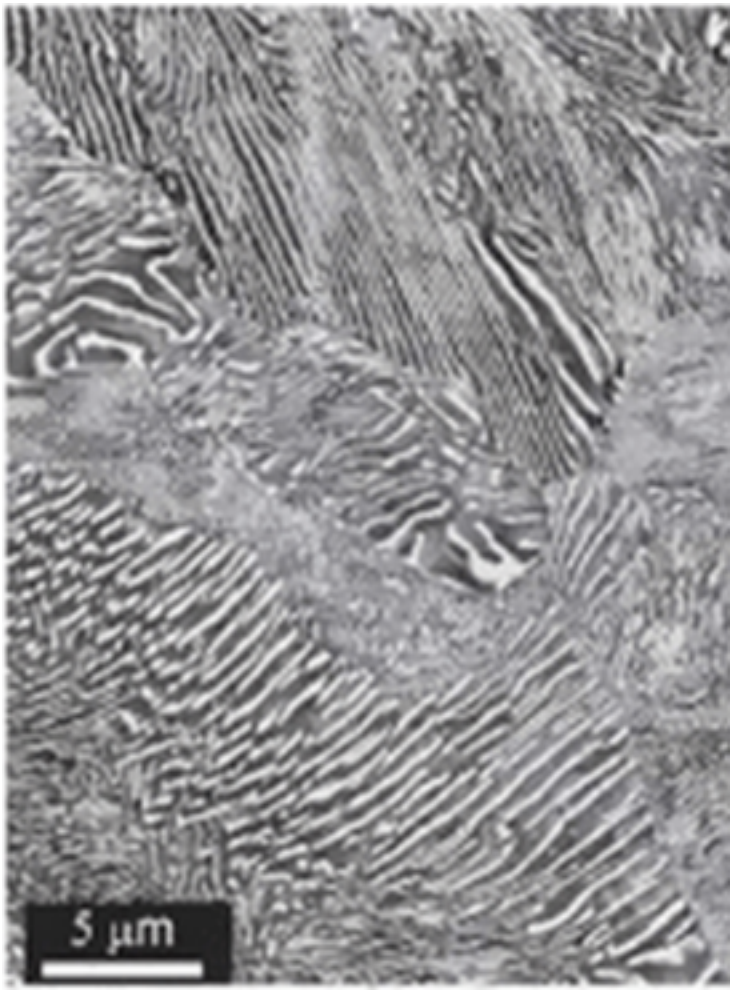


Figure 1.9: Microstructure of typical pearlite [7]

is not sufficient time for pearlite to form. Instead, a bainite or martensite structure may form. Typical structures of bainite and martensite are shown in Fig. 1.10 [8]. When the cooling rate is more rapid than required to form equilibrium pearlite, the bainite phase will form. In bainite phase there is no lamellar structure in a grain. Instead, lath structure will form with $Fe_3C$ particles and/or stringers surrounded, as shown in Fig. 1.10a.

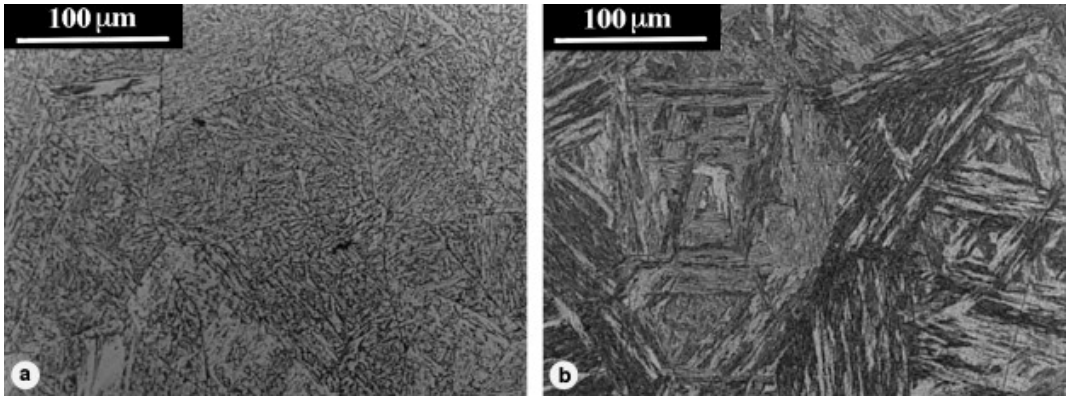


Figure 1.10: Microstructure of typical (a) bainite and (b) martensite [8]

If the cooling rate is even more rapid and no atomic diffusion could happen during the phase transformation, martensite will form instead of bainite. As a result of a sudden shear process, the crystal structure transfers from FCC to body-centered tetragonal (BCT). The transition requires less thermal activation energy. The lenticular crystal grains will be lath- or plate-shaped under microscope observation, as shown in Fig. 1.10b and Fig. 1.11 [9].

The original austenitic grain will be subdivided into packets, with each packet containing blocks. In each block, laths having a Kurdjumov-Sachs crystallographic re-

lation to the parent austenite, which minimizes the energy by aligning the phases to share a close-packed plane.

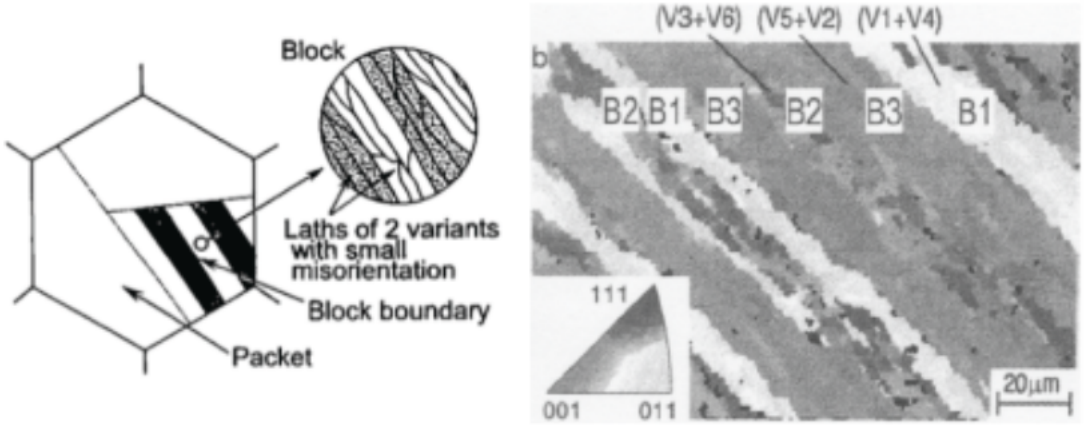


Figure 1.11: Microstructure of lath martensite [9]

Tempering is a heat treatment in which the metal will be heated to some temperature below the critical point for a certain amount of time before being air-cooled. The propose of tempering is to increase the toughness and ductility of the metal by reducing its excess hardness. When martensite is tempered, the C trapped in the BCT lattice will be released to from $Fe_3C$, and the crystal structure of BCT will change to BCC. A fully tempered martensite has the lenticular grain shapes with $Fe_3C$ decorations shown as small black particles, as shown in Fig. 1.12 [10].

The microstructure formation of Fe-C system dependent on cooling rate is summarized by the continuous cooling transformation (CCT) diagram in Fig. 1.13. When cooled below the critical temperature, Fe-C system with a proper C content will be

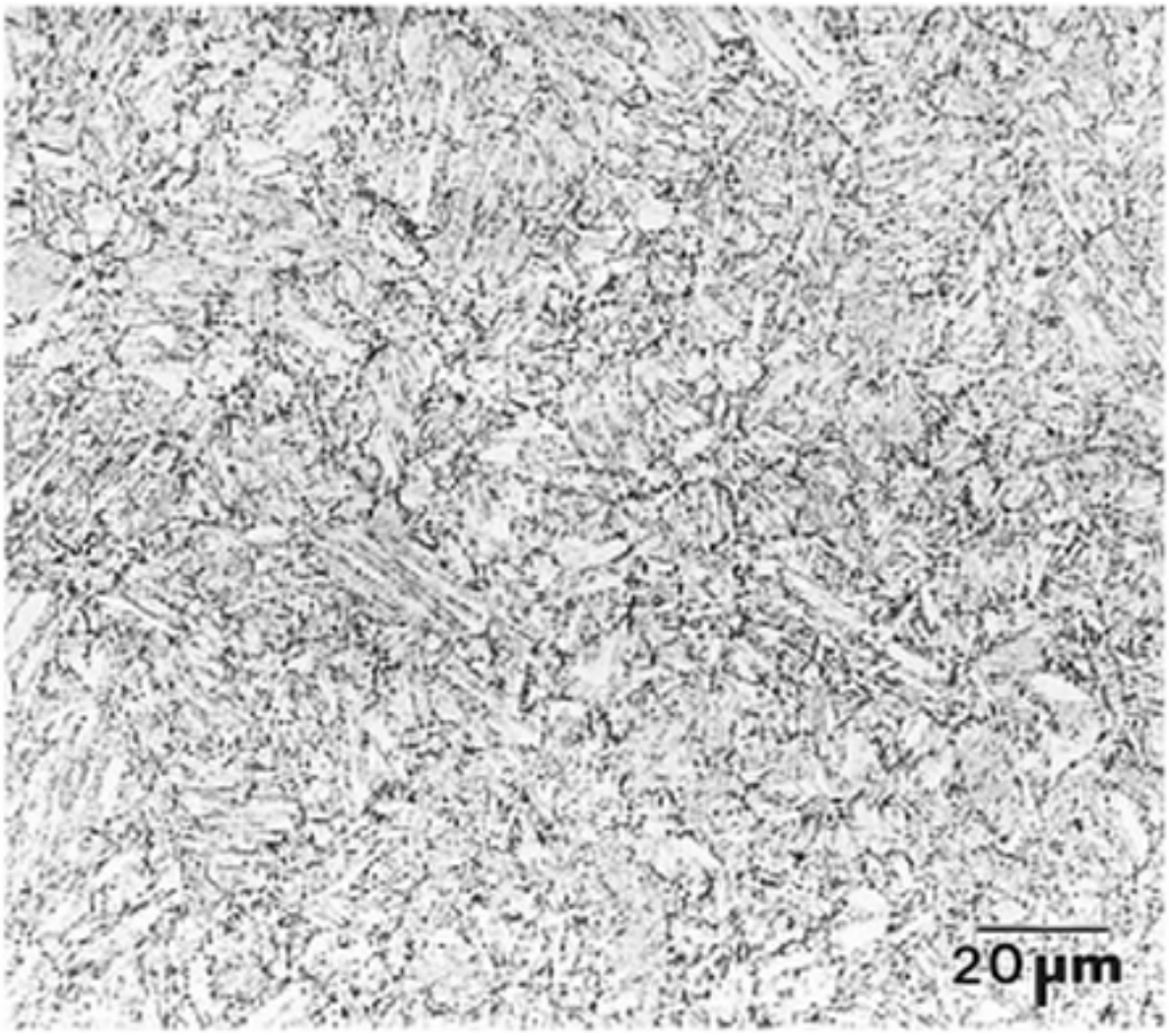


Figure 1.12: Microstructure of a fully tempered martensite [10]

dominated by a BCC or BCT crystal structure. The steel having such microstructures is known as F/M steel.

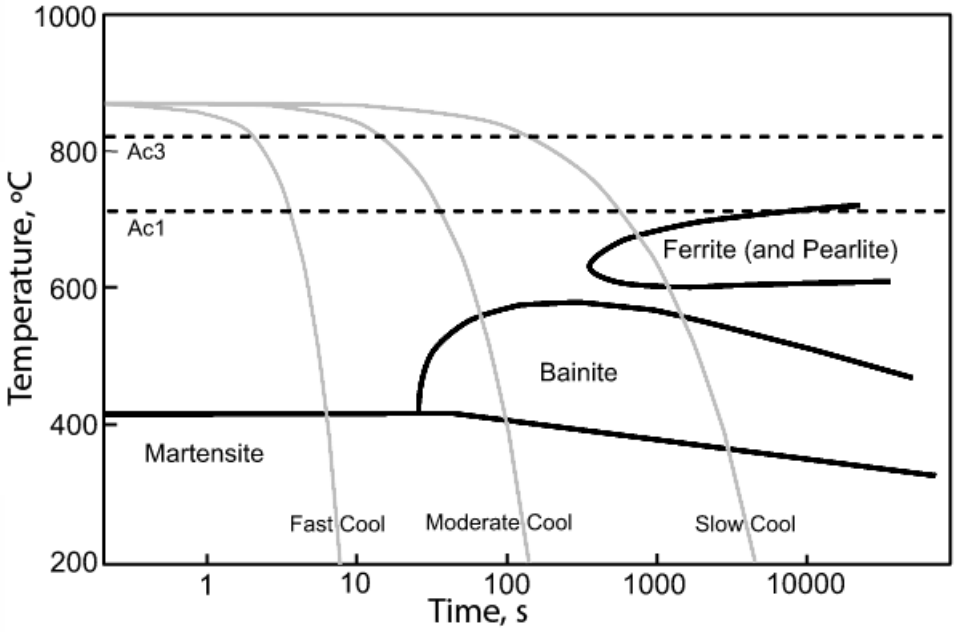


Figure 1.13: A continuous cooling transformation diagram of steel

### *1.3.2 Radiation Response of Ferritic-Martensitic Steels*

Before the use of F/M steels, austenitic steels were the mainly used material in fast reactors as cladding and structure material. The advantages of lower thermal expansion, higher thermal conductivity and lower swelling rate of F/M steel makes it the replacement of austenitic steels for future use in SFR. However, that does not mean F/M steel does not have any problems. Table 1.2 lists some of the pros and cons of F/M steel compared to austenitic steel.

Table 1.2: Comparison between F/M steel and austenitic steel

| | F/M steel | Austenitic steel |
|---|---|---|
| Void swelling | 0.2%/dpa, longer incubation time | 1%/dpa |
| Low temperature irradiation creep | $0.5\times10^{-6}/MPa/dpa$ | $1\times10^{-6}/MPa/dpa$ |
| Thermal creep | Higher creep rate | Lower creep rate |
| High temperature helium (He) embrittle | 1000 appm He before grain boundary embrittlement | 100 appm He before grain boundary embrittlement |

As discussed earlier in this section, in general, F/M steel has better radiation tolerance compared to austenitic steel. The swelling resistance is higher with a lower swelling rate and an usually long incubation period before swelling starts. The irradiation creep and He embrittle of F/M steel is also not as severe as it of austenitic steel. However, the thermal creep resistance of F/M steel is not as good. Later the technology of using oxide dispersion to enhance the strength of F/M steel, which lead to higher creep resistance, will be discussed.

Upon receiving irradiation, F/M steel can undergo several microstructures changes. Defects induced by irradiation in material includes interstitials and vacancies, point defect clusters, interstitial and vacancy loops, stacking fault tetrahedra and cavities. Although it has been shown that F/M steels have a better swelling resistance than austenite steels [5], void swelling in F/M steel is not negligible. The swelling of the F/M HT9 after receiving 208 dpa fast-neutron irradiation is shown in Fig. 1.14 [5]. The driving force for void to form is the supersaturation of vacancies in the material. Interstitial and vacancies created during irradiation react to form interstitial and vacancy clusters. These clusters can further grow by absorbing same type of defects or shrink by absorbing opposite type of defects. If irradiation continues to create

more vacancies around a vacancy cluster, the cluster will further grow for voids to nucleate. The nucleation and growth of void is a temperature dependent progress, as illustrated by Fig. 1.15 [6], where void swelling peaks at the intermediate temperature and is suppressed at either lower or higher temperatures. The suppression mechanisms at lower temperatures are the reduction of defect mobility and the stability of vacancy loops, with both of them leading to a reduction of vacancy density available for void formation; and at higher temperatures, the vacancy flux due to irradiation is counterbalanced by the enhanced emission of vacancies from voids [6].

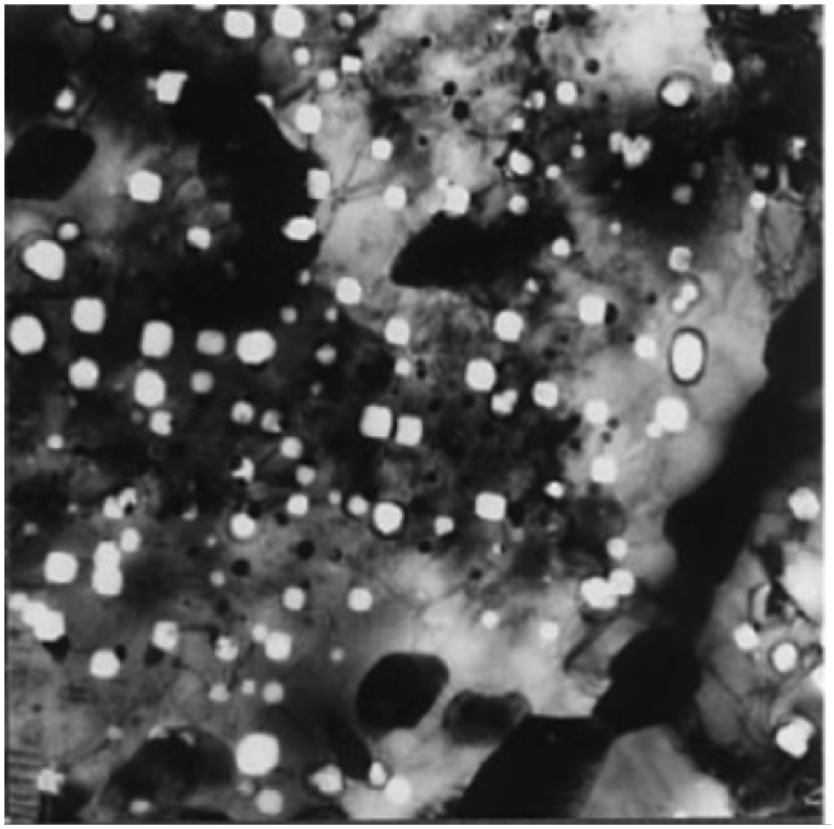

Figure 1.14: HT9 swelling at 208 dpa in Fast Flux Test Facility reactor [5]

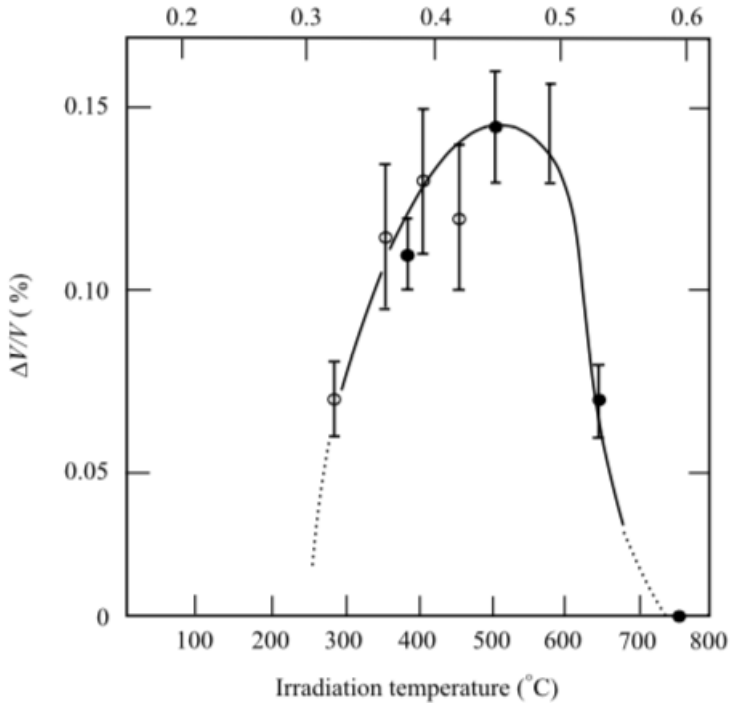


Figure 1.15: Temperature dependent void swelling [6]

Similar to vacancies, interstitials can react with each other to form clusters. According to molecular dynamics (MD) simulations, in BCC Fe, the most stable small cluster that has less than 10 self interstitial atoms (SIAs) is a set of 111 crowdions, followed by the 110 crowdions. For clusters having more than 7 SIAs, only these two types of cluster are stable [6]. In addition, it is well known that interstitial clusters have higher stability and mobility than vacancy clusters. As clusters grow in size, they form specific configurations in crystal lattice to minimize the energy, for example, a loop. A micrograph of dislocation loop observed in F/M steel is shown in Fig. 1.16 [11].

In general, dislocations has a bias for interstitials. This is one reason that the environment in matrix tend to be vacancy rich, which leads to void formation. In

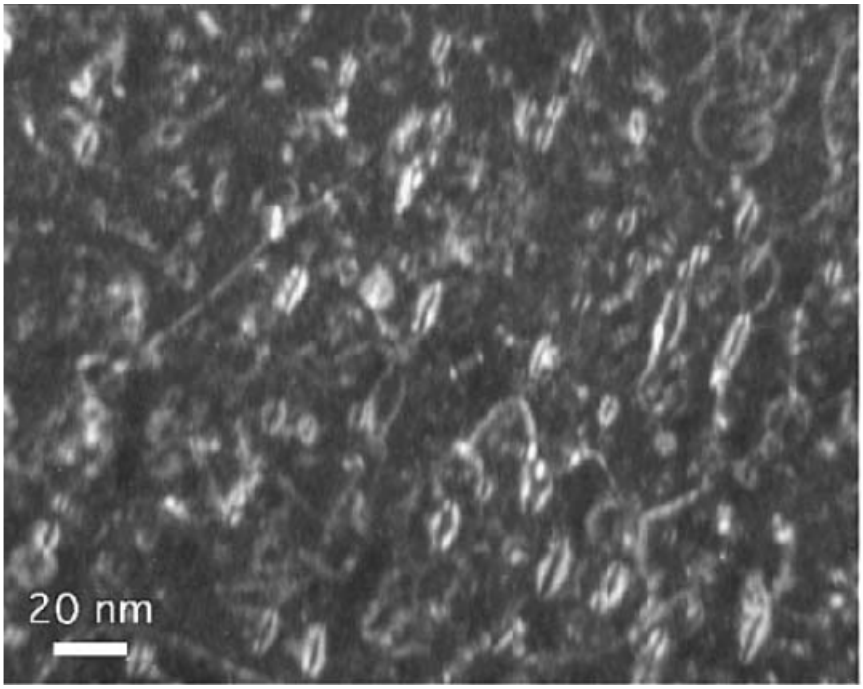


Figure 1.16: Dislocation loops observed in F/M steel [11]

1990, the concept of production bias was proposed [29]. It includes dislocation bias as well as the higher stability of interstitial clusters compared to vacancy clusters, especially at more elevated temperatures, as the reasons for vacancy rich environment. More importantly, in a damage cascade, interstitial and vacancy segregated differently: after initial thermal annealing period, interstitials can recombine with vacancies, get mobilized through interaction and clustering, given a high interstitial concentration, or go through long-range migration and escape from the cascade region. On the other hand, vacancy clustering occurs mainly during the cooling down period after damage cascade. At this time, the vacancy rich environment has been formed for vacancies to form loops, stacking fault tetrahedra and voids.

### *1.3.3 Oxide Dispersion Strengthening*

The concept of using inert additions to enhance material behavior was first exploited in 1910. Elevated temperature mechanical properties, especially creep resistance, were found to greatly enhanced as a result of the presence of inert additions. In 1952, the first ODS material was designed as a structural load bearing system [30], which showed increased strength with increasing volume fraction of the oxide.

Recently, the concept of ODS has also been introduced to radiation-tolerant materials. One of the examples is ODS F/M alloys. F/M steels are considered as one of the candidate materials for generation IV fast reactors for their relatively high thermal conductivities and lower expansion coefficients compared to those of austenitic stainless steels [31]. However, the thermal creep resistance of F/M stainless steel is usually not as good as it of austenitic steels [27]. The benefit of dispersions in enhancing creep resistance was then made use of. Commercialized ODS FM steels such as MA 956 and MA 957 showed considerable enhancement in material properties [32, 33]. Meanwhile researchers around the world are developing new ODS FM alloys by optimizing fabrication parameters. Recently, more advanced ODS alloys such as 14YWT developed in the United States, Fe-9/14/18Cr1WTiY2O3 alloy developed in France, 9/12/15Cr ODS developed in Japan, etc. all showed improved mechanical properties and/or irradiation tolerance, making them very promising for cladding and structural materials for Generation IV fast reactors [20, 19, 34, 35, 36, 37, 38].

The strength of an ODS F/M steel is enhanced through complicated mechanisms, from mesoscopic optimization of grain structures to nano-level enhancement primary from the presence of nano particles [19]. Nano particles play significant roles in

stabilizing grain structures, immobilizing dislocations, trapping irradiation-induced defects, etc. The grain structure stabilization can be achieved through the so-called Zener pinning effect [39], which is stronger with finer particles. The presence of nano particles has been shown to prevent phase transformation at high temperatures by pinning on the phase boundaries [20]. On the other hand, nano particles are also known for their capability to pin dislocations, as shown in Fig 1.17 [12]. The pinning of dislocations is through the relaxation of strain energy when dislocation is close to a nano particle. The existence and status of such a low-energy configuration of dislocation 'pinned' by a nano particle depends on the size, coherency and mechanical properties of the particle and the matrix [12, 40].

### *1.3.4 Issues Addressed in this Work*

As a candidate materials for future reactor use, the high temperature strength and radiation tolerance of ODS materials should be well understood. In this study, the microstructure stability of ODS alloys would be tested by means of heavy-ion irradiations. Microstructure investigations would be carried out on ODS alloys receiving different levels of radiation damage at various temperatures. Focuses would be on grain structure stability, void swelling resistance and nano particle stabilities.

Void swelling resistance of a cladding and/or structural material is very important. Because void swelling leads to volume changes of a material, which would result in stress building up that will crack the material. Cracking in a reactor usually means reactor accidents and leakage of radioactive pollutions.

Grain stability and radiation tolerance of nano dispersoids are critical to main-

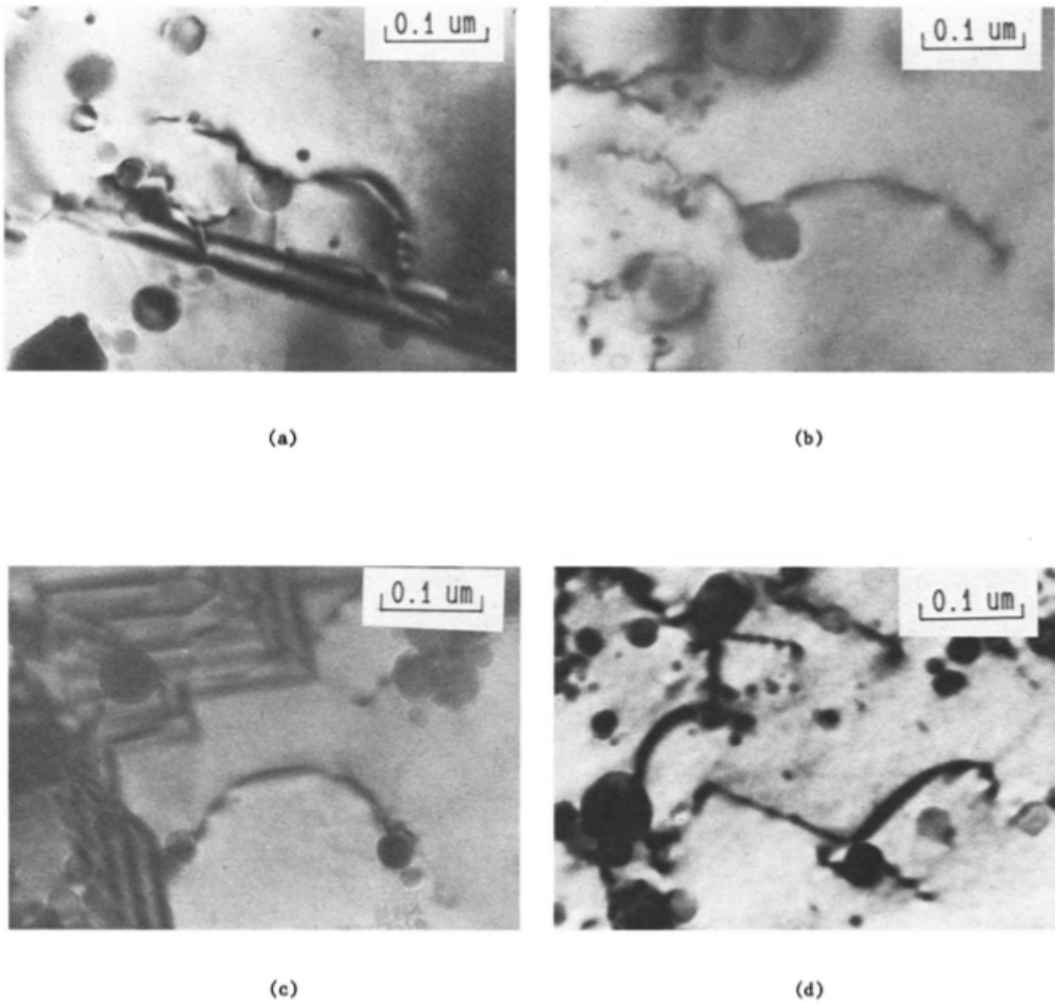


Figure 1.17: Micrographs showing dislocations pinned by dispersoid in an ODS material [12]

tain the high creep strength of the material [41, 19]. Creep is a slow deformation of the material that will eventually lead to rupture. Subgrain boundaries are obstacles against gliding of mobile dislocations, which can enhance the creep strength of the material. On the other hand nano dispersoids can pin the subgrain boundaries to stabilize them especially in the long-term creep region and pin immobilize dislocations. Thus to understand the changes to grain structures and nano dispersoids during irradiation will be useful to predict the material strength degradation due to irradiations.

# 2. EXPERIMENT DESIGN AND CARRY-OUT

In this section, we introduce the whole scope of this research in terms of experiment procedure. Some key experiment methods like ion irradiation and microstructure analysis would be addressed. Some important experiment instruments like the tandem accelerator, the focused ion beam (FIB), scanning electron microscope (SEM) and transmission electron microscope (TEM) will also be introduced with sufficient details.

## 2.1 The Scope of This Study

### *2.1.1 The Procedures*

Figure 2.1 illustrates the scope of this study. The material design, fabrication and microstructure investigation would be brought about in next section; and radiation response of the material after high damage levels and at different irradiation temperatures would be present in the two sections following next section. The material of interest in this study is a 12Cr dual-phase ODS, details of which can be found in next section. This material was designed and fabricated by our collaborator Dr. S. Ukai from the Department of Material Science and Engineering, Hokkaido University, Japan. The as-fabricated material bar was sent to my advisor, Dr. Lin Shao's group at the Department of Nuclear Engineering, Texas A&M University (TAMU), for ion irradiation and microstructure analysis. Ion irradiations were carried out at the Ion Beam and Materials Characterization Facility, TAMU using a 1.7 MV tandem accelerator; TEM sample preparation was done at the Material Characterization Facility, TAMU, using a TESCAN Lyra3 FIB-SEM; and TEM microstructure analysis was done at the Microscopy and Imaging Center, TAMU, using FEI F20 ST, FEI F20 T

and Joel 2010.

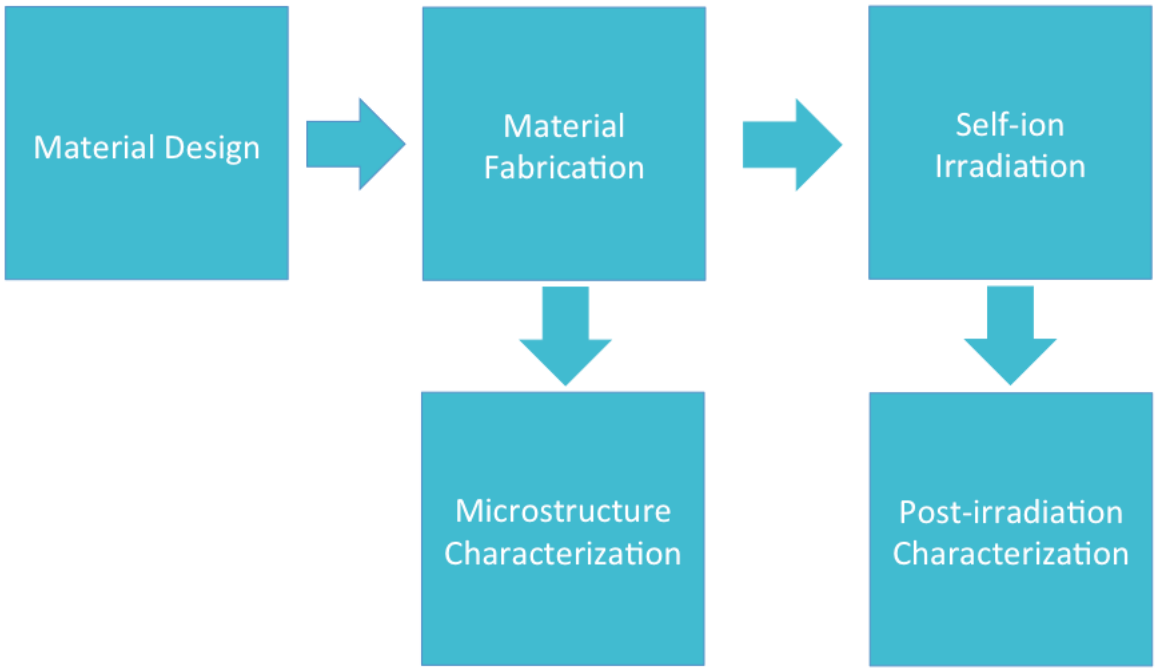


Figure 2.1: The experiment procedures of this study

### *2.1.2 The Goal*

By means experiments, we try to achieve a two-folded goal through this study. First is to test the reliability of the novel 12Cr dual-phase ODS alloy as a cladding/structure material in future fission and/or fusion reactors. Two major challenges for future nuclear materials are the high radiation damage and high temperature. A high dpa damage level at elevated temperatures can be appropriately simulated using heavy-ion irradiations [6], with the benefit of much higher dose rate. Thus, we carried out a study of extreme high dpa irradiations to our tested materials, characterized

the microstructure and nano-structure changes related to the void swelling and creep strength of the material. On the other hand, although the radiation response of oxide particle in ODS alloys have been frequently studies [42, 43, 38, 44, 34, 45, 36, 46, 47], their results are not very conclusive, as shown in Table 2.1. So the second motivation of this study is to provide more experimental data on this topic by carrying out some systematic studies.

## 2.2 Sample Preparation

Before TEM specimen was lifted out from the sample and before ion-irradiations were conducted, the samples were cut into pieces with dimensions of ∼5 mm × 5 mm × 0.7 mm. On each of these as-cut samples, scratches and stress on the surface of sample were removed by means of mechanical polishing and electropolishing. The samples were relatively thin with a thickness of ∼0.7 mm in order to reduce the temperature gradient between the irradiated front surface and the heated back surface for the sake of temperature control during irradiation.

### *2.2.1 Mechanical Polishing*

Mechanical polishing was done using a ACE Nano 2000T Grinder-polisher. Silicon carbide papers were used with the grit progressing down from 400 to 1200. Finally, 0.05 $\mu$m aluminum power was used to polish the surface, removing most of the scratches. The sample was than cleaned using an ultrasonic cleaner. Having a flat surface is very critical for ion-beam irradiation studies. Given that the 3.5 MeV $Fe^{2+}$ has a penetration depth of ∼1 $\mu$m in Fe, the irradiated region of interests will be within this distance from the irradiating surface. Having a smooth sample surface will make the microstructure analysis easier when relating the depth to the

Table 2.1: Previous studies on ODS alloy radiation responses

| Material | Irradiation | Temp. (°C) | Irradiation Response | Reference |
|---|---|---|---|---|
| 9-12Cr ODS | ⩽15 dpa JOYO neutron | 397-534 | Stable dispersoids | [42] |
| F94, F95, M93 | ⩽15 dpa JOYO neutron | 330-500 | Stable dispersoids | [48] |
| K1, K4 | 150 dpa $Fe^{3+}$ | 300-700 | Stable dispersoids | [49] |
| MA957 | 100 dpa JOYO neutron | 502-709 | Coarsened dispersoids, decreased density | [43] |
| Fe18Cr-$Y_2O_3$ | 150 dpa $Fe^{+}$ | 500 | Coarsened dispersoids, decreased density | [50] |
| 14YWT | 16 or 160 dpa Pt | -100 and 750 | Destructed dispersoids at -100 °C retained with coarsened size at 750 °C | [34] |
| DY, EM10 | ⩽100 dpa $Xe^{+}$, $Kr^{2+}$, $Kr^{3+}$ | 300-600 | Amorphized dispersoid | [45] |
| 9Cr ODS | ⩽200 dpa Ni | 350-700 | Shrunk dispersoids, increased density | [51] |
| DY, EM10 | ⩽81 dpa Phnix neutron, 1 and 1.2 MeV electron, 1MeV He, 300 keV Ar | 300-580 | Shrunk dispersoids, increased density under neutron irradiation; dissolved dispersoids under electron irradiation; stable dispersoids under He irradiation | [52] |
| 14YWT | 100 dpa $Ni^{2+}$ | 300-600 | Shrunk dispersoids, decreased density | [36] |

corresponding radiation damage. After mechanical polishing, the sample was cleaned with acetone in a Branson 1510 ultrasonic cleaner.

### *2.2.2 Electropolishing*

Mechanical polishing introduced a surface layer of stress. To remove this layer, electropolishing was employed. A schematic diagram of an simple electropolishing system as employed in this study was shown in Fig. 2.2. A round carbon bar was used as the cathode and the material to be polished was connected in as the anode. The solution was made with 0 vol. % of perchloric with methanol. Electropolishing was carried out at room temperature with a 2-3 volt voltage applied between the cathode and anode.

After mechanical and electro- polishing, the surface of the material is ready for irradiation. As shown in Fig 2.3, a polished sample used in this study has a surface free from scratches. Some pits are visible on the surface, which might be a result of defect, dislocations or grain boundaries that enhance etching rate during electropolishing. Yet, the area free from pits is still large enough to lift out TEM samples later.

## 2.3 Self-ion Irradiation

### *2.3.1 Study Radiation Damage Using Ion Irradiations*

To study the radiation response of materials under radiation for their potential use in a reactor, the ideal case would be introduce neutron irradiation with similar energy range and at similar temperature as the environment where the material will be serving. However, even for some high flux neutron source such as research fast reactors, the neutron damage rate would be in the order of $10^{-6}$ dpa/s, that is

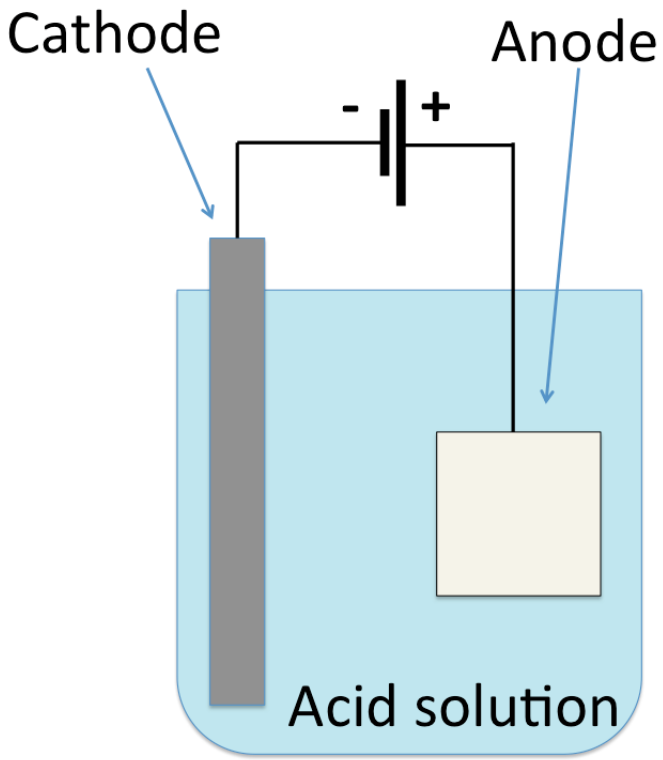


Figure 2.2: Schematic diagram of an electropolishing system

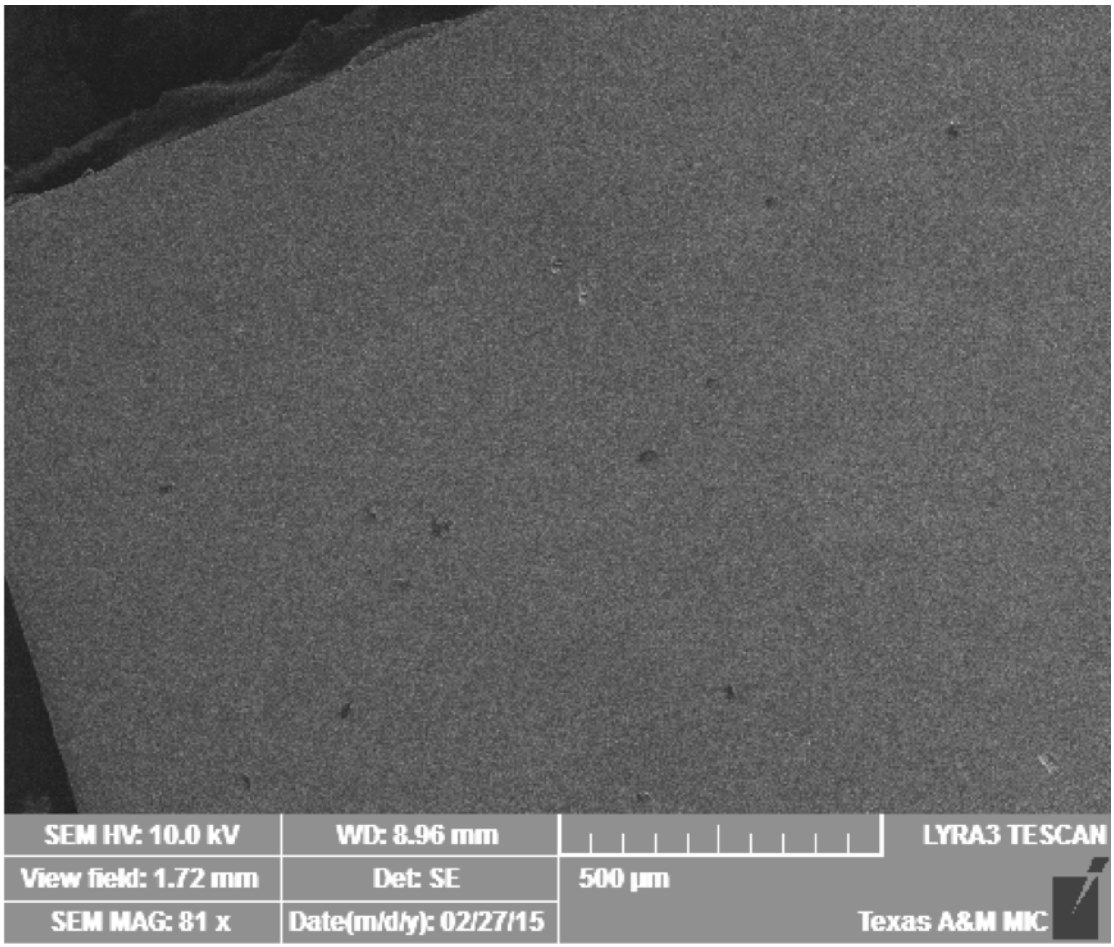


Figure 2.3: A secondary electron micrograph of an as-polished ODS sample before irradiation

approximately 10 dpa per year. On the other hand, as introduced in first section, generation IV reactors challenge the material at a dpa range of a couple of hundreds, and it would be a long period of waiting to use test reactors to accomplish such high damage level, not to mention that materials activated in the reactor need to be 'cool-down' for up to a couple of years before investigation can be done on them. Heavy ion irradiation produced by accelerators turns out to be an ideal choice to introduce high level of dpa damage within a short period of time. The choice of using heavy ion is made because it create damage cascade very similar to the case of neutron irradiation, as shown in Fig. 2.4 [6]. The dpa rate of heavy ion to material is in the order of $10^{-3}$ dpa/s, which approach $\sim$100 dpa in a day. As introduced in the first section, material degradations due to irradiation, such as swelling and strength changes, are strongly related to the total dpa received by the material. Thus, it was believed that by introducing ion irradiations with a higher dpa rate, some of the material degradation phenomena can be studied and compared to material degradations under neutron irradiation.

Yet, every coin has two sides. Heavy ion irradiation has some side effects that need to be considered, most of which were introduced due to its fast dpa rate and the implanted ions. As discussed in the first section, a peak in temperature exists for void swelling due to the kinetics of defect cluster and migration. Given a higher dpa rate, the corresponding kinetics need to speed up to match it, thus the peak swelling temperature will shift towards the higher end, as illustrated in Fig 2.5 [6]. Meanwhile, the absence of swelling near the damage peak of ion irradiation has been observed in many experiments. The defect imbalance and the injected interstitial effects are the reasons [53, 13]. The injected ions become interstitials that suppress the formation of voids. As the dpa peak region is closer to the injected ion range, in

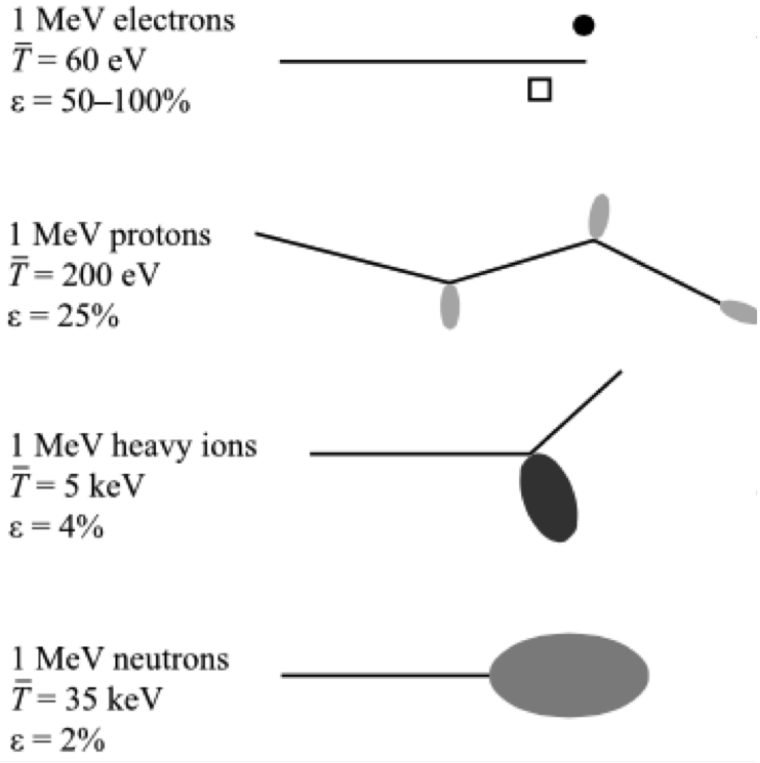


Figure 2.4: Schematics of damage cascades created by electron, proton, heavy ion and neutron bombardment [6]

general, swelling will be lower at the peak dpa region, as shown in Figure 2.6 [13]. In addition, faster dpa rate results in shorter annealing time per dpa. As a result, phenomena with low 'slower' kinetics might not be not sufficient or even not able to occur during ion irradiation, such as second phase formation, precipitating and segregation.

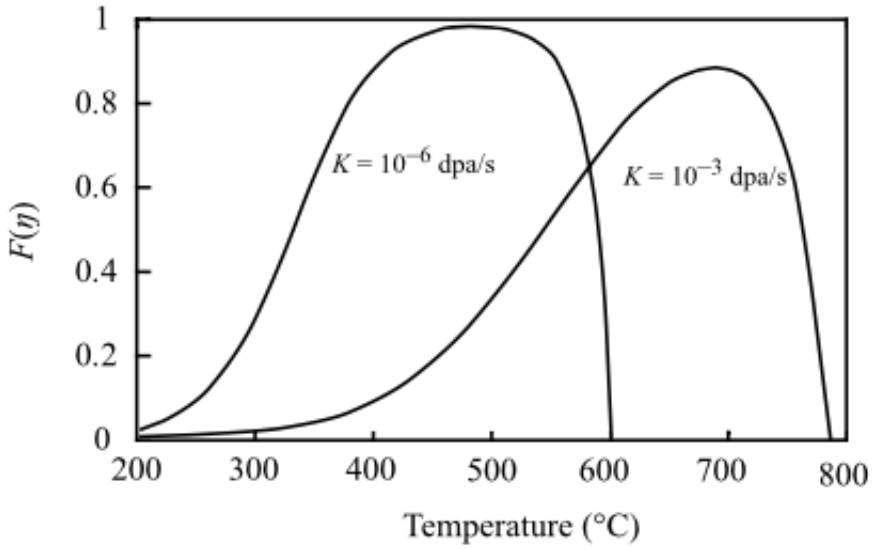


Figure 2.5: The shift of peak swelling temperature corresponds to increase in damage rate K [6]

### *2.3.2 1.7 MV Tandem Accelerator*

A 1.7 MV Tandem accelerator made by the General Ionex Corporation in 1983 was used for self-ion irradiations in this study, as shown in Fig. 2.7 and Fig. 2.8. Two different source heads were equipped to generate the ions used in various experiments, i.e., the Duoplasmatron and the Negative Ions by Cesium Sputtering (SNICS). Ions generated from the source were then fed to the main accelerating column. After

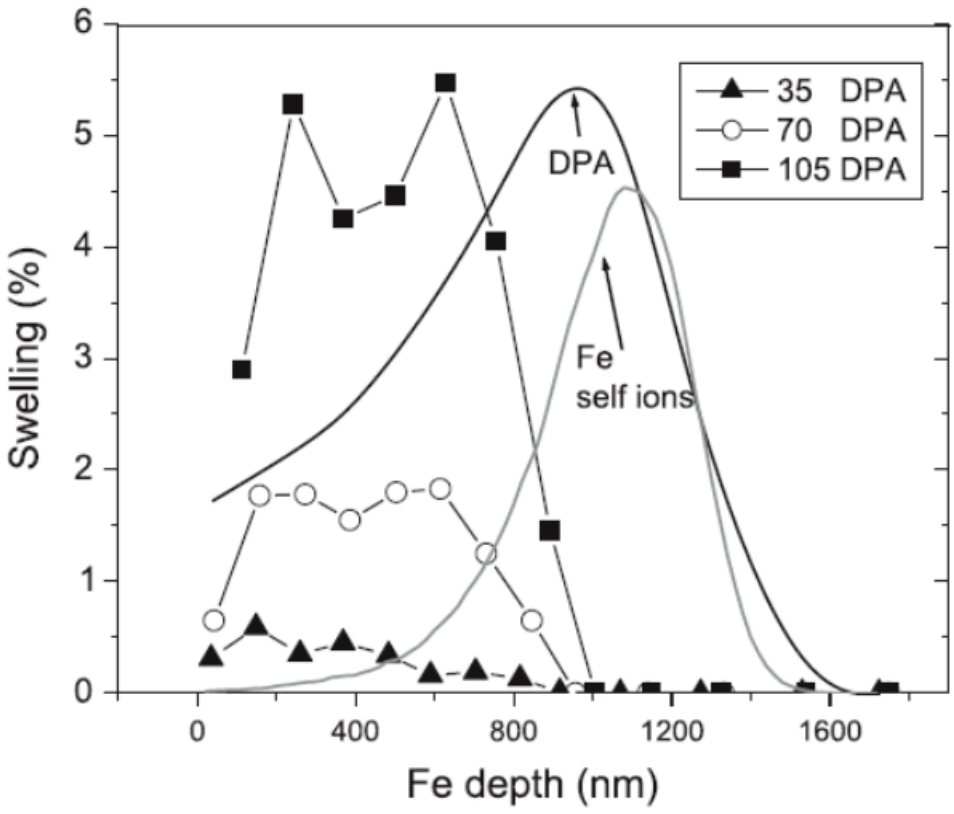


Figure 2.6: Depth distribution of void swelling in pure Fe irradiated with 3.5 MeV self-ions to different peak values [13]

being accelerated by the main terminal voltage, the ions are directed down a beam pipe to the implantation chamber, one of the three target chambers. It is convenient to isolate the accelerator into three main sections: low energy, main acceleration column, and high energy to better describe the accelerator.

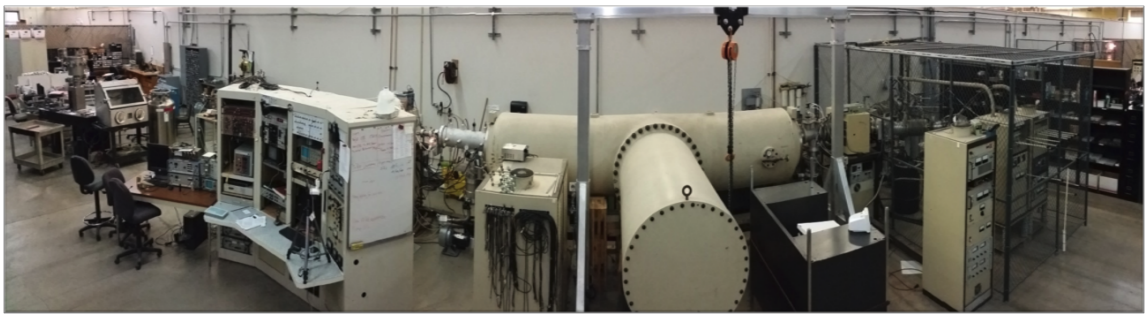

Figure 2.7: A photo of the 1.7 MV Tandem accelerator

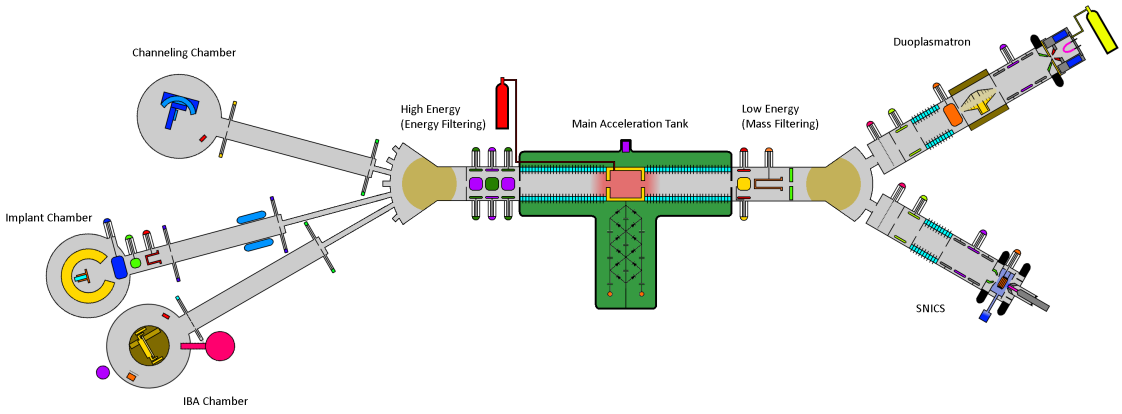


Figure 2.8: An overall schematic of the 1.7 MV Tandem accelerator

To carry out $Fe^{2+}$ irradiation, the solid source named SNICS was used. In SNICS,

a solid cathode was used as the source material for the ion beam it produces. This source has a great flexibility for all elements except the noble gases. Even for elements that cannot be found as a solid in pure form, they can still be produced through the use of compounds. A schematic diagram of the source including the beam optics and vacuum system is exhibited in Fig. 2.9.

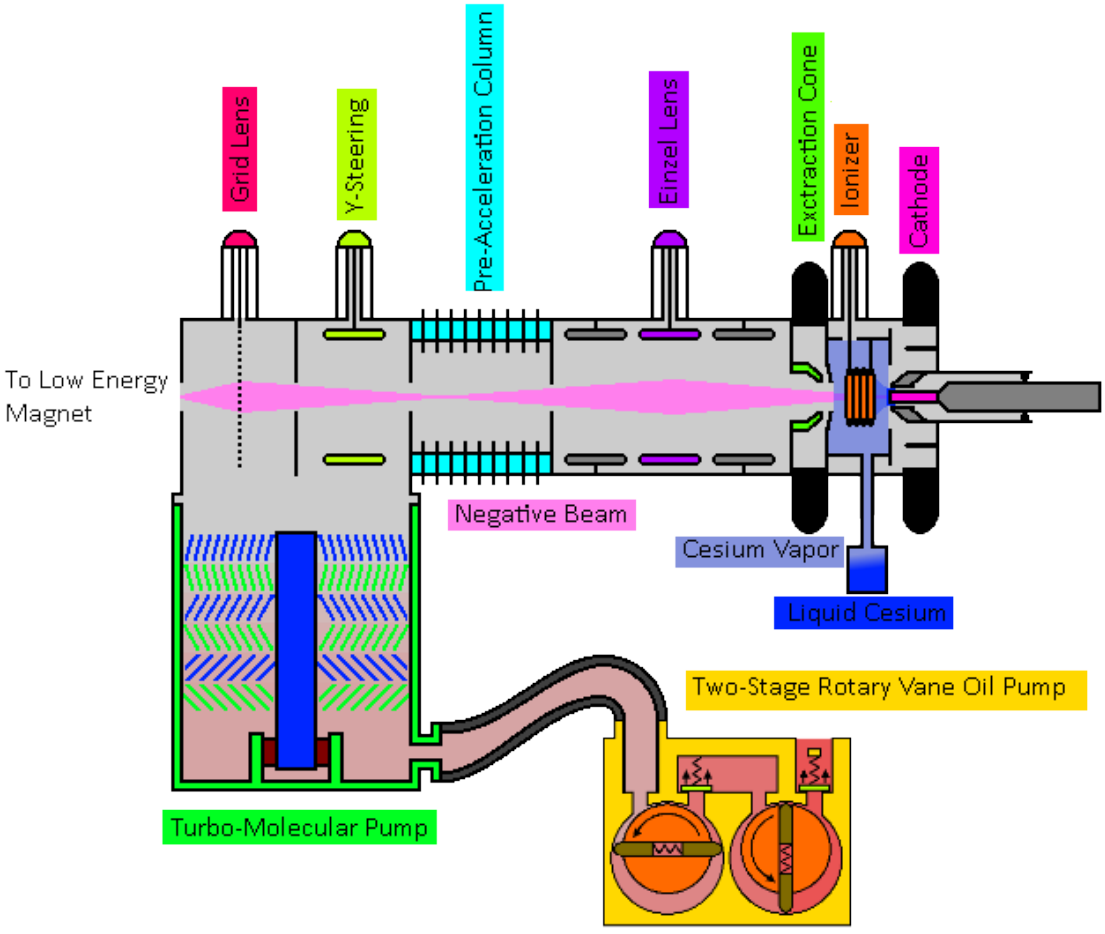


Figure 2.9: A schematic of the internal structure and the vacuum system of the SNICS ion source.

The source starts with the cathode sputtered by cesium. The cesium was stored in a reservoir below the source head in liquid form. When heated, some of the cesium become a vapor and travel up the chimney pipe. Some cesium will drift towards the target cathode, condense on the surface and form a thin layer, which is important to enhance the percentage of ions produces that are negatively charged. On the other hand, most of the cesium will travel into the ionizer chamber, where they cesium atom lose an electrons to become positively charged, through collisions with thermal electrons produced by the heated coil known as ionizer. The positively charged cesium will then be accelerated by the target voltage towards the cathode, depositing large mounts of energy in the near surface region and sputtering off the target material. When traveling through the thin layer of cesium, the sputtered target material atoms have a good chance to receive electrons and become negatively charged as they leave the cathode. These negatively charged ions are then accelerated with the target voltage, and then the extraction voltage. The extracted ions then go through the Einzel lens, which focuses the beam before they pass through the pre-acceleration column. This will add 40-50 keV of energy to the ions. This extra energy is essential later to resolve different elements using the low energy bending magnet. After gaining energy through the pre-acceleration column, ions travel through a set of electrostatic deflection plates and the grid lens, which help position the beam in the vertical direction and focus the beam before it is sent to the low energy magnet.

The bending magnet at the low energy end is the last major component before ions were sent to the main acceleration part. It performs several functions. Firstly, the magnet is able to switch polarity, so that ion beams produced from both the SNICS and Duoplasmatron sources can be bent to travel down the main acceleration column. Secondly, the low energy magnet provides the main horizontal direction

control in the low energy system. Thirdly, the low energy magnet performs a mass filtering function, as illustrated in Fig. 2.10. This graphic shows the beam passing through the magnet, filtered by the low energy magnet.

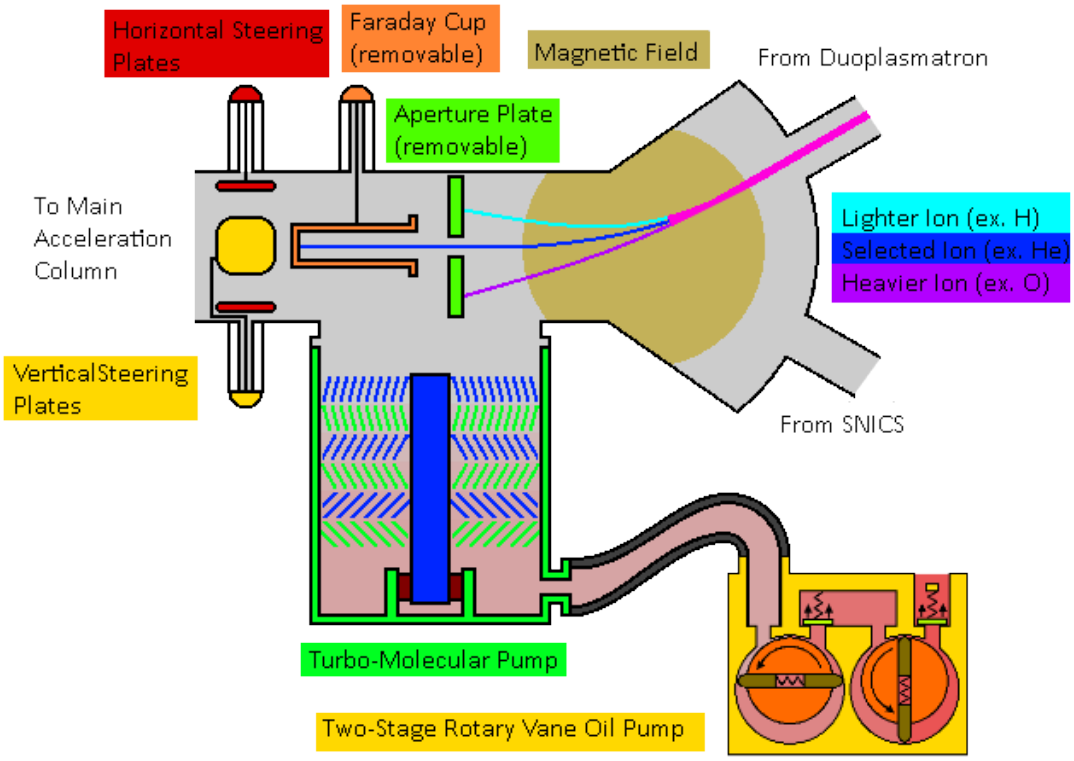


Figure 2.10: A schematic showing the internal structure and operation principles of the low energy magnet.

The main acceleration column provides most of the energy of the ions. In this part, the beam is exposed to very high voltages, resulting in the acceleration of the ions to their desired energy. The 1.7 MV used in this study is a tandem type accelerator with a maximum allowable voltage of 1.7 MV. Figure 2.11 exhibits a schematic

of the main acceleration column.

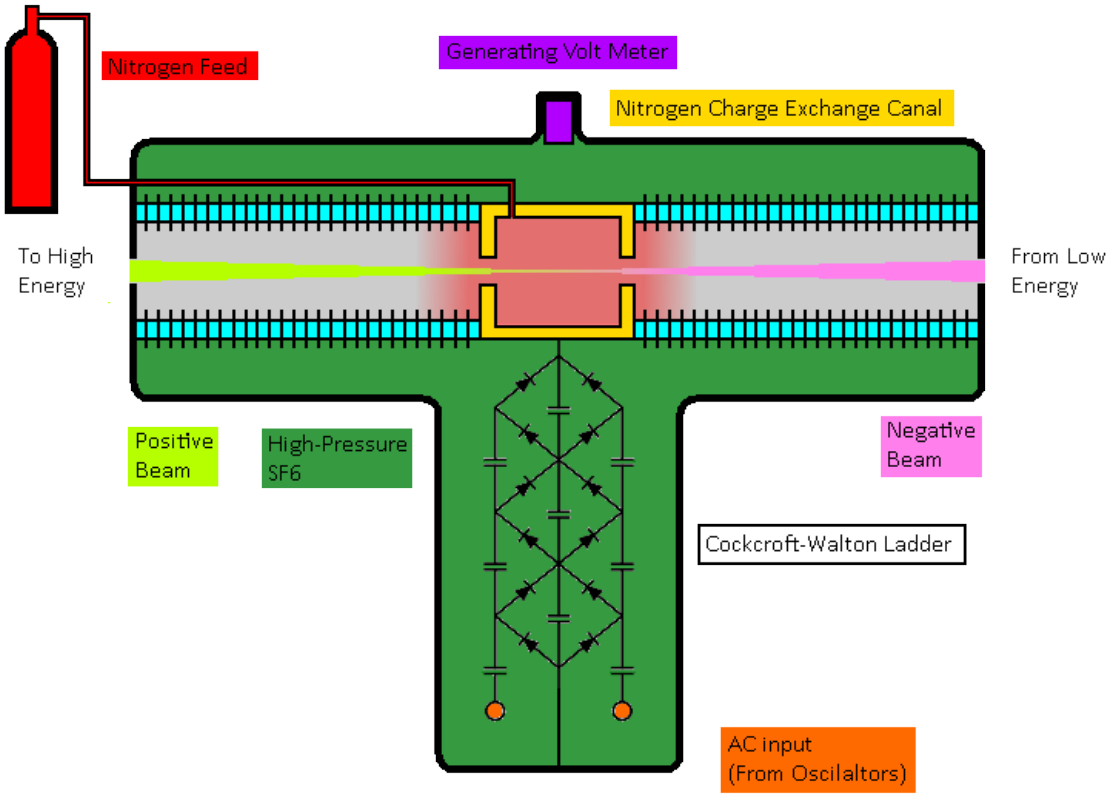


Figure 2.11: A schematic of the internal structure of the main acceleration column

The tandem configuration is named after the positioning of the two acceleration columns that contained in this design. As shown in Fig. 2.11, the beam passes one column and then another. Each column has a series of metal plates separated by ceramic standoffs and connected to its directly adjacent neighbors by a series of high-value resistors. Between these two columns, there is a nitrogen stripper canal where

the vital charge-exchange operation takes place.

Ions passed to the main acceleration tank are negatively charged. They are then attracted to the positively biased terminal, accelerating along the first column. Once they reach the center they enter the charge exchange canal, which contains high pressure nitrogen gas. The gas is fed in at a very low rate, controlled by a leak valve. The negative ions interact with the gas, so that their electrons get striped and become positive. These now positive ions will be repulsed by the positive terminal voltage and pushed down to the second beam tube, where they get more energy.

The accelerated ions then come to the high energy equipments, as schematically shown in Fig. 2.12, including the high-energy beam optics and the various target chambers. The high energy beam optics are very critical for directing the beam and controlling its shape. The beam is unfocused after traversing the nitrogen stripper canal. A quadrupole is immediately after the main acceleration column to shape the beam. Properly shaped beam continues to the high energy magnet which directs the desired energy beam to the correct beam line. Three chambers are installed in the 1.7 MV Tandem accelerator, i.e., the implantation chamber, the ion beam analysis chamber, and the channeling chamber.

Immediately after the main acceleration tank, the beam enters the X-Y focusing quadrupole. This element is designed to focus a divergent beam in the vertical and horizontal direction independently, resulting in a focused beam with a controllable shape. The focused and shaped beam then enters the high-energy bending magnet. Like the low energy magnet, the high-energy magnet also performs several important tasks. First, it directs the beam down the beam pipe to the chamber to be

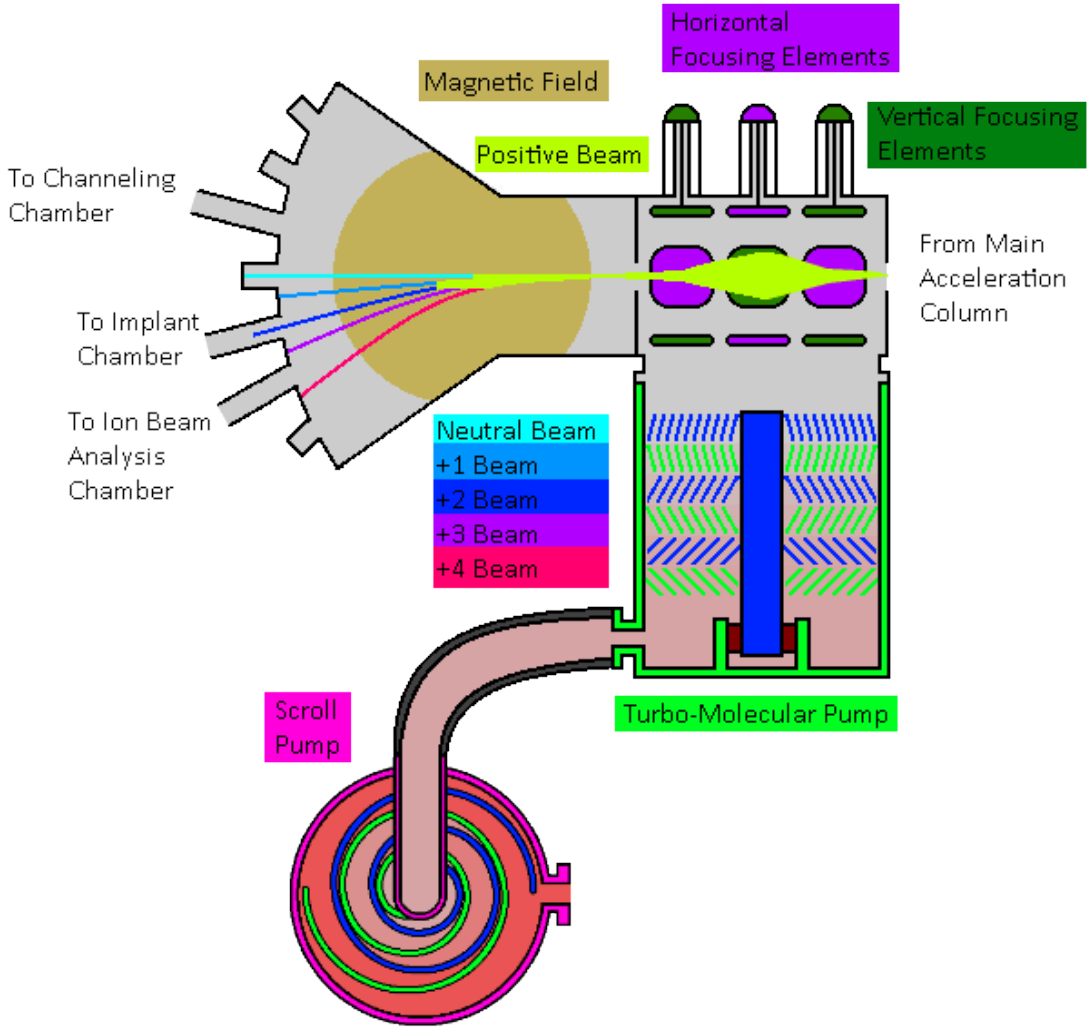


Figure 2.12: A schematic diagram of the magnet and focusing elements located next to the main acceleration column of the 1.7 MV tandem accelerator

used for the experiment. Second, this magnet also performs energy filtering of the beam. Due to the creation of many charge states in the nitrogen stripper canal, the accelerated beam after the main acceleration column is a mixture of ions with different charge states, and thus, different energies. By altering the strength of the magnetic field, ions with different charge states and therefore different energies will be bended differently angle-wise. And thus, certain charge state can be selected, as illustrated in Fig 2.12. With the beam filtered by the high energy magnet, it is sent to the chamber to achieve the experimental goal.

In this study, the material irradiations were done in the implantation chamber, as exhibited in Fig. 2.13. This chamber is equipped with a room temperature or hot stage, and is setup to perform uniform implantations on samples, either by rastering the beam through a set of raster coils located approximately 3 feet before the chamber, or be defocusing the beam from the X-Y focusing quadrupole. The hot stage is designed to maintain samples at an elevated temperature up to 750 °C for implantations. Due to this high heat load in the chamber, a water-cooled shroud is installed around the heated stage to reduce the heating of the chamber. The implantation chamber is installed on the left hand side 11 degree beam line. This smaller angle has been chosen to allow for heavier ions with higher energy to pass.

Figure 2.14 is a photo of the home-made hot stage used for high temperature irradiations with samples mounted. A 150 watt cartridge heater was installed behind the copper stage as the heating source. Thermal couples were connected to the back of the copper stage for temperature readout. The accuracy of temperature control of this system has been confirmed with infrared camera measurements. The temperature accuracy is below ± 10 °C. This hot stage system can heat the samples

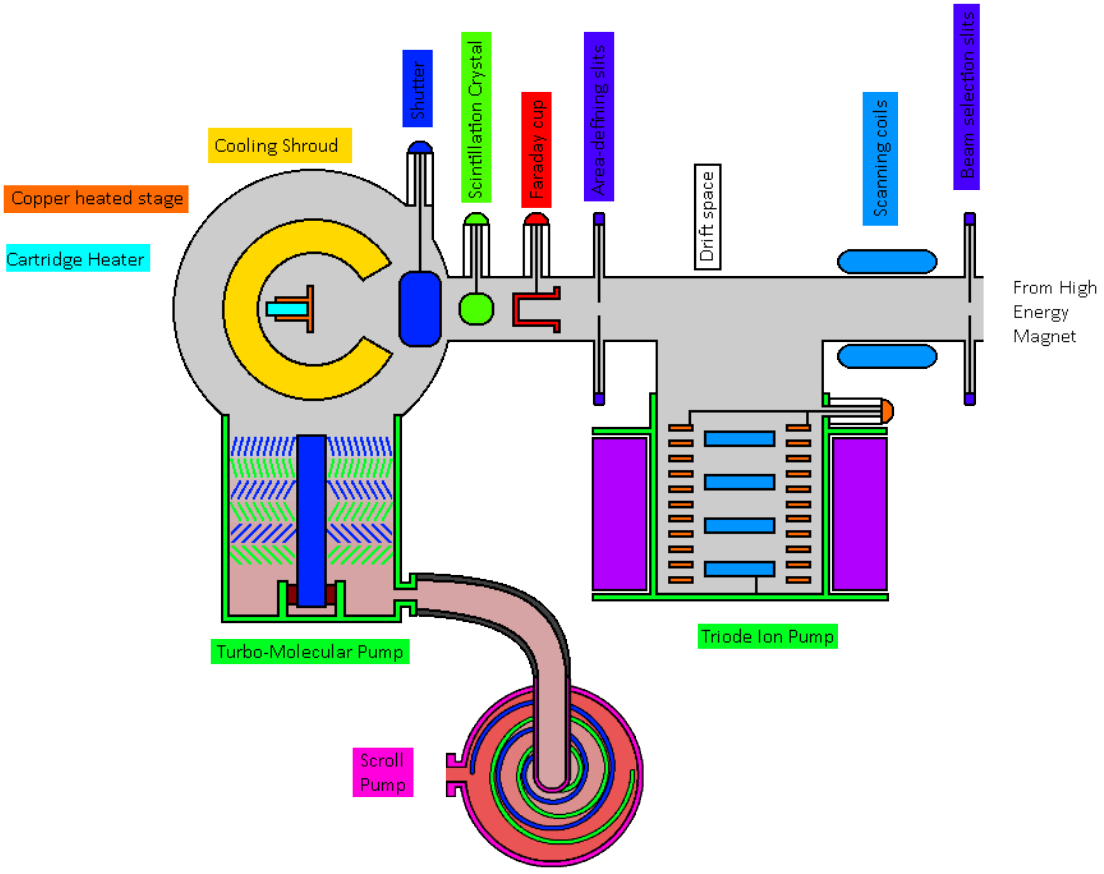


Figure 2.13: A schematic of the implantation chamber including stage geometry and cooling shroud.

up to 750 °C+ and is compatible with a vacuum better than $10^{-6}$ torr. The samples were mounted to the hot stage with high-temperature compatible silver paste.

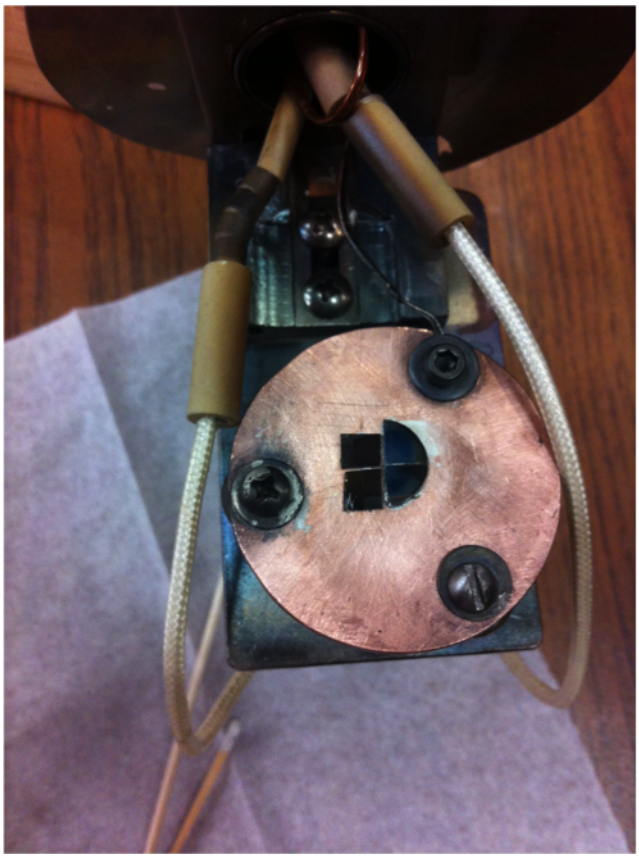

Figure 2.14: A photo of the hot stage used in this study for high temperature irradiations with samples mounted

### *2.3.3 The Experiment Matrix*

Figure 2.15 displays the irradiation matrix of this study. Three elevated temperatures from 325 to 625 °C were chosen with a highest peak dpa of 800. Dose dependence study was carried out using samples irradiated at 475 °C with increasing

radiation damage from 100 peak dpa to 800 peak dpa. The temperature of 475 °C was chosen because it is close to the peak swelling temperature, based on previous F/M steel radiation response data [54, 55, 56, 5]. As will be discussed in later sections, investigations are usually carried out in a half-peak dpa region rather than the peak dpa region. As a results, we should gain some solid data for damage level higher than 400 dpa. Such damage level is still sufficient to predict the behavior of the material in most cases for Generation IV reactors.

Three irradiation temperatures, i.e., 325, 475 and 625 °C were chosen to induce damage up to 200 dpa at. It is well known that kinetics such as diffusion is strongly influenced by temperature, thus, by comparing the responses of different temperature irradiation, some kinetics of microstructure evolution under radiation conditions can be understood.

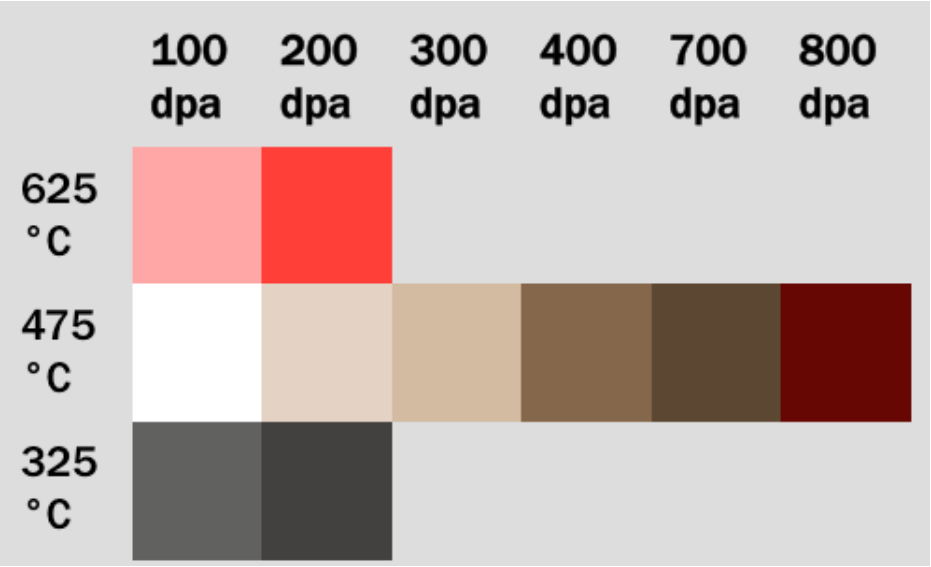


Figure 2.15: Irradiation matrix of this study

## 2.4 TEM Specimen Preparation

### *2.4.1 General Used Methods*

As will be shown later in this section, TEM images with electrons transmitted through the sample. In general, the electron energy of most commercial TEM is in the order of hundreds keV. In order to allow the electron to transmit the sample, the thickness of the sample should be well-controlled. In this study, we used 200 keV electrons, which requires the thickness of the F/M alloy samples to be ∼100 nm or below. In practice, preparing such a thin-lamella-type sample without breaking it requires techniques with great accuracy and reliability. Although we used the technique called focused ion beam lift-out, a review of most-used TEM sample preparation methods is provided in this section.

In general, the preparing of ultra-thin sample involves a mechanical thinning that reduce the thickness of the sample to a reasonable thickness, i.e., a couple of microns, followed by a more gentle and usually slower technique that reduce the thickness of the sample to the desirable value without producing much damage to the material. Three methods would be introduced later including dimpling and ion milling, electro chemical polishing, and focused ion beam. The fist two usually involve the mechanical thinning at the beginning. While the first and third techniques achieve the final thinning through ion bombardment, the second technique uses chemical reaction to remove the sample and reduce the thickness.

Dimpling and ion milling: dimpling is a common method to mechanically reduce the thickness of the sample. Before dimpling, the sample is usually cut into a 3 mm disk and ground to a thickness of ∼100 microns. Figure 2.16a shows the dimpling

mechanism [14]. The sample mounted on the platen of specimen stage rotates with the stage. On top of the sample, the rotating grinding wheel will remove the sample. So that the sample will have a thin region in the center, as shown in Fig. 2.16b [14]. The removing rate of a dimpling grinder is usually controlled by the weight of the grinding wheel. Thus, the condition of the grinding wheel is very critical to the success of dimpling. Uneven wheel surface increases the vibration during dimpling, which leads to deformation or fracture of the sample.

The dimpled sample can then be further thinned to be electron transparent using ion milling technique. Figure 2.17 exhibits the principle of ion milling. Argon ( Ar) gas is ionized and accelerated to an energy in the order of eV in the ion source, which bombards the sample at an glancing angle. The sample rotates so that eventually a hole surrounded by electron transparent thin regions would form in the center of the sample. The thinning rate can be controlled through the ion accelerating voltage, ion current and the incident angle. High voltage and/or current might results in undesirable damages in the sample due to the deeper penetration depth of higher energy ions and more deposited thermal energy with higher current of ions.

Electro chemical polishing is another general used method applied to conducting materials such as metals and semi-conductors. It is based on electro chemical dissolution of the material. By controlling the solute, the temperature and the voltage, the dissolution rate can be well-controlled and a electron transparent sample that is totally free from ion damage, as produced by ion milling, can be prepared.

Like for ion milling, the sample prepared for electro chemical polishing is usually a 3 mm disk with a typical thickness of 50-200 microns. Electro chemical polishing

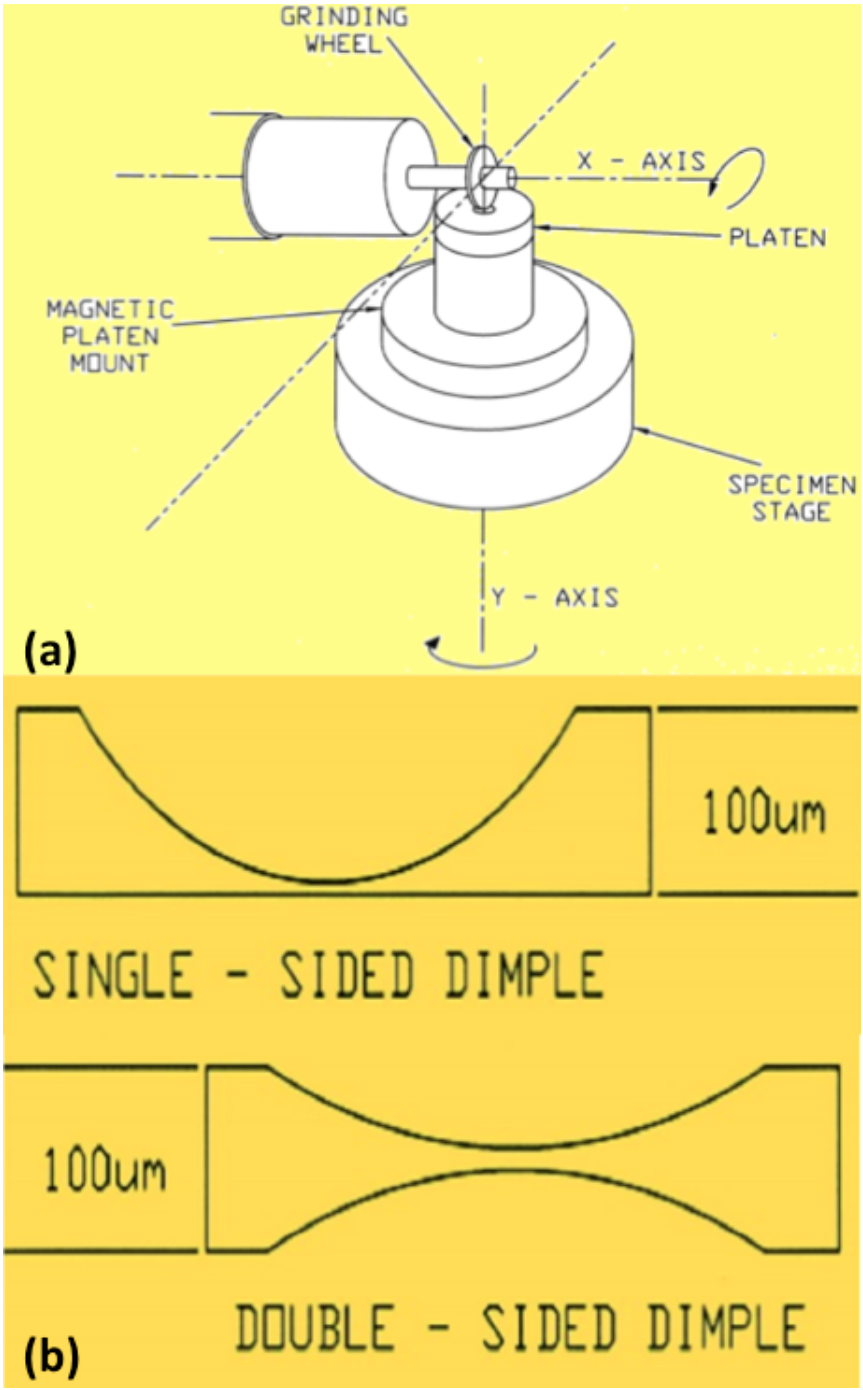


Figure 2.16: (a) A schematic representation of the mechanism of dimpling, (b) samples after single-sided dimple and double-sided dimple, shown on the top and bottom, respectively [14]

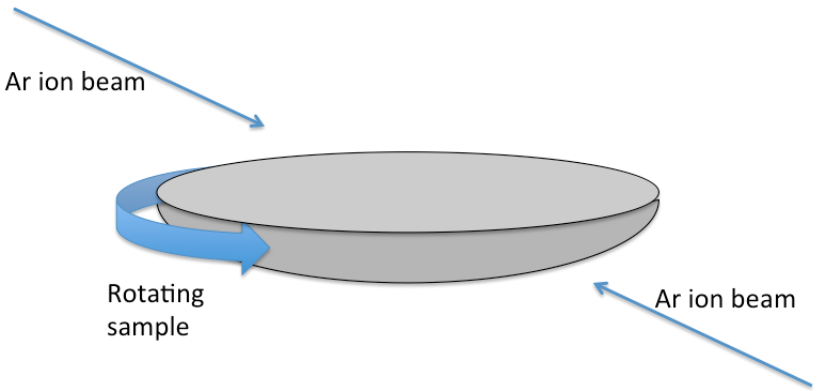


Figure 2.17: A schematic representation of the mechanism of ion milling

can be conducted using a jet-polisher. A schematic of a jet-polisher is shown in Fig 2.18 [15]. When thinning the sample with a jet-polisher, a positive voltage is applied to the sample disk, so that the sample is anode. Current control is applied through controlling the current of solution targeting the center of the disk from each jet nozzle. When a perforation formed in the center of the sample, a light beam emitted from one side of the sample will be detected by a photocell on the other side of the sample, which triggers the end of the polishing.

While the technique of FIB will be discussed in detail later, the pros and cons of each TEM specimen preparation method is summarized in table 2.2. In this study, FIB technique was chosen primarily because of its capability to lift-out a cross-sectional specimen that includes the full damage range and irradiation-free region of an ion-irradiated sample.

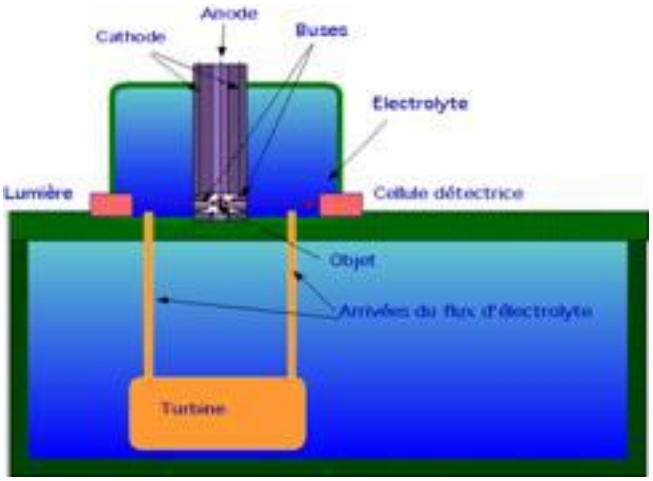


Figure 2.18: A schematic representation of an electronic twin jet-polisher [15]

Table 2.2: Comparison of different TEM specimen preparation methods

| Method | Advantages | Drawbacks |
|---|---|---|
| Dimpling and ion milling | applicable to a wide range of materials; large electron transparent region | mechanical damage from dimpling ;ion-induced damage and increase in temperature during ion-milling |
| Electro chemical polishing | damage free sample; large electron transparent region | selective dissolution may occur for sample having different chemical compositions or precipitates |
| FIB lift-out | accurate control of lift-out region; reduced magnetism effect from magnetic samples | limited region of observation; ion-induced damage |

### *2.4.2 Focused Ion Beam*

As shown in Fig. 2.19, modern FIB is usually combined with a SEM to become a dual-beam system, where both electrons and ions can be used to generate secondary electrons for imaging. Meanwhile, ion beam is used to bombard and remove the materials, or to deposit materials on the surface of the materials. Nano-sized structures can be created using this technique. When using FIB to prepare an electron transparent lamella for TEM investigation, it is incomparable by any other technique in making a specimen from any desirable features that are visible in secondary and/or backscattering electron micrographs, i.e., a grain boundary, a certain phase, precipitates etc.

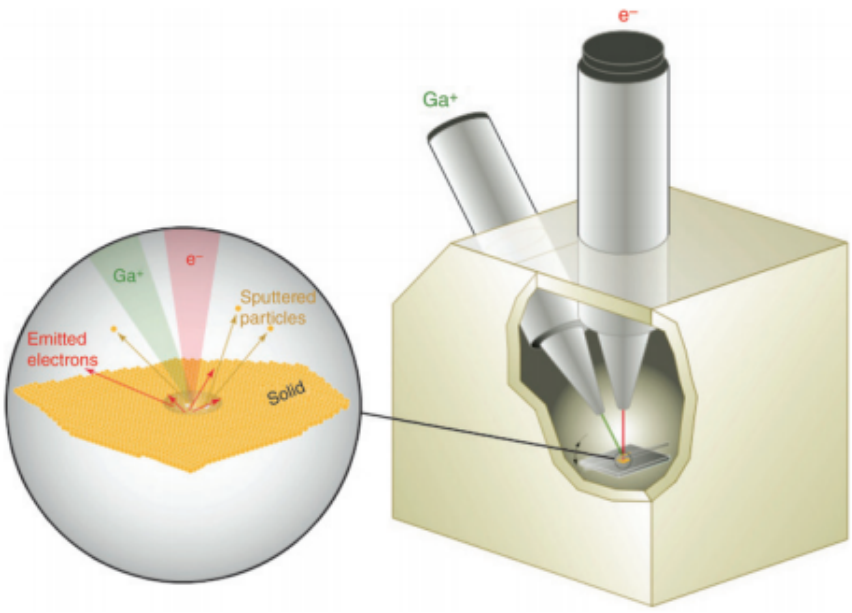


Figure 2.19: A schematic representation of a FIB-SEM dual-beam system [16]

In this study, the TEM lamellas were lifted out from the irradiation surface, so that a cross-sectional TEM specimen can be prepared with the whole irradiation damaged region as well as irradiation-free region. Figure 2.20 illustrates that in a FIB lifted-out TEM specimen of ion-irradiated sample, the irradiation layer is marked by the protection layer, and the whole damage region predicted by the dpa profile calculated by SRIM is included. A detailed procedure of TEM specimen lift-out using TESCAN LYRA FIB-SEM can be found in the appendix of this dissertation. It is worth to note that since TESCAN and FEI are using different nano-manipulator and gas-injection-system, the lamella lift-out procedures are slightly different. Especially for TESCAN LYRA system if nano-manipulator or gas-injection-system is recalled to near-sample and the stage is 0 degree tilted at eccentric height, a collision might happen leading to damage of equipment.

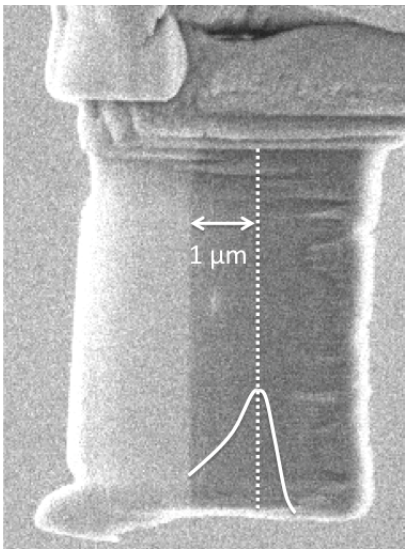


Figure 2.20: A FIB lifted-out lamella reflecting radiation response of the whole damage profile

## 2.5 Microstructure Investigation

A strong relationship has been found between material property and microstructure. Researchers have been enhancing material properties through microstructure engineering. For example, grain boundary engineering has shown to contribute to the hardness of F/M steel as well as the swelling resistance under irradiation, and introducing dispersion to material can improve its strength, as introduced in last section. Investigating microstructure changes of the 12Cr dual-phase ODS alloy before and after irradiation would be the most important effort in this study. Three microstructure level changes due to irradiation would be particularly addressed, i.e., grain and sub-grain structure stability, nano dispersion stability, and void swelling. The presence of high density grain and sub-grain boundaries and nano dispersoids are critical to the material hardness and creep strength; void swelling resistance is a key factor for material designed for nuclear use.

There are a few microstructure analysis techniques that are widely used, for example, TEM, SEM, atom probe tomography (APT), etc. TEM based techniques were used in this study and would be introduced in detail later. Using secondary electrons, backscattering electrons, and characteristic X-rays generated by $\sim$30 keV incident electrons on the surface of the material, SEM provides characterizations of the whole surface of the sample, with a spacial resolution of $\sim$10 nm. The depth of the sample from the surface that would contribute to the characterization is illustrated by the interaction volume of electron as shown in Fig. 2.21 [17]. In general secondary electrons are generated in the near surface of less than 0.1 micron depth, while backscattering electrons and characteristic X-rays have deeper penetration ranges. These ranges increase with increasing incident electron energy and usually decrease

with increasing atomic number.

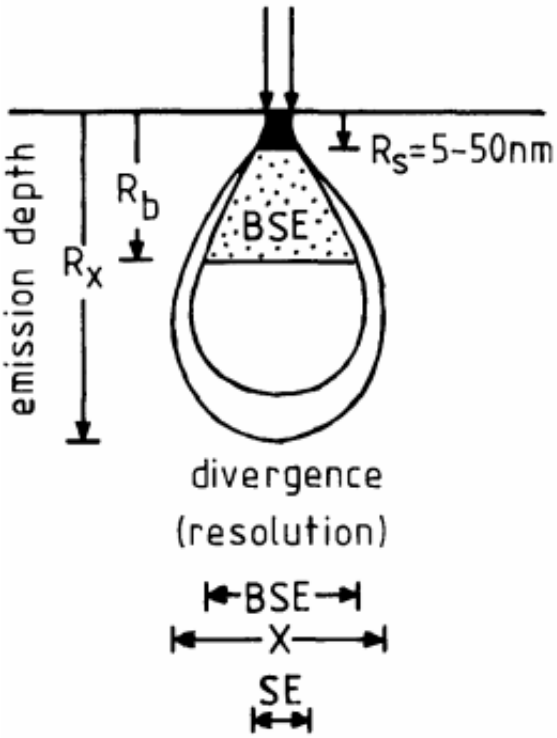


Figure 2.21: Interaction volume of electron to a material with low to medium atomic number [17]

APT is a material analysis technique offers 3 dimensional chemical composition measurements and imaging at atomic scale. A sample prepared to be a sharp tip of diameter of ∼50 nm is biased at a high voltage of 5-20 kV, creating a very strong electrostatic field at the tip surface, which is just below the atom evaporation point. On the top of the tip, usually a laser is used to evaporate a controlled amount of atoms from the surface, which ionized are projected onto a high-efficiency position sensitive detector (PSD) by the electron field. The time of flight of the ions as well

as their projection position on the PSD are recorded and used to determine the mass to charge ratio of the atom and to reconstruct the original location of the atoms in the tip sample.

### *2.5.1 Transmission Electron Microscope*

As would be shown in the following sections, TEM techniques were used in this study because of the following advantages:
(1) grain boundaries, nano-sized dispersoids and voids can be imaged; while nano-sized dispersoids and voids are below the resolution of SEM, and APT is not appropriate to study voids due to its reconstruction mechanisms.
(2) Electron diffraction and high resolution transmission electron micrograph (HRTEM) can be used to study the crystal structure, interfacial coherency of nano-dispersoids. To the author's best knowledge, there is no other techniques can do such a job.
(3) Chemical composition of even nano-features can be studied using energy-dispersive X-ray spectroscopy (EDS) and electron energy-loss spectroscopy (EELS).

Figure 2.22 schematically show the operation of TEM to incident parallel electron beam onto the sample [18]. In this study, most of the micrographs, including bright field (BF) images, dark field (DF) images, electron diffraction patterns, HRTEM, EELS mappings, were obtained in a parallel-beam operation. Monochromatic electrons are produced by the electron gun system, the core part of which is a field-emission gun in the FEI F20 TEMs used in this study. two condenser lenses (C1 and C2 as shown in Fig 2.22) are adjusted to illuminate the TEM sample with a parallel beam.

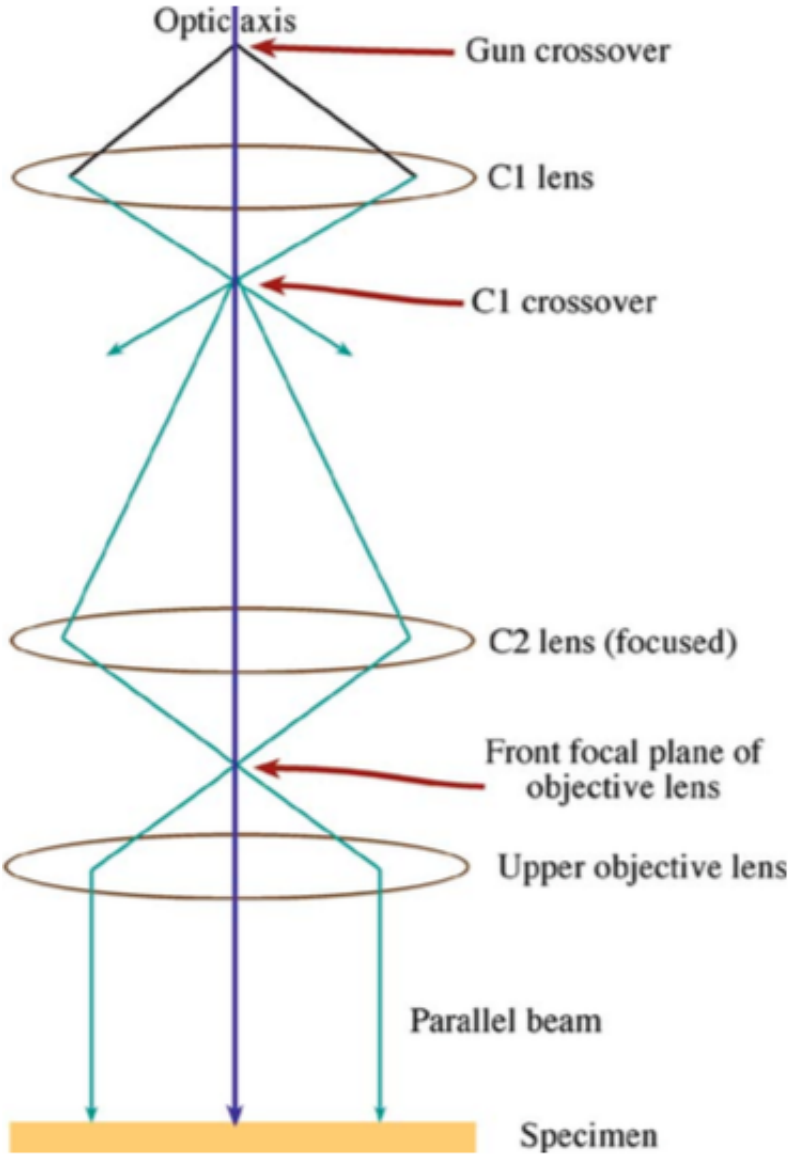


Figure 2.22: The practical parallel-beam operation in TEM [18]

### *2.5.2 Diffraction Pattern, Bright Field, and Dark Field*

When electron passing through the sample, those low-mass and charged particles are easily scattered by the positive nucleus of the atoms in the sample. That is also the physics that make TEM feasible. In Fig. 2.23, after the parallel beam passing the sample, some electrons are still traveling with unchanged direction, as schematically shown by the maroon and pink lines representing the direct beams; while some electrons get scattered and changed their direction of traveling, as illustrated by the blue, purple, green and orange lines representing the diffracted beams. Diffraction patterns, bright field micrographs and dark field micrographs are all imaged using (some of) these direct or diffracted beams.

When forming diffraction patterns, the directions of the scattered beams, in respect to the direct beam, are projected to diffraction spots in a typical diffraction pattern, which would be shown in later sections. As shown in Fig. 2.23A, electron beams that travel in parallel directions after passing the sample are converged to a same spot on the screen, demonstrating that in diffraction patterns, each spot reflects a type of diffraction due to electron-sample interactions. With knowledge of electron-atom interaction and crystallography, the structure information such as crystal structure, lattice parameters, grain boundary types, coherency between precipitate and matrix, etc. can be understood through diffraction patterns.

As shown in Fig. 2.23B, by adjusting the intermediate lens, its object plane becomes the image plane of the objective lens. As a result, a image of the sample is projected to the screen. When taking micrographs in image mode, the objective aperture is usually inserted. If the objective aperture is positioned so that the central

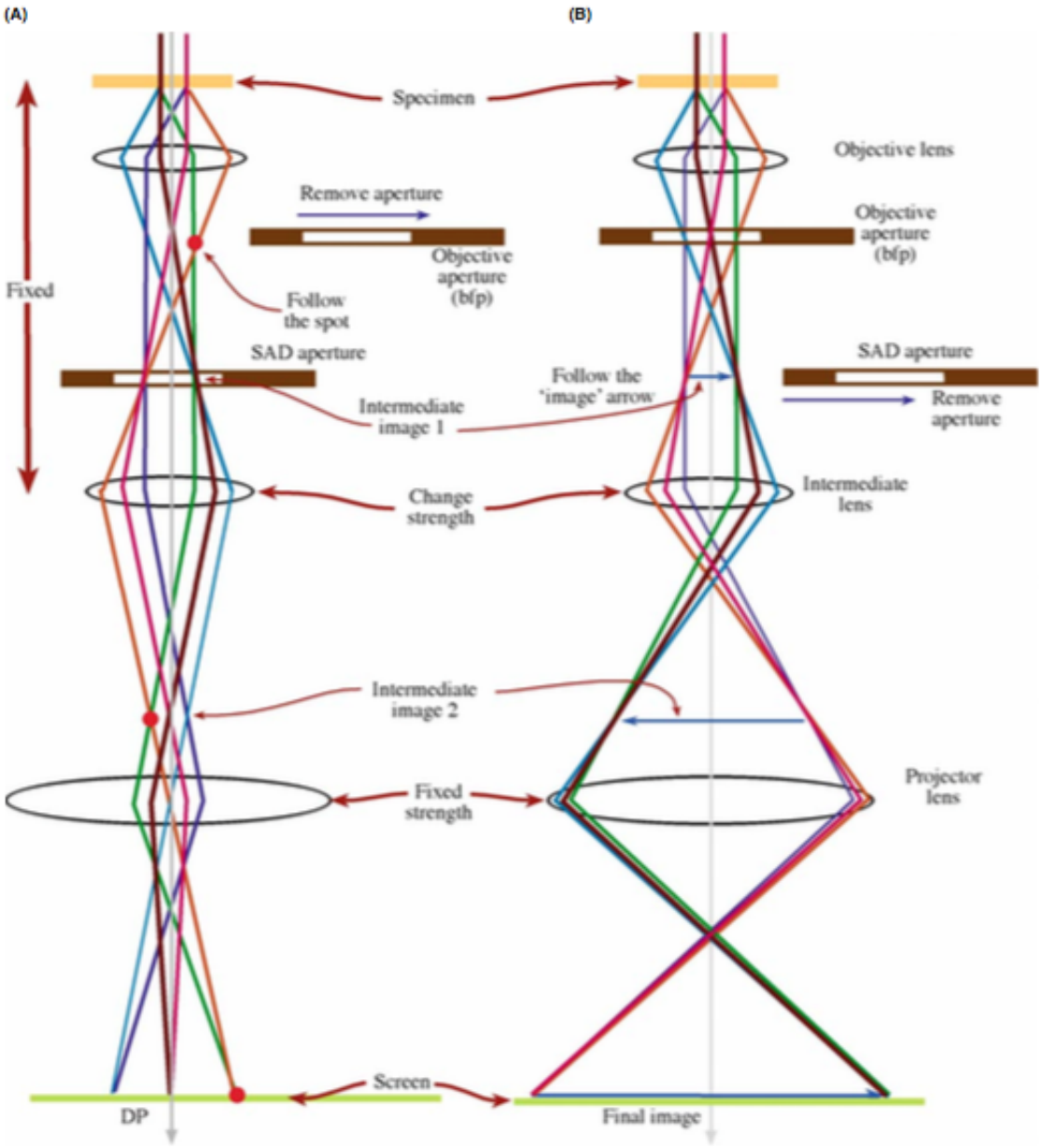


Figure 2.23: Schematics showing (A) the diffraction mode operation and (B) the image mode operation [18]

direct beam is passing through it while the high-angle diffracted beams are not, a BF image with enhanced contrast can be obtained. The features diffracting more electrons are darker because less electrons contribute to the BF image.

On the other hand, when obtaining a DF image, the objective aperture allows only one or a few diffraction beams to pass, and the direct beam is blocked. In this scenario, most of the as-obtained micrograph is dark and only features that diffracting electrons towards the directions corresponding to the selected diffraction beams appear bright. Examples of BF and DF images and analysis work done with them would be shown in the following sections.

### *2.5.3 Chemical Composition Analysis*

Two techniques are generally used in TEM for chemical composition analysis. They are EDS and EELS. The principle of EDS is the same as it is in the SEM. Characteristic X-rays are generated when the material is bombarded with electrons. By collecting the characteristic X-rays and associate their energy with the element's characteristic energies, the element type can be determined. A EDS spectrum obtained in at a dispersoid in the 12Cr dual-phase ODS would be presented in next section. As the electron can be converged to a smaller size in TEM compared to SEM, the spacial resolution of EDS obtained in TEM is better.

EELS is based on the electron energy loss due to inelastic scattering with an atom. Although the physics between EDS and EELS are different, the amount of energy-loss due to inelastic scattering can also be 'characteristic' of an element. Inelastic interactions between electrons and an atom include Cherenkov radiation,

inner shell ionizations, plasmon excitations, phonon excitations, inter and intra band transitions. Among them, through inner shell ionization, the electron in the inner-shell of the atom will receive a certain amount of energy from the incident electron to get ionized. As a result, the incident electron will lose approximately this amount of energy due to the inner shell interaction. The amount of energy-loss then, is characteristic to the element. EELS technique is better at determining elements with lower mass numbers. For example, the amount of C can be better determined using EELS rather than EDS. Besides chemical composition determination, EELS technique is also used to determine the sample thickness. Figure 2.24 displays a typical EELS spectrum showing the 'characteristic' ionization edges [18].

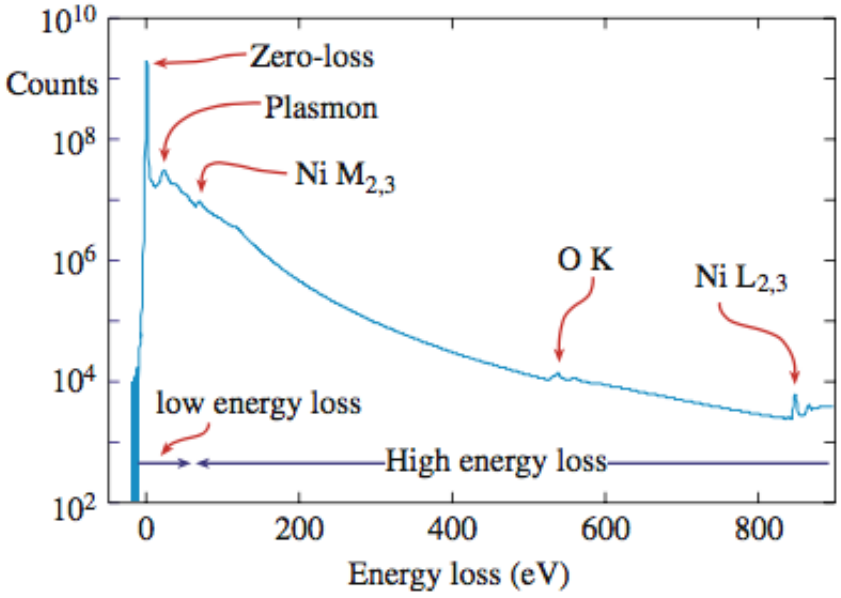


Figure 2.24: A typical EELS spectrum showing Zero-loss peak, plasmon peak and ionization edges [18]

# 3. THE 12CR DUAL-PHASE ODS ALLOY*

A dual-phase 12Cr ODS alloy, with improved corrosion and high temperature oxidation resistance compared to 9Cr alloys, has been designed and fabricated by our collaborators S. Ukai, et al. at Hokkaido University. The majority of tempered martensite phase also makes the material promising for void swelling resistance. In this section, we provided microstructure investigations of the samples. Radiation tolerance test results will be reported in the following sections. Both smaller tempered martensite grains and larger ferrite grains were found in this material, with a area ratio of approximately 4:1. Dispersoids were present in both ferrite and tempered martensite grains, with the latter having a wider range of dispersoid sizes, and a lower dispersoid density. In both phases dispersoids $> 10$ nm in diameter are incoherent with the matrix, while smaller dispersoids are coherent.

## 3.1 Material Design and Fabrication

### *3.1.1 Chemical Composition Determination*

The 12Cr ODS was designed and fabricated at the Department of Material Science and Engineering, Hokkaido University. In general, 12Cr alloys have designed to have better corrosion resistance than 9Cr alloys, but suffer less from $\alpha$' brittleness. Specifically, this 12Cr ODS was designed to involve dispersoids in both ferrite and tempered martensite phase [20]. This dual-phase alloy has a majority of tempered martensite phase and a minority of ferrite, at a ratio of $\sim$4:1. The amount of ferrite

*Part of the data reported in this section is reprinted with permission from "Microstructural changes and void swelling of a 12Cr ODS ferritic-martensitic alloy after high-dpa self-ion irradiation" by T. Chen, E. Aydogan, J.G. Gigax, D. Chen, J. Wang, X. Wang, S. Ukai, F.A. Garner, L. Shao, 2015, Journal of Nuclear Materials, 467, 42-49, Copyright [2015] by Elsevier B.V.

phase, consisting of thermally equilibrium ferrite and residual ferrite, was optimized at $\sim 20\%$ to enhance its creep rupture strength [19, 20, 57].

The composition of the 12Cr ODS dual-phase F/M alloy is provided in table 3.1. Elemental powders were mechanically alloyed in an argon gas atmosphere and consolidated at 1100 °C for 120 minutes. The consolidated specimens were then hot-extruded at 1150 °C, normalized at 1050 °C for 60 minutes before tempering at 800 °C for another 60 mints hour. More extensive details of alloy synthesis have been reported by Ukai et. al [20]. The amount of excess oxygen (O) and titanium (Ti) was specially designed to enhance the strength of the material by achieving ultra-fine nano particles ($\sim$2 nm) through element-compositional control, as shown in Fig 3.1 [19]. The ultra-fine nano particles were critical for to the material strength. Finer particles with a higher density are better at pinning dislocations, so that the grains with finer and denser dispersoids would be harder. Later we would show that ferrite phase preserves the particle distribution, leading to harder grains compared to tempered martensite grains [19].

Table 3.1: Composition of the as-received 12Cr dual-phase ODS alloy [21]

| Component: | Fe | C | Cr | Ni | W | Ti | N | Ar | $Y_2O_3$ | Excess O |
|---|---|---|---|---|---|---|---|---|---|---|
| Weight %: | 85.74 | 0.16 | 11.52 | 0.34 | 1.44 | 0.28 | 0.007 | 0.006 | 0.36 | 0.144 |

### *3.1.2 Heat Treatments and Microstructures*

Figure 3.2 shows the phase diagram of Fe-12Cr-0.15C-1.5W-0.3Ti system with changing Ni composition [20], with schematics of microstructure evolution during

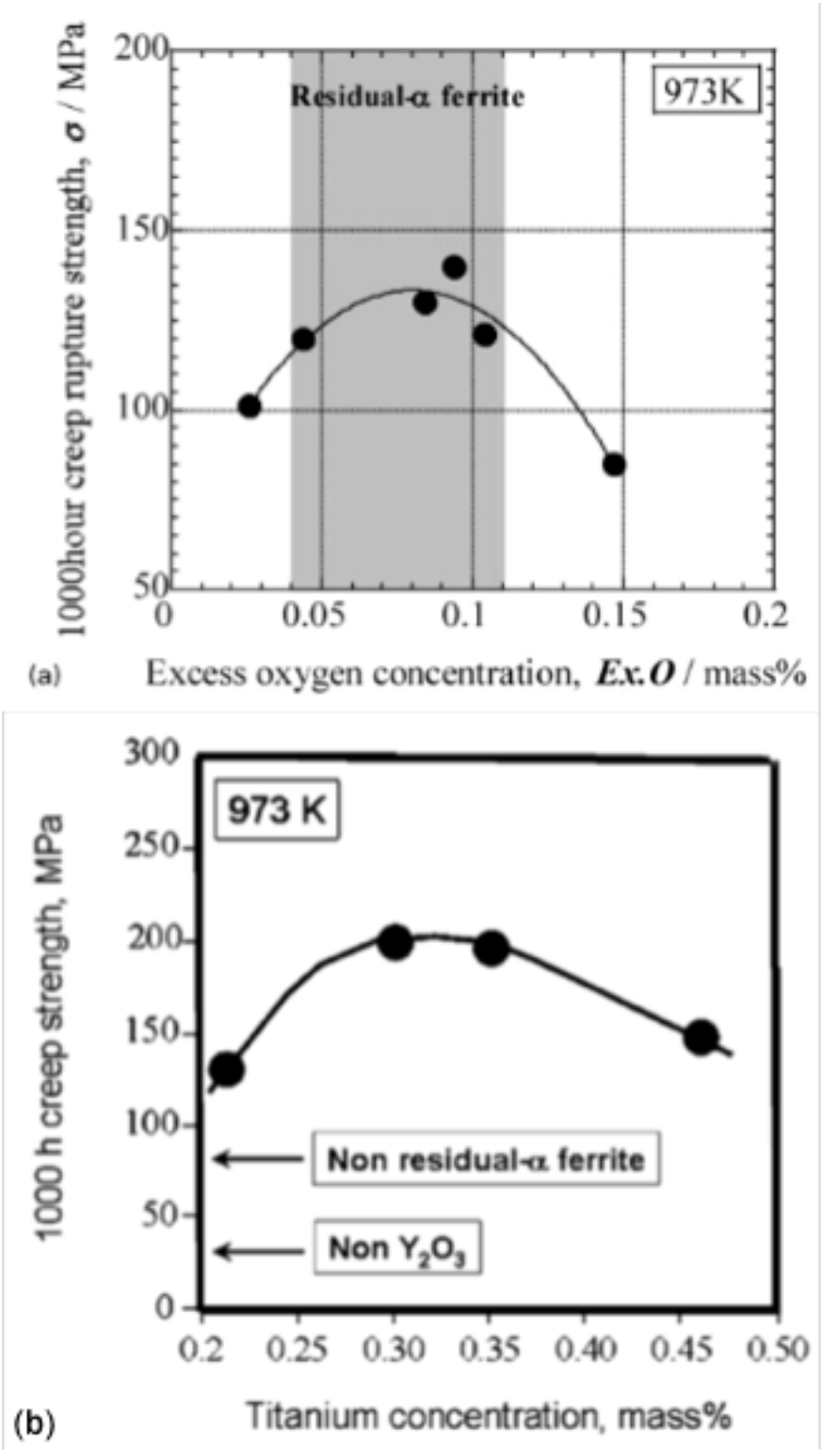


Figure 3.1: The rupture strength of the ODS material as function of (a) excess O and (b) Ti compositions [19]

material fabrication and heat treatment. Over lapped on the phase diagram, the red disk on the top represents material being normalized at 1050 °C; the blue disk at the bottom represents material air-cooled down to room temperature after normalization; the yellow disk in the middle represents material being tempered at 800 °C to achieve the tempered martensite microstructures. Starting with normalization, the material has dual phases of $\alpha$ and $\gamma$. The fraction of $\alpha$ will be higher than as predicted by the equilibrium phase diagram, due to the pinning effect of fine particles (shown as little blue spots) that prevent $\alpha - \gamma$ phase transformation at normalization condition [20]. After the material was cooled down in an atmosphere of air with a cooling rate of ∼3000 °C per hour, $\gamma$ phase transforms to martensite phase with lath structure. Due to phase transformation, the coherency between some of the nano-particles and the matrix is interfered, leading to higher interfacial energy. As a result, oxide particles coarsen to minimize the interfacial energy. Experimental evidence of this statement would be provided later. Tempering at 800 °C remove the high density of dislocations in martensite phase, reaches an equilibrium ferritic crystal structure in the tempered martensite phase with lath grain structures decorated with carbide. Both carbide and nano particles present in the tempered martensite grains will help to stabilize their sub-grain structures.

According to Ukai et al., a moderate amount of ferrite phase in the dual-phase alloy would maximize the creep rupture strength, through the so-called mesoscopic optimization [19]. Ferrite grains are harder with the finer and denser dispersoids, as a result, they prevent and/or delay the deformation occurs to the softer tempered martensite grains surrounded when the material is stressed. On the other hand, the harder ferrite grains are less likely to take intragrain deformation when the stress is beyond the threshold stress at which dislocations get over the oxide dispersoids. The

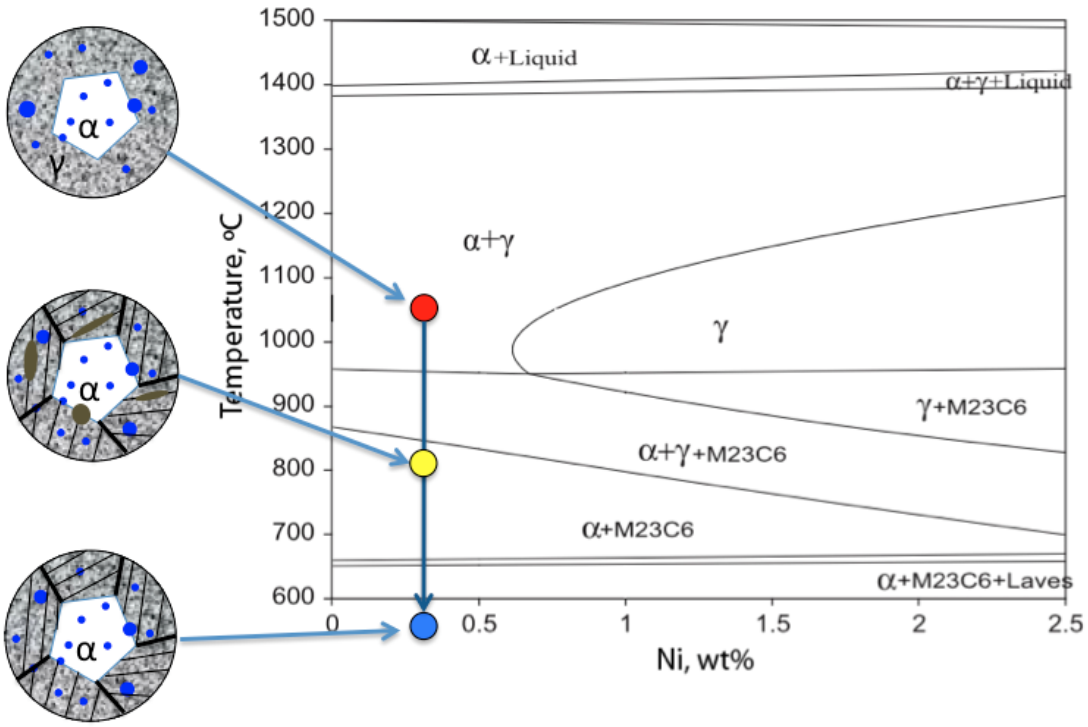


Figure 3.2: Phase diagram of Fe-12Cr-0.15C-1.5W-0.3Ti system with changing Ni composition [20], overlapped with schematics of grain structures at different conditions during heat treatment

interface between hard and soft grains is vulnerable to cracking, resulting from the stress concentration at grain boundary triple junctions [19].

## 3.2 Material Microstructure Characterizations

### *3.2.1 Grain Structure*

Figure 3.3 shows typical TEM micrographs of a ferrite grain (Figs. 3.3a-b) and a tempered martensite grain (Figs. 3.3c-d) observed in the as-received unirradiated sample. The ferrite grain fraction was measured to be $\sim$ 20%. As pointed out by Ukai et. al, the ferrite phase in this alloy consists of both residual ferrite and thermal equilibrium ferrite. While they arise from different mechanisms, these phases have essentially the same physical properties [20]. In addition, transformed ferrite can also exist when the phase transformation from austenite to ferrite takes place during air cooling [19]. Differences in grain size between ferrite and tempered martensite grains were obvious; ferrite grains were significantly larger (up to $\sim 1\mu$m) compared to tempered martensite grains ($\sim$200 nm).

### *3.2.2 Dispersoids*

Tempered martensite and ferrite grains were found to have different dispersoid distributions. As shown in Fig 3.3b, dispersoids in one ferrite grain are more uniform in size and more homogeneously distributed. In contrast, dispersoids in tempered martensite phase as shown in Fig 3.3d have large size variation even within one grain. The difference is statistically compared in Fig. 3.4, which was generated by measuring at least 100 randomly picked dispersoids from multiple grains in each of the ferrite and tempered martensite phases. The tempered martensite phase exhibits coarser dispersoids compared to the ferrite phase. In ferrite, while most dispersoids have diameter less than 5 nm, larger dispersoids were found in the transformed ferrite.

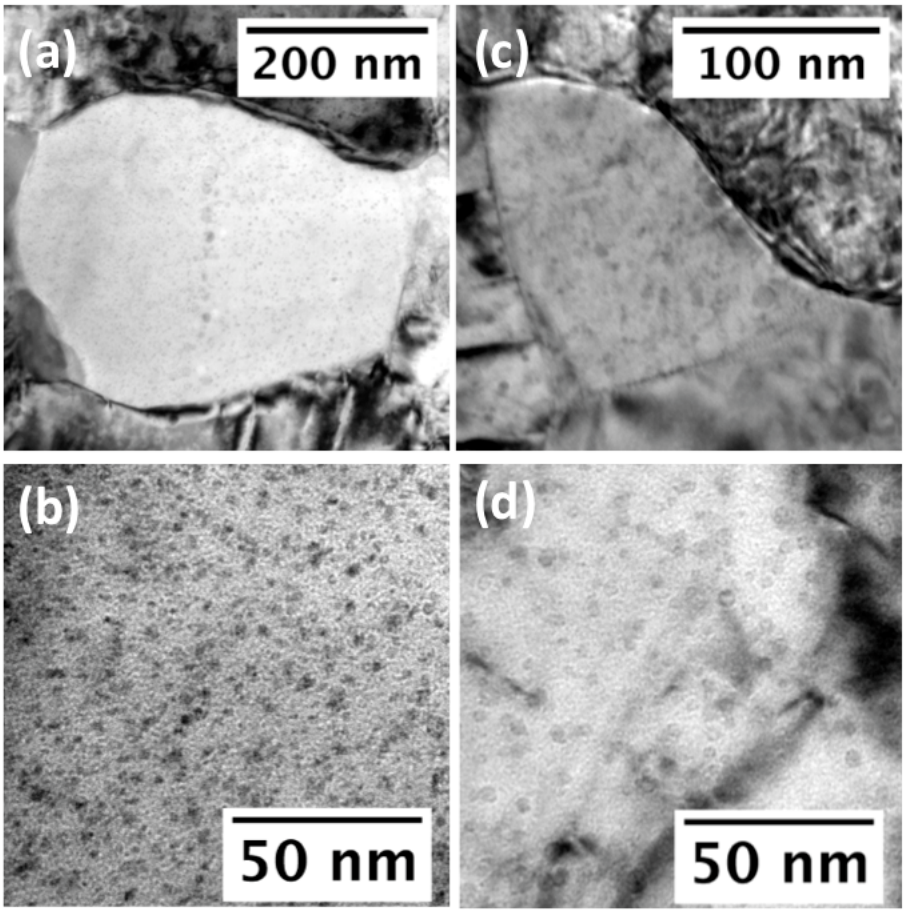


Figure 3.3: TEM micrographs of unirradiated samples having dispersoids in (a-b) a typical ferrite grain and (c-d) a typical tempered martensite grain [21]

Similar coarse distributions of dispersoids in tempered martensite and transformed ferrite phases were also observed in 9Cr and other 12Cr ODS [51, 20, 58]. It has been suggested that the disturbance of interfacial coherency between dispersoid and matrix, during phase transformation, results in the coarsening of dispersoids via interfacial energy minimization [19, 57, 59]. Therefore fine dispersoids were more likely to exhibit coherency with the matrix than larger dispersoids. In both phases, the dispersoid density varies significantly from grain to grain. The average dispersoid density in tempered martensite and ferrite phases were measured to be $\sim 7.6 \times 10^{16}$ $cm^{-3}$ and $\sim 1.6 \times 10^{17}$ $cm^{-3}$, respectively.

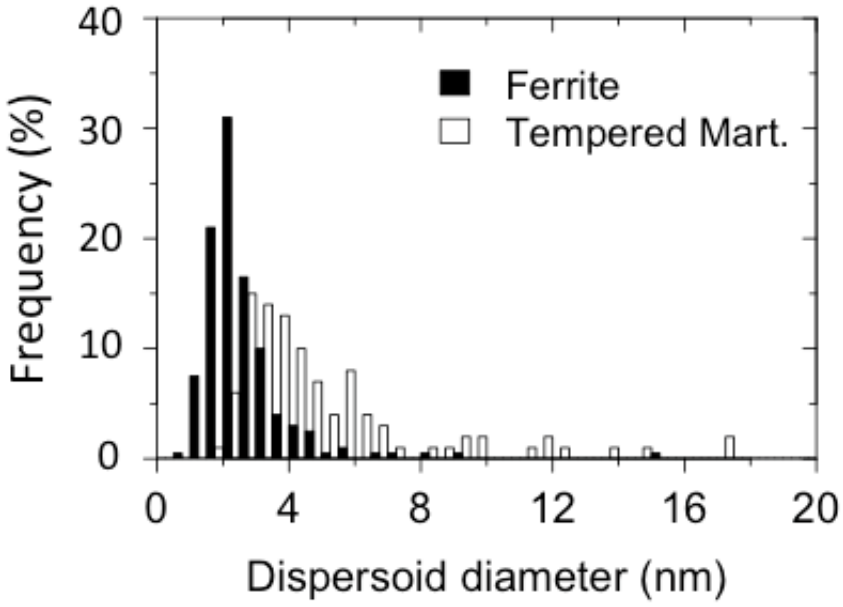


Figure 3.4: Size distribution of dispersoids in ferrite and tempered martensite grains in the before irradiation [21]

The chemical composition of nano dispersoids were confirmed using EELS, STEM

and EDS. Figure 3.5 exhibits the zero-loss image, the yttrium (Y) mapping and the Ti mapping of a same grain containing nano dispersoids. Clearly, the nano particles are Y and Ti rich, suggesting that they are Y-Ti-O particles. Figure 3.6a is a STEM micrograph obtained from another grain, showing dispersoids because of the Z-contrast of STEM technology. A typical EDS spectrum of a particle was recorded and shown in Figure 3.6b. While the Fe and Cr signals came from the matrix, the Y and Ti peaks shows the chemical composition of the particle. EDS analysis of dispersoids of sizes ranging from ∼3 nm to ∼30 nm in diameter showed a Y/Ti ratio of between ∼1:1 and ∼2:1.

Figure. 3.7 shows bright field and weak beam dark field TEM micrographs of a tempered martensite grain. Dislocations and dispersoids have a non-uniform distribution and wide range in size. The dark field micrograph suggests that a coherent or semi-coherent relationship exists between most of the fine dispersoids and the matrix, as illustrated by the dashed arrow, while coarse dispersoids do not exhibit coherency, as illustrated by the solid arrow. This conclusion was later confirmed using HRTEM.

The size distribution of total dispersoids and coherent dispersoids can be obtained from bright field images like Fig 3.7a and dark field images like Fig 3.7b, respectively. The distribution of total dispersoid and coherent dispersoid, both normalized over its own population, of tempered martensite grains, is exhibited in Fig 3.8. It is clear shown that within finer particle range, i.e., below ∼3 nm, most dispersoids are coherent, whereas larger dispersoids tend to be semi-coherent or incoherent with the matrix. On the other hand, the coherent dispersoid distribution of radiation-free sample in tempered martensite, shown as white bars in Fig. 3.8, is similar to the dispersoid distribution in radiation-free ferrite phase as shown as white bars in Fig. 3.4.

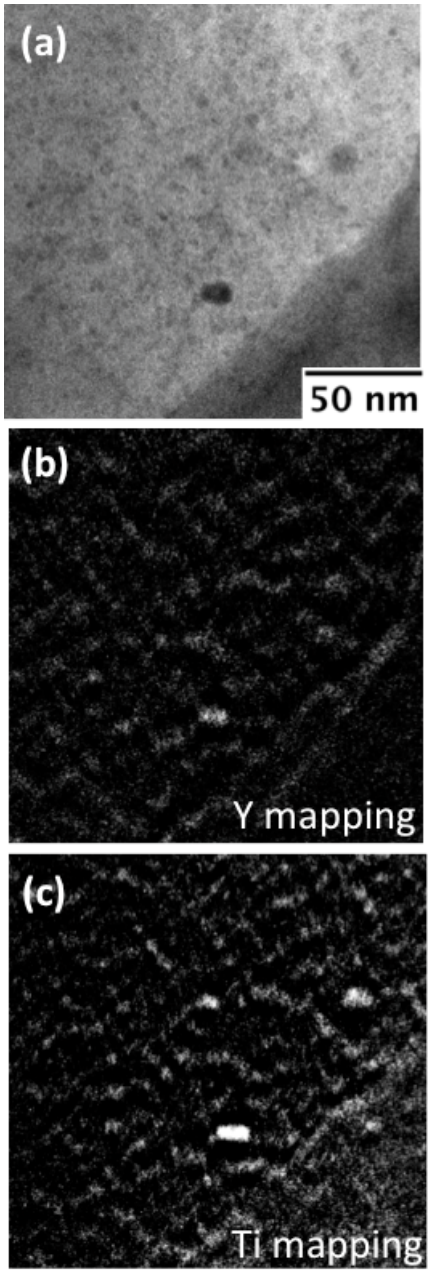


Figure 3.5: (a) Zero-loss micrograph, (b) Y element mapping and (c) Ti element mapping of a same grain containing nano dispersoids

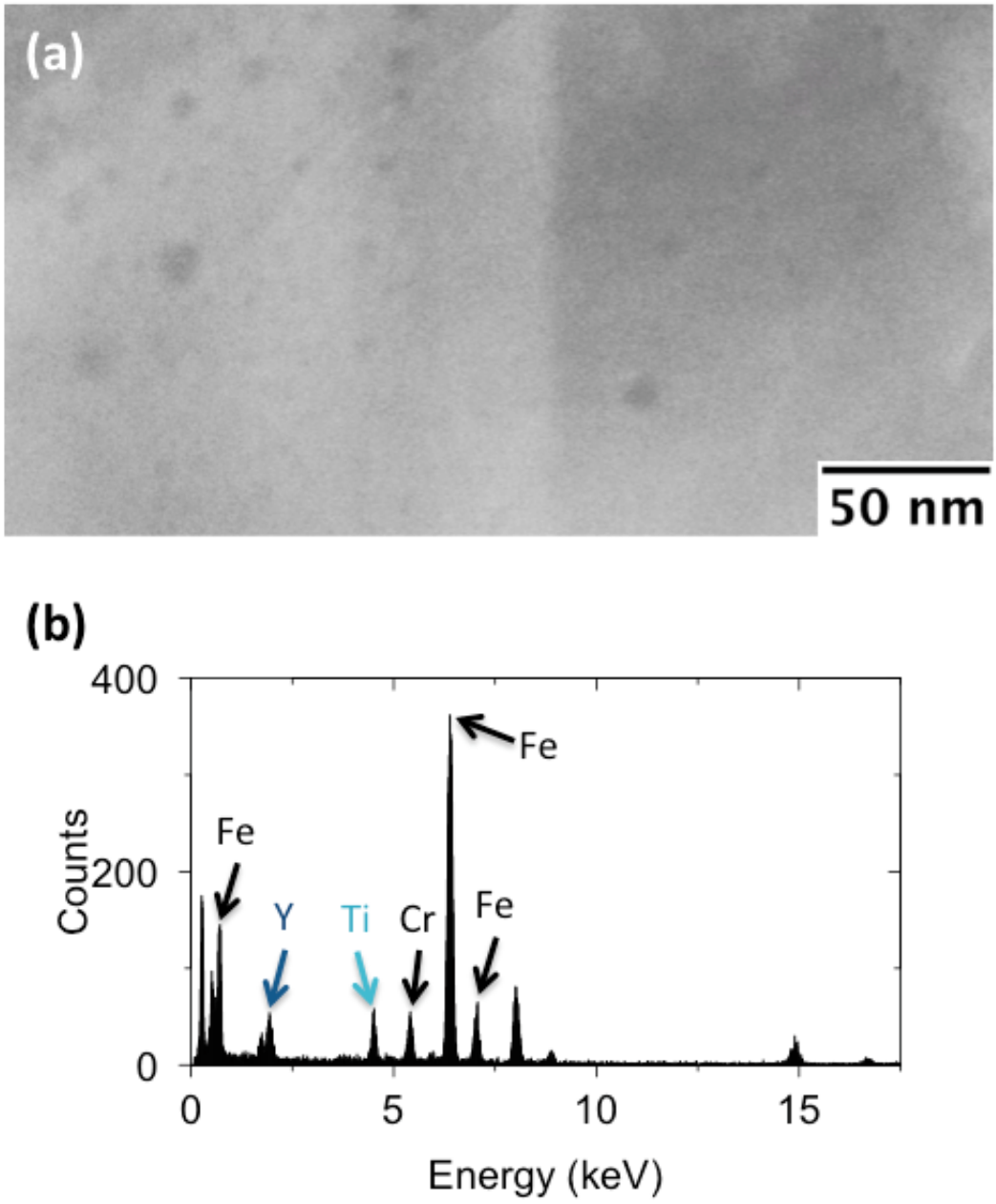


Figure 3.6: (a) STEM image of nano dispersoids, and (b) EDS spectrum obtained from a nanoparticle

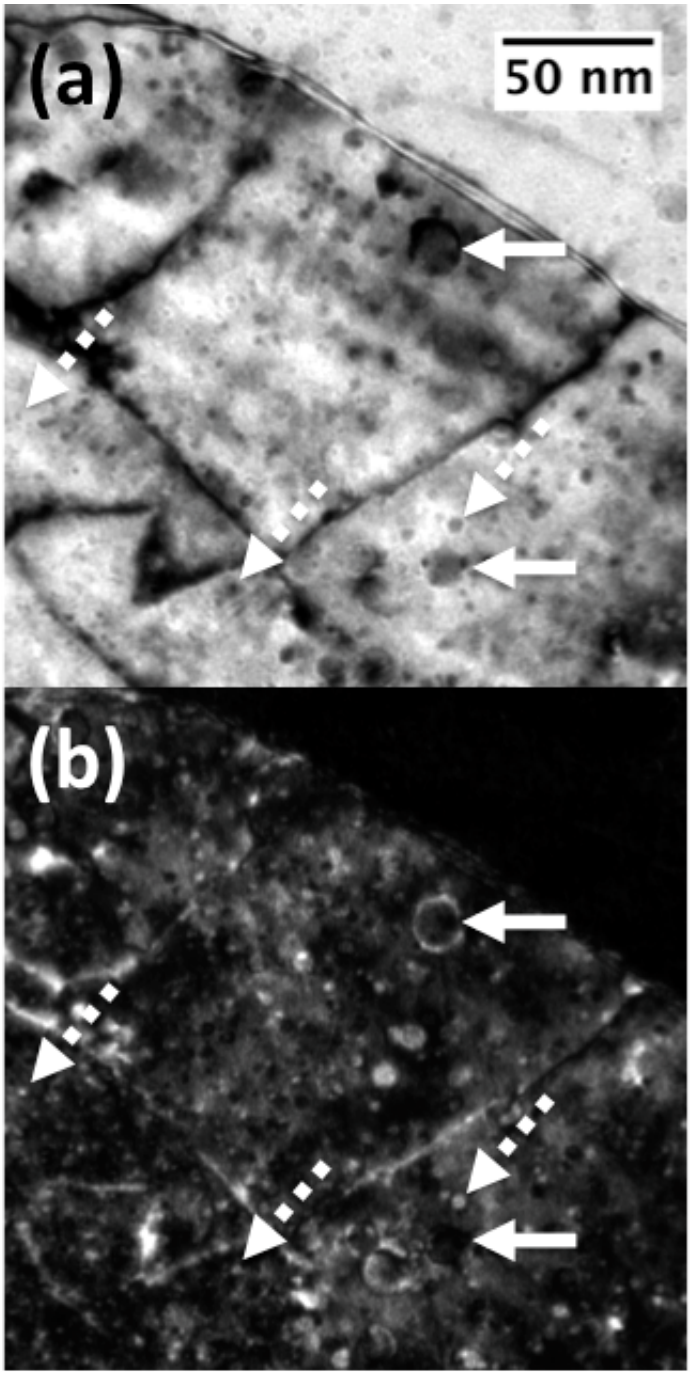


Figure 3.7: (a) Bright field TEM image and (b) weak beam dark field TEM image of an unirradiated tempered martensitic grain obtained near $\mathbf{g}_{110}$. The dashed arrow highlights a coherent dispersoid, while the solid arrow highlights an incoherent dispersoid [21]

This suggests that during material fabrication and before $\alpha/\gamma$ transformation [20], dispersoids might have a homogenous distribution with most of them being small and coherent. Dispersoids which lost their coherency due to the phase transformation coarsened through Ostwald ripening [19, 57, 59], a kinetic progress also believed to occur during high-temperature annealing or irradiation [50]. As a result, the distribution of total dispersoids in tempered martensite phase is broadened by including coarse incoherent dispersoids.

Figure 3.9 shows diffraction patterns and HRTEM micrographs of a ∼3 nm dis-

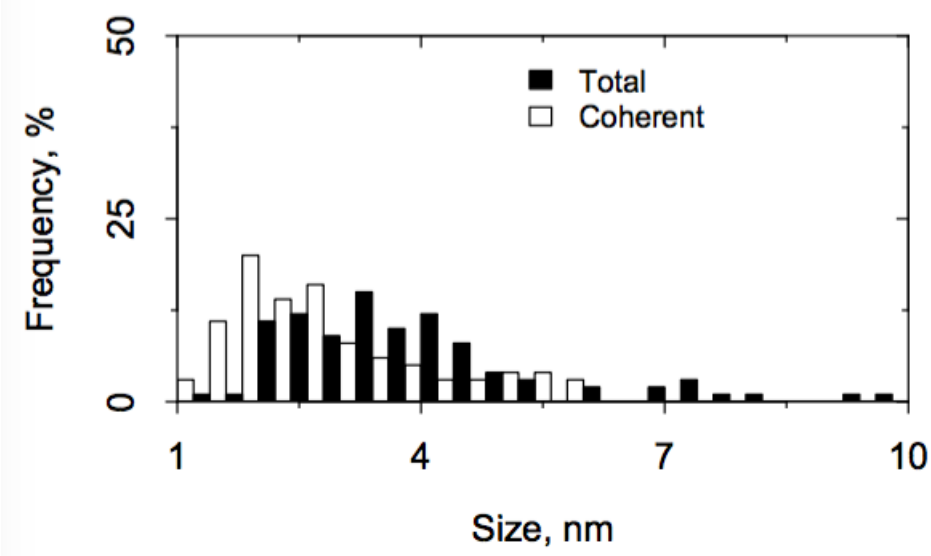


Figure 3.8: The size distribution of total dispersoid and coherent dispersoid of tempered martensite grains [21]

persoid in a ferrite grain imaged at the $[012]_\alpha$ zone axis. The diffraction pattern in Fig. 3.9a shows coherency between dispersoids and the matrix, which are confirmed by HRTEM images in Figs. 3.9b-d. As marked by dashed lines in Fig. 3.9b, the nano-particle exhibited two planar directions clearly visible. The two plane-to-plane

distances were measured to be 0.24 nm, and the angle between them was measured be to 61°. These agree with the 0.23 nm interplanar distance and 61.73° inter-direction angle of (331) and (31$\bar{3}$) planes of $Y_2Ti_2O_7$, suggesting a coherency of $(32\bar{1})_d \parallel (001)_\alpha$ and $[5\bar{6}3]_d \parallel [012]_\alpha$ between fine dispersoids and the ferrite matrix.

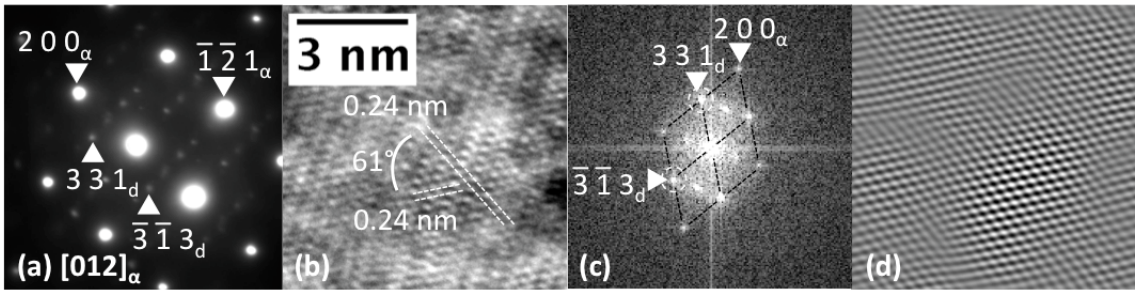


Figure 3.9: (a) Diffraction pattern of an unirradiated ferrite grain, (b) HRTEM micrograph of a dispersoid in this grain, (c) FFT diagram of the micrograph in (b), (d) FFT filtered image derived from diffraction spots circled in (c) [21]

Figure. 3.10 shows diffraction patterns and HRTEM taken at $[011]_\alpha$ zone axes of a tempered martensite grain. Weak diffraction spots shown in Fig. 3.10a indicate that lattice coherency between fine dispersoids and the matrix exists, similar to fine dispersoids in ferrite phase. Figures. 3.10b-d correspond to a dispersoid with a diameter of ∼6 nm. As shown in Figs. 3.10b-c, the coherency between the dispersoid and matrix is different from that of finer dispersoids. Two interplanar spacings were measured to be 0.28 nm and 0.27 nm with an angle of 86° between them, matching the (330) and (2$\bar{2}$1) planes of orthorhombic $Y_2TiO_5$. Therefore interface coherency of $(15\bar{1})_d \parallel (0\bar{1}1)_\alpha$ and $[1\bar{1}\bar{4}]_d \parallel [011]_\alpha$ is suggested. For dispersoids larger than 10 nm in diameter, no coherency was observed.

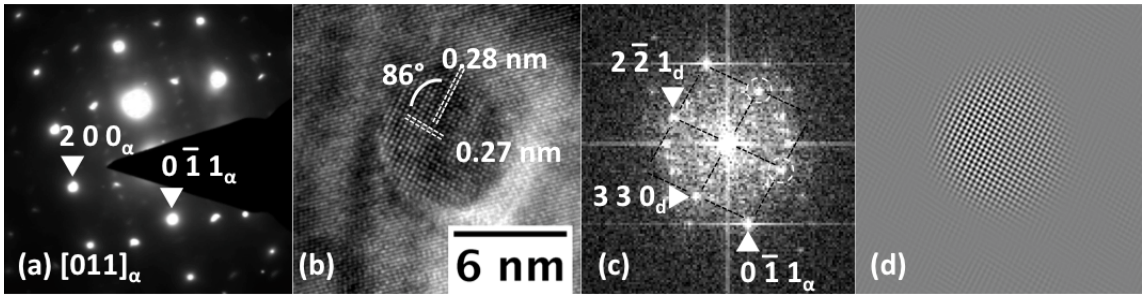


Figure 3.10: (a) Diffraction pattern of an unirradiated tempered martensite grain, (b) HRTEM micrograph of an dispersoid in this grain, (c) FFT diagram of the micrograph in (b), (d) FFT filtered image derived from diffraction spots circled in (c) [21]

## 3.3 Conclusions

In this section, we showed a dual-phase ODS material that has been optimized in nano level and mesoscopic level to enhance its creep strength. The enhancement in mechanical properties is through mesoscopic microstructure controlling of ferrite/tempered martensite grain ratio, and nano-structure controlling of dispersoid size, distribution and coherency. By means of TEM microstructure analysis, we confirmed the existence of both phases with a ferrite/tempered martensite ratio of $\sim$1:4. Fine and dense particles were found in ferrite, while particles in tempered martensite has a broader distribution. Smaller particles in tempered martensite grains were found to be coherent to the matrix; and larger ones are observed to be incoherent. The incoherency of coarsened particles is believed to be a result of coherency-loss due to $\alpha/\gamma$ phase transformation during heat treatment.

# 4. RADIATION RESPONSE OF THE 12CR ODS: DOSE DEPENDENT*

In last section we introduced the novel 12Cr dual-phase ODS, which was designed to have enhanced corrosion resistance, high-temperature oxidation resistance and high-temperature strength. It was believed that the high-temperature strength was achieved by a combination efforts of grain structure and nano-particles. In this section, we reported experiment results of self-ion irradiations at 475 °C to peak damage up to 800 dpa. Focus would be put on grain and sub-grain structure stability under irradiation, as well as evolution of dispersoids during irradiation. Because the stability of grain structure and dispersoid will provide enhancement to material properties under irradiation conditions. On the other hand, it is well known that tempered martensite microstructure has a high swelling resistance due to its high density of boundaries serving as defect sinks. And nano-sized dispersoids can also provide defect trapping sites from their interface with the matrix. Thus, we expect swelling resistance enhancement contributed from both tempered martensite structure and nano dispersoids.

## 4.1 High Dpa Irradiation

Specimens were cut to dimensions of 5 mm × 5 mm × 0.7 mm and then mechanically polished with SiC paper, progressing down to a grit of 1200, followed by 0.05 $\mu$m aluminum powder. The surface layer containing residual mechanical damage was then removed using electrical polishing with a perchloric solution. Irradiation with

*Part of the data reported in this section is reprinted with permission from "Microstructural changes and void swelling of a 12Cr ODS ferritic-martensitic alloy after high-dpa self-ion irradiation" by T. Chen, E. Aydogan, J.G. Gigax, D. Chen, J. Wang, X. Wang, S. Ukai, F.A. Garner, L. Shao, 2015, Journal of Nuclear Materials, 467, 42-49, Copyright [2015] by Elsevier B.V.

3.5 MeV $Fe^{2+}$ ions was performed using a 1.7 MeV Tandetron accelerator. A defocused beam was used to avoid void-swelling-suppression characteristic of rastered beams [6, 60, 28]. The beam current was controlled at 200 ± 10 nA, producing a maximum dpa rate of $\sim 1.74 \times 10^{-3}$ dpa per second at damage peak. The depth profiles of dpa and injected Fe atoms, calculated by the SRIM code [61], are shown in Fig. 4.1. A value of 40 eV displacement threshold energy and the Kinchin-Pease option were used for the damage calculations [62, 63]. The irradiation temperature was controlled to be 475 ± 10 °C to maximize swelling based on previous determinations of peak swelling temperatures [54, 55, 56, 5]. The chamber vacuum during irradiation was better than $1 \times 10^{-6}$ torr.

Six specimens received 100, 200, 300, 400, 700 and 800 dpa at the peak displacement depth. Cross-sectional lamella samples from unirradiated and irradiated specimens were prepared using FIB lift-out technique with a TESCAN LYRA-3 FIB-SEM forTEM investigations. TEM characterizations were performed using a 200 keV FEI Technai F20 Supertwin microscope.

## 4.2 Post-irradiation Characterizations

### *4.2.1 Grain Structure*

Figures 4.2a-e show bright field cross-sectional TEM micrographs of the unirradiated sample and samples irradiated to 100, 200, 400 and 800 peak dpa, respectively. The dashed lines in Fig. 4.2 refer to the ∼1 $\mu$m region that was irradiated. Deeper regions represent structures that were thermally annealed but not irradiated. Note that the sample receiving 800 peak dpa was annealed at 475 °C for as long as ∼125 hours. No changes of grain size were noticed for both ferrite and tempered martensite phases in either the irradiated or thermally aged regions. Statistics of grain

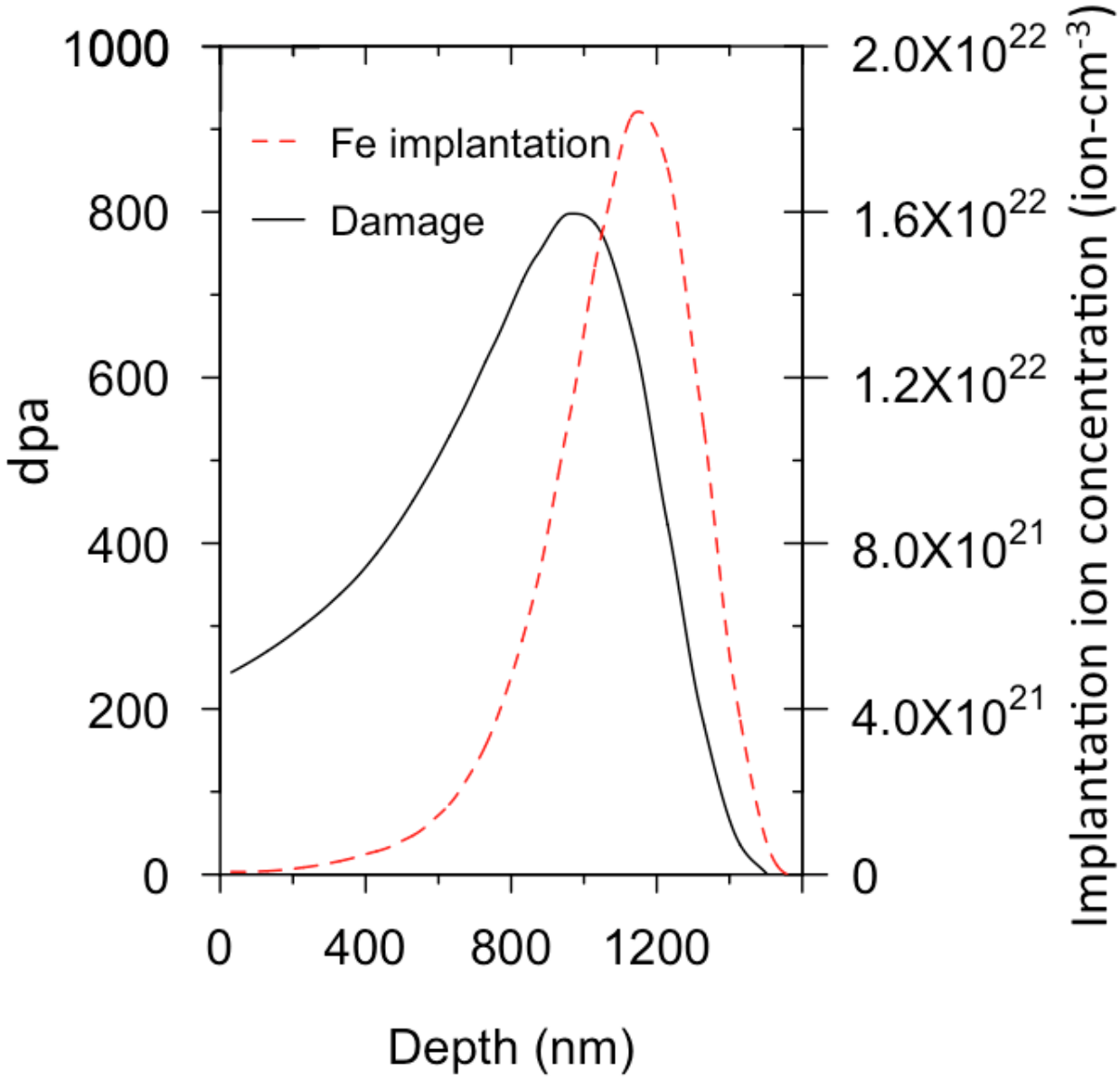


Figure 4.1: SRIM calculation of 3.5 MeV self-ion irradiation into pure Fe to 800 dpa maximum, using a displacement threshold energy of 40 eV and the Kinchin-Pease option [21]

size are listed in Table 4.1. Compared to unirradiated samples, all grain sizes were maintained within the statistical standard deviance.

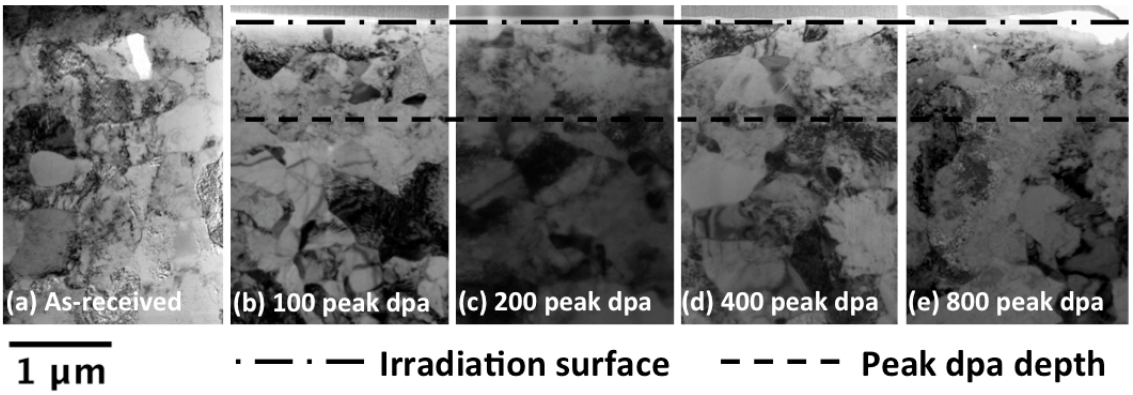


Figure 4.2: Bright field cross-sectional TEM micrographs of (a) unirradiated sample and (b-e) samples irradiated to 100, 200, 400 and 800 peak dpa, respectively. The dashed lines refer to the irradiated region [21].

Table 4.1: Mean grain size measured in as-received, irradiated and thermal-aged irradiation-free conditions [21]

| As-received sample | 274 ± 65 | | | Unit: nm |
|---|---|---|---|---|
| Location in sample | 100 peak dpa | 200 peak dpa | 400 peak dpa | 800 peak dpa |
| Peak dpa region | 281 ± 61 | 271 ± 51 | 309 ± 40 | 268 ± 44 |
| Irradiation free region | 272 ± 46 | 293 ± 62 | 282 ± 46 | 241 ± 53 |

### *4.2.2 Dispersoid Shrinkage and Stability*

Figures 4.3a-d were obtained from the 400 peak dpa sample, presented as a panoramic TEM micrograph showing dispersoids starting from the irradiated surface to a depth beyond the peak damage (the dpa peak is located at $\sim$ 1000 nm).

Only grains of the tempered martensite phase are shown in Fig. 4.3d. Both depth (bottom) and the corresponding local dpa values (top) are provided. The enlarged TEM images of three local regions correspond to the near-surface region, the half peak-dpa region and the end of damage region, respectively. In comparison with the bulk unirradiated region, overall, dispersoid sizes within the irradiated region are reduced. Similar observations have been reported in previous studies on $Ni^{2+}$ ion irradiated 9Cr ODS and 14YWT, whereas rastered beams were used [51, 36]. In addition, as shown in Figs. 4.3b-c, the highly irradiated region (in Fig. 4.3b) shows higher dispersoid density compared to regions receiving lower dpa (in Fig. 4.3c). Compared to unirradiated samples, the dispersoid density in tempered martensite was observed to increase due to irradiation by a factor of $\sim$1.5.

The mean dispersoid sizes in samples after 100, 200, 400 and 800 peak dpa irradiation are plotted as a function of depth from irradiated surface in Fig. 4.4. The solid lines denote the size range of dispersoid distribution in unirradiated tempered martensite grains, and the dash lines denote the range of dispersoid sizes in unirradiated ferrite grains. One important finding is that dispersoid sizes were reduced after irradiation and approached to $\sim$2-2.5 nm in irradiated region ( $\leq$1000 nm), regardless of different dpa rates at different depths.

Figure 4.5a shows two neighboring ferrite and tempered martensite grains at $\sim$750 dpa region in the 800 peak dpa irradiated sample. Figures 4.5b-c are higher-magnification TEM micrographs showing dispersoids in the ferrite and tempered martensite grains, respectively. Figure. 4.5d summarize size distributions of dispersoid in two phases after irradiation. Dispersoids in tempered martensite grains underwent a dramatic shrinkage. In both phases, most, if not all, dispersoids larger

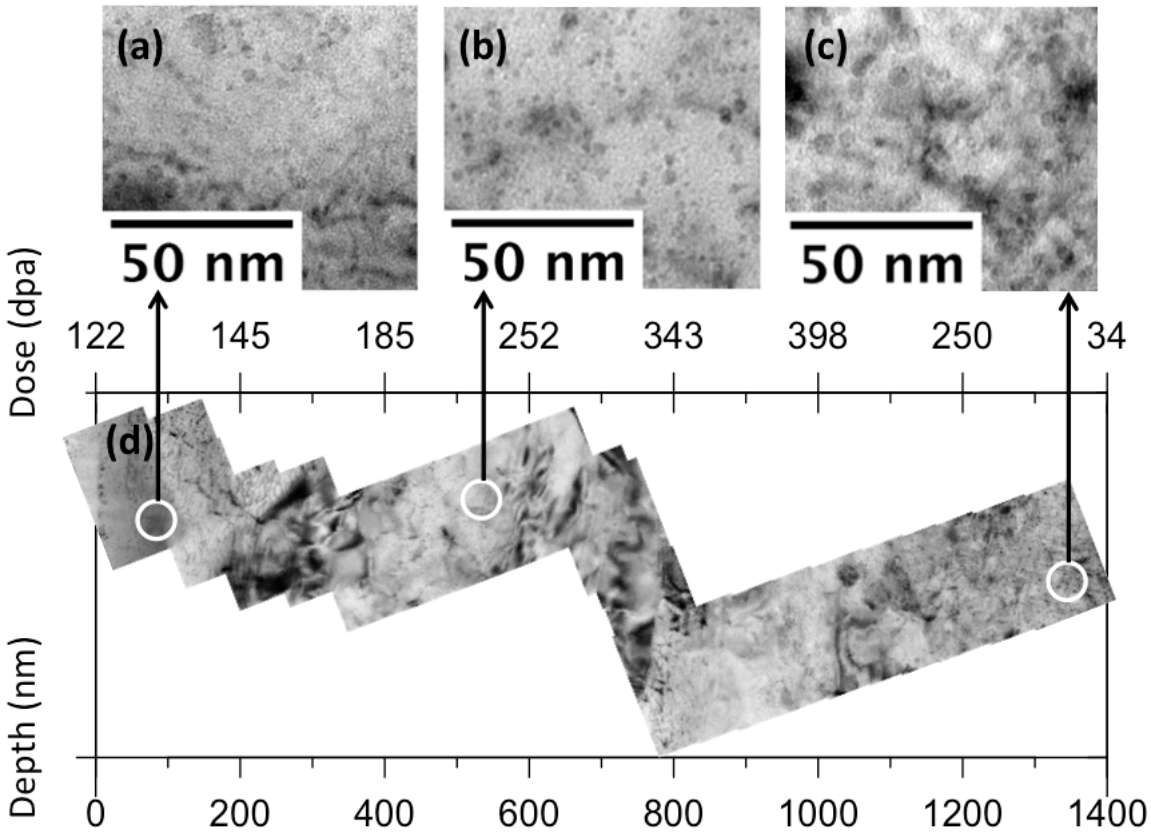


Figure 4.3: (a-c) TEM micrographics at near surface region, half-peak-dpa region and end of irradiation region, respectively, and (d) panoramic TEM micrographs from the 400 peak dpa sample [21]

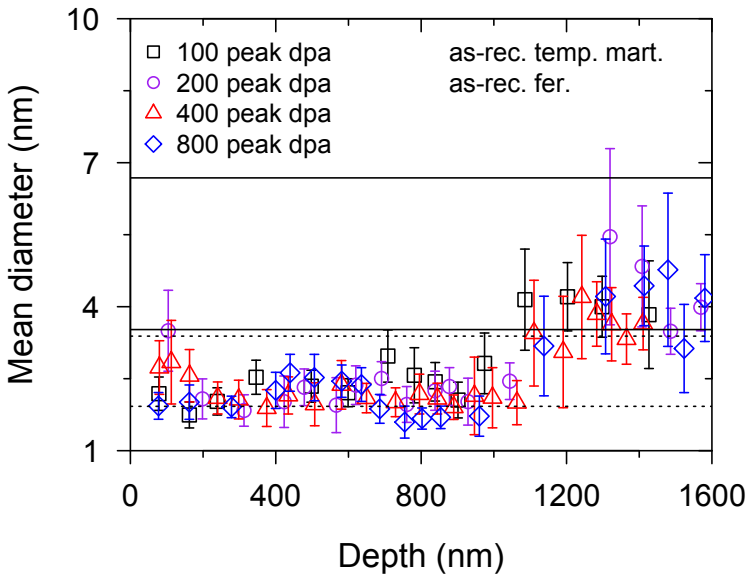


Figure 4.4: Mean dispersoid diameter vs. depth from samples irradiated up to peak dpa values of 100, 200, 400 and 800, with solid horizontal lines representing the range of the as-received dispersoid distribution in tempered martensite grains, and the dashed horizontal lines representing the range of the as-received dispersoid distribution in ferrite grains [21]

than 5 nm were removed by irradiation. In the ferrite phase, while there was a barely noticeable size change in the fine dispersoids, the dispersoid density dropped ∼20%. Decrease in density and sustainment in size of the fine dispersoids in ferrite phase agrees with observations in neutron irradiated MA957 [43, 33], while loss of larger dispersoids in the tempered martensite phase agrees with previous studies by Allen, et al. on Ni irradiated 9Cr ODS [51]. It is important that in the present study, dispersoids of different sizes were confirmed to have different stability in the same dual-phase alloy.

Beyond 1200 nm, where the dpa level rapidly drops to zero, a plateau of dispersoid diameter appears at ∼4-5 nm, a range close to the mean dispersoid diameter in the pre-irradiation condition. The dispersoid size distribution in the radiation-free zone is the same as it is in pre-irradiation condition, suggesting that observed size difference in the irradiated region results from irradiation effects, instead of thermal annealing effects

To further illustrate the evolution of dispersoid populations with increasing damage level, an analysis of dispersoid size was carried out, limited to the 400 nm to 700 nm depth range, to minimize compositional changes resulting from the injected Fe atoms. The selected region corresponds to a damage level of $\sim 60\%$ of the peak dpa. Only tempered martensite data were used for this comparison. Figure. 4.6 shows that dispersoid shrinkage after ion irradiation essentially stops by 60 dpa; with a stable size distribution maintained thereafter. As pointed out in earlier studies, such stability of fine dispersoids can sustains ODS strength during irradiation [51, 64, 65].

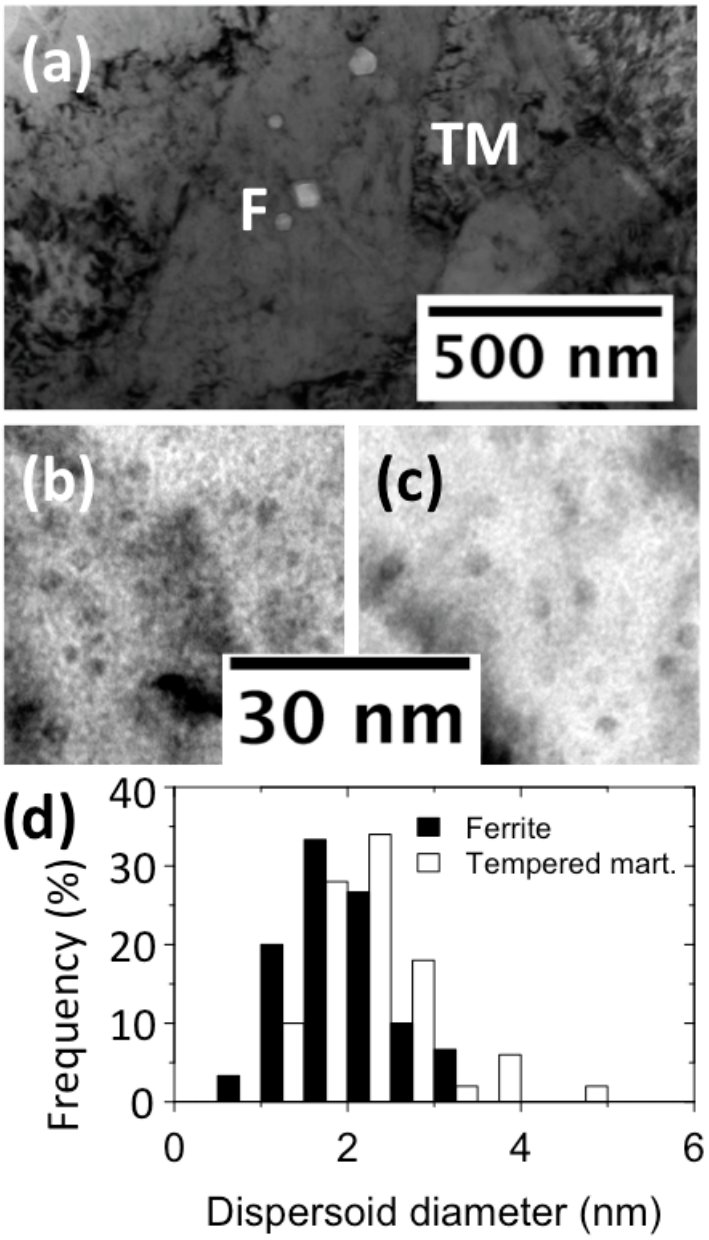


Figure 4.5: (a) TEM micrograph taken from the 500-1200 nm region of the 800 peak dpa sample, with F and TM referring to ferrite and tempered martensite phase, respectively, and (b), dispersoids in the ferrite grain F, and (c), dispersoids in the tempered martensite grain TM, and (d), statistic size distributions of dispersoids in irradiated ferrite and tempered martensite phases [21]

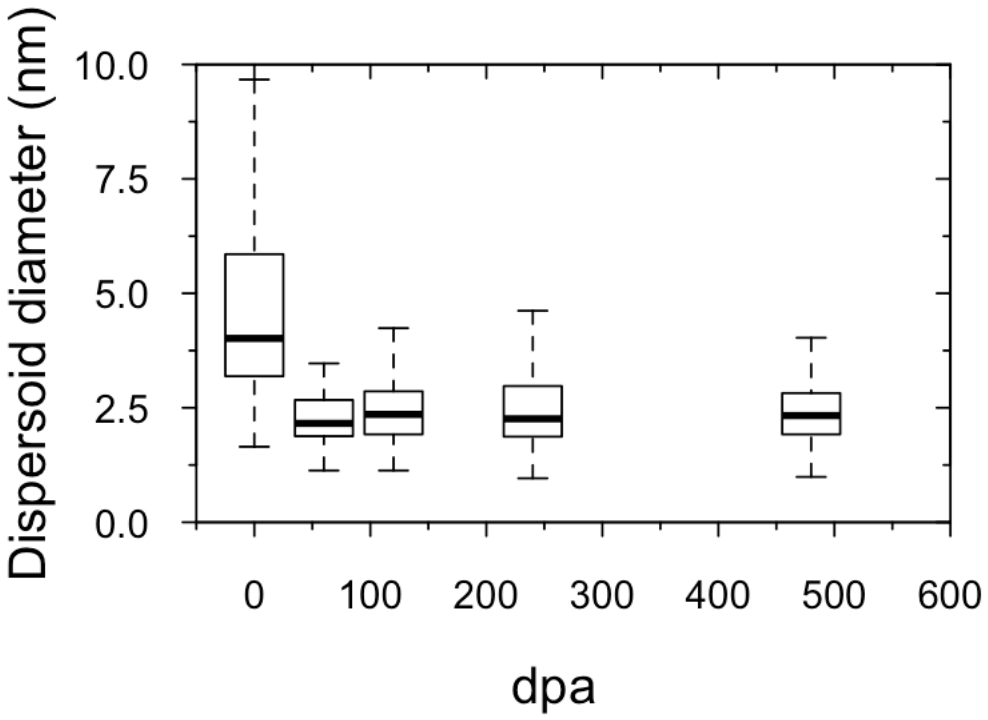


Figure 4.6: Dispersoid size as a function of increasing dpa in tempered martensite grains, with the bottom and top of the rectangular boxes represents the first and third quartiles of the statistic data, respectively, while the bar in the middle of the box represents the mean value [21]

### *4.2.3 Void Swelling*

Previous studies have shown that in the absence of dispersoids, the ferrite phase is significantly less swelling resistant than the tempered martensite phase, as tested using neutron irradiation and heavy-ion irradiation [66, 67]. The tempered martensite phase is usually smaller in grain size compared with ferrite, and has more dense and complex internal microstructure to serve as sinks for point defects created by radiation, thereby imparting additional resistance to void nucleation. Therefore, it has been suggested that employing dispersoids in the tempered martensite phase may gain additional swelling-suppression, first by pinning the grain walls to maintain small grain size and second by allowing the dispersoids to serve as sinks. To date, however, very limited results have been reported on ODS tempered martensite phase [68, 51, 69, 44, 47].

As shown in Fig. 4.5a, the ferrite and tempered martensite phases exhibit different swelling behavior under irradiation. In the depth of 550-800 nm, faceted voids up to 45 nm in diameter formed in the larger central ferritic grain; while no voids were observed in the surrounding tempered martensite grains. Figures 4.7a-c show void formation in ferrite phase and Figs. 4.7d-f show void formation in tempered martensite phases as a function of dose. Micrographs were taken with an under-focus of $\sim$500 nm to image very small voids. Faceted voids were observed in ferrite phase at doses as low as 50 dpa. The void size increases with increasing dpa values. In comparison, only nano-cavities were observed in tempered martensite phase. Since void numbers in ferrite phase are quite limited, we focused on statistic analysis of voids in martensite phase only. Figures. 4.7g-i plot the void size distributions at 50, 200, and 400 local dpa regions, respectively. With increasing dpa values, void sizes

gradually increase but are still limited to only a few nanometers only. At 400 dpa, for instance, the mean size is ∼1.4 nm.

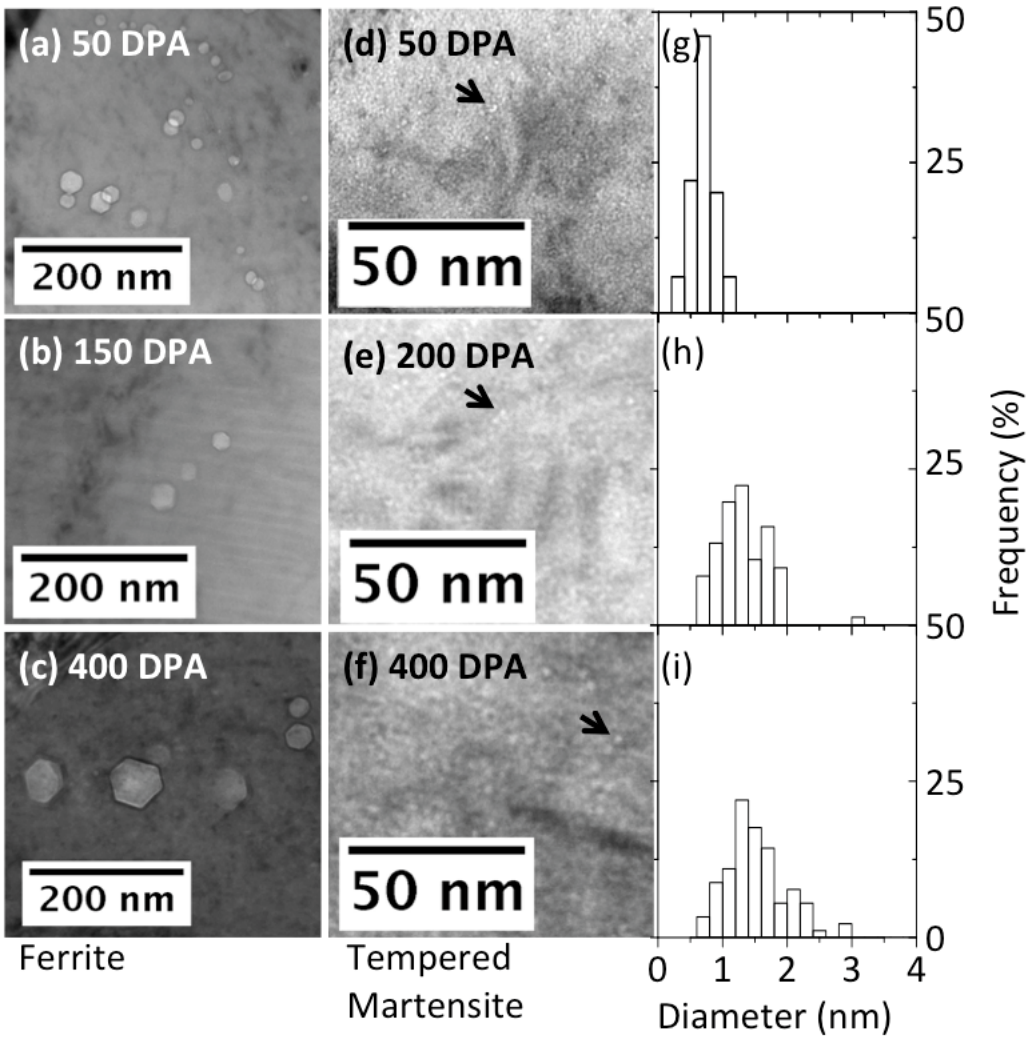


Figure 4.7: (a)-(c) TEM micrographs obtained at the depth of 500 nm in ferrite phases after 100, 300, 800 peak dpa irradiation, respectively, and (d-f) TEM micrographs obtained at the depth of 500 nm in tempered martensite phase after 100, 400, 800 peak dpa irradiation, respectively, with arrows highlighting some of the nano-cavities, and (g, h, i) the size distributions of nano-cavity in tempered martensite phases after irradiation corresponding to (d, e, f) [21]

Figures. 4.8a and b compare the depth-dependent swelling in ferrite and tempered martensite phases, respectively. The "spikiness" of the swelling distribution results from low statistics when void numbers are limited. Overall, the swelling in ferrite is more than one order of magnitude higher than that in tempered martensite. Note, however, that while the peak dpa occurs at a depth of ∼1000 nm from the surface, the swelling at higher dpa levels disappears at ∼800 nm, which is a well-known behavior attributed to combined effects from defect imbalance and the injected interstitial [53, 13]. This behavior has been frequently observed in self-ion irradiated pure iron and other F/M steels [28, 53, 13].

## 4.3 Discussion

### *4.3.1 Swelling Resistance and Strength*

The 12Cr dual-phase ODS alloy appears to have a very good swelling resistance under the high-dpa ion irradiation conditions employed in this study. Figure 4.9 plots the largest swelling values observed in the ferrite phase, as a function of local dpa where the data were extracted. These data are compared with published data from MA957, an ODS ferrite alloy [22], but this is not a single variable comparison due to differences in irradiating ion, energy and dpa rate. Nevertheless, this figure shows the rather low swelling obtained in the alloy of this study. Even more importantly, the majority of tempered martensite phase in this alloy is swelling almost negligibly, producing a very low overall swelling.

The swelling rate of ferrite phase in this ODS at the highest dpa examined was estimated to be ∼0.005 %/dpa, significantly lower than the steady-state swelling rate of ∼0.2 %/dpa from neutron irradiation of Fe-Cr alloys reported by Garner et

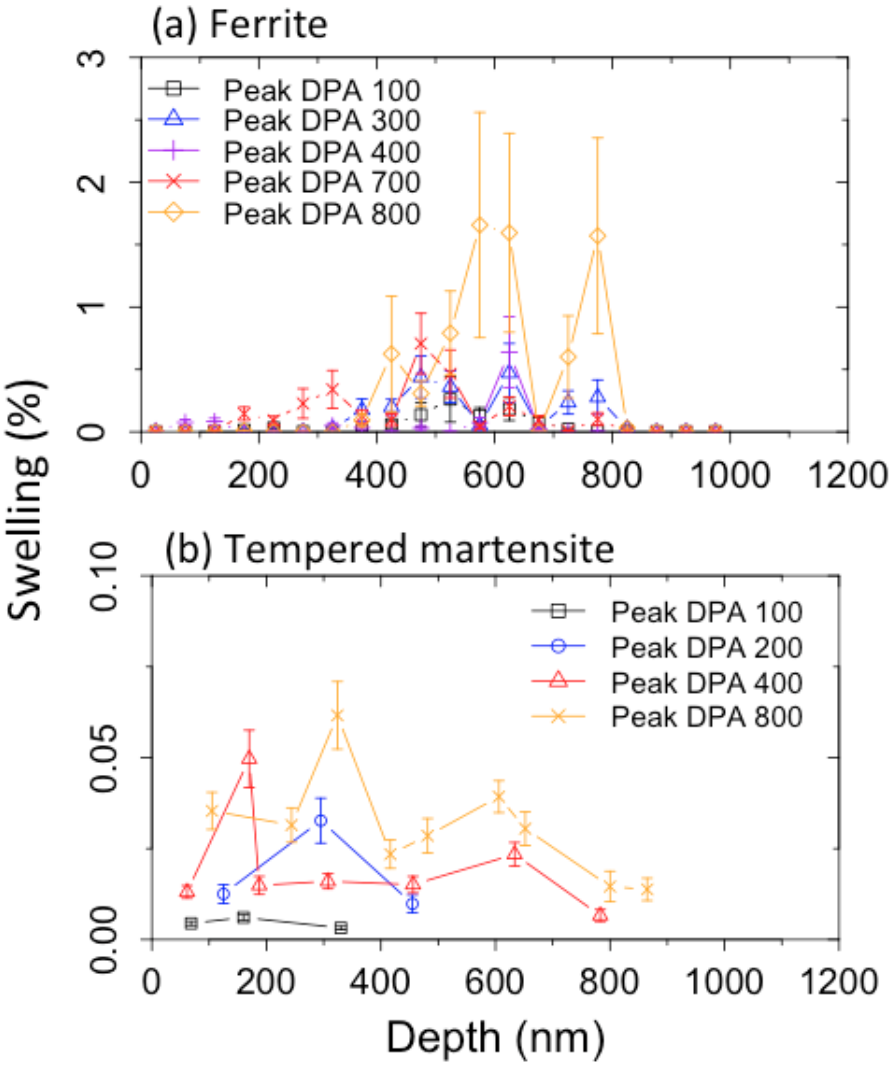


Figure 4.8: Swelling vs. depth distributions in (a) ferrite and (b) tempered martensite at different peak dpa levels [21]

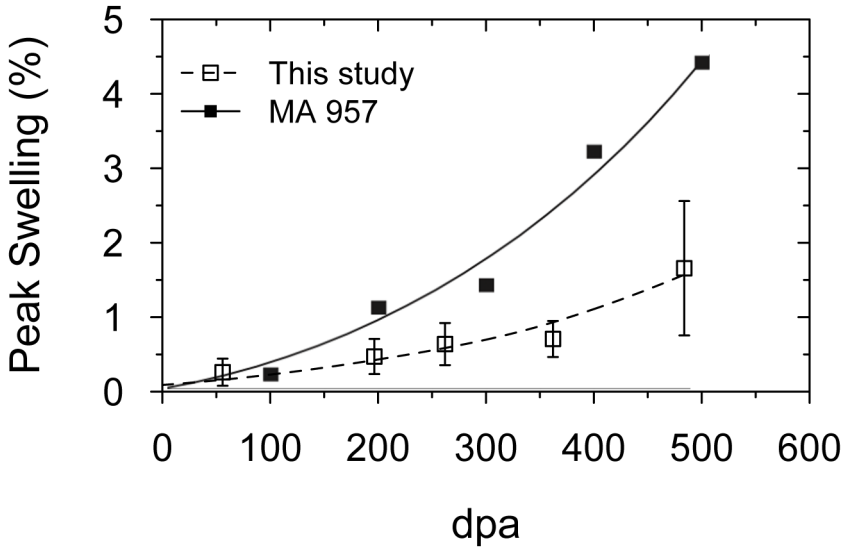


Figure 4.9: Maximum swelling as a function of local dpa in ferrite phase, in a comparison with swelling of ferritic MA957 [21, 22]

.

al. [5, 70], and the ∼0.12 %/dpa steady-state swelling rate shown in a recent study of $\alpha$-Fe under self-ion irradiation [28]. This suggested that the incubation period before onset of steady-state swelling has not yet been reached in the 12Cr dual-phase alloy [22, 5]. The tempered martensite phase is known to have an even longer incubation period under ion irradiation, as observed in the two-phase alloy EM12 and EP-450 [66, 56, 67].

In Fig. 4.10, we schematically show the understanding of the effects of dispersoids on void swelling and mechanical strength. The strong resistance to void swelling probably arises from a combination of factors. First, presence of fine grain structures with high boundary area is thought to provide defect trapping and annihilation sites [71, 22, 26, 72]. Higher densities of internal boundaries characteristic of tempered martensite may be critical to the swelling resistance. The fine grain structure and internal boundaries are also known to elevate hardness in F/M steels or F/M based ODS alloys [73]. The stability of grain sizes observed in this study suggests that both swelling resistance and hardness can persist to very high irradiation, possibly as a consequence of dispersoid locking and stabilizing of grain walls. Although there is larger swelling in the ferrite grains, a trade-off between swelling resistance and strength and ductility was made by optimizing composition, heat treatment and dispersoid volume and size [20]. In ferrite grains, dispersoids are finer with a higher density. As suggested by Ukai, such ultra fine dispersoids lead to enhanced hardness, creep rupture strength and tensile strength [19]. On the other hand, tempered martensite grains having larger dispersoid and larger dispersoid distance is likely to be less hard compared to ferrite. The ferrite grains surrounding tempered martensite grains are critical to maintaining the appropriate creep rupture strength.

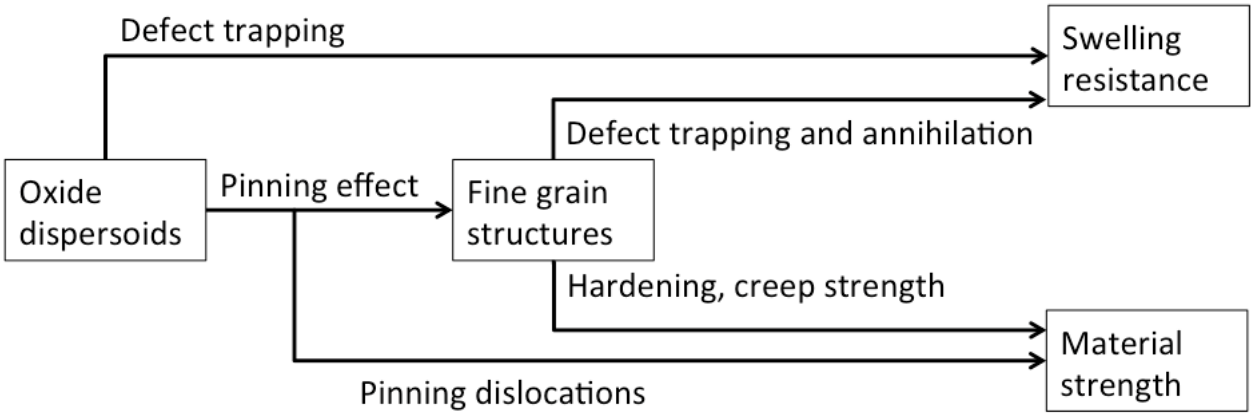


Figure 4.10: Schematic showing mechanisms of dispersoid effects on void swelling and mechanical properties [21]

Second, the finely distributed dispersoids of high density appear to have enhanced the swelling resistance, probably by playing two roles, stabilizing grain structures and trapping of defects. Previous studies showed that fine dispersoids suppress growth and recrystallization of grains [74] and phase transformations [20, 58]. The drag force applied to boundaries by dispersoids has been found to be stronger for finer size dispersoids [20, 58, 39]. In addition, as reported by Allen, et al. high-density dislocation segments were observed in a 9Cr ODS alloy both before and after irradiation [69, 38]. Dispersoids were suggested to immobilize dislocations both within the grain and on the boundary walls, thereby preventing dislocation recovery under high-temperature irradiation [69, 38]. On the other hand, the interface between dispersoids and the matrix has been reported to serve as defect recombination sites [69, 22, 75]. In a spherical 200 nm tempered martensite grain with dispersoid distribution reported earlier, the ratio of dispersoid-matrix interface to grain boundary area would be approximately 30% before irradiation, which is reduced after irradiation, due to the loss of dispersoid. Without evaluating the defect trap strength of dispersoid-matrix

interface, the dominating surface area of grain boundary in tempered martensite suggests its more important role in swelling resistance.

### *4.3.2 Dispersoids Under Irradiation*

During irradiation, the loss of the less-frequent, larger dispersoids in the alloy of this study is insufficient to overcome the much higher density of small dispersoids, especially since the lost yttria volume appears to be partially compensated by the increased density of smaller dispersoids in tempered martensite.

The shrinkage in dispersoid size suggests the operation of a ballistic dissolution mechanism but the quickly reached equilibrium size suggests the presence of rather strong healing by re-precipitation processes. Notably, the equilibrium dispersoid size was not strongly correlated to the local dpa rate, indicating the strong influence of these healing mechanisms. This may be due in part to the strong insolubility of yttrium in the presence of excess oxygen.

Diffusion mechanisms are believed to influence the changes in dispersoid size under irradiation [51, 76]. Based on Russell's radiation-affected precipitation model of equilibrium phases [51, 76], it is expected that large dispersoids would shrink and small dispersoids would grow under irradiation, although large precipitates in this scenario would fall to the equilibrium size and not disappear altogether, as was observed in this study. Russell's model predicts that the equilibrium size would be dependent on dpa rate, a phenomenon which was not observed in the present study. In addition, no coherency was observed for dispersoids larger than $\sim$10 nm in diameter and these larger dispersoids disappeared after irradiation, suggesting a

correlation between dispersoid-matrix coherency and dispersoid stability. As another evidence of this correlation, dispersoids in both phases were observed to maintain coherency relationships with the matrix after irradiation, as observed in this study and others [33, 50]. Further studies are needed on the radiation response of dispersoids at different temperatures and under different dpa rates, in order to understand the mechanisms in determining the irradiation-stable size and structures of dispersoids. Focuses should be put on interface structural configuration and interface energy differences of dispersoids having different sizes, as well as atomic scale details of how interfaces interact with point defects.

## 4.4 Conclusions

High dpa $Fe^{2+}$ ion irradiations up to 800 peak dpa were conducted on a dual-phase 12Cr ODS at 475 °C. The alloy is very stable under irradiation with grain/sub-grain structures that apparently not affected by radiation. During irradiation, dispersoids were found to reach to an equilibrium size and to change in density, while larger incoherent particles were destroyed. The equilibrium size, which was not observed to change as a function of dpa rate, was reached at as low as 60 dpa and was preserved to the highest irradiation level in this study. Dispersoids in ferrite grains were initially very close to the equilibrium size and therefore showed better irradiation stability than dispersoids in tempered martensite grains. There appears to be a correlation between coherency and dispersoid stability. Void swelling was found to be much higher in ferrite grains than in tempered martensite grains, but overall the alloy was rather resistant to void swelling.

# 5. RADIATION RESPONSE OF THE 12CR ODS: TEMPERATURE DEPENDENT

In last section we showed the grain stability, dispersoid stability and swelling resistance of the 12Cr dual-phase ODS alloy tested using self-ion irradiation at 475 °C. In this section, self-ion irradiations at various temperatures ranging from 325 °C to 625 °C were carried out to a 12Cr F/M ODS alloy containing tempered-martensite structure. After receiving peak dpa of 100 and 200 at each temperature, grain structures of this ODS were stable, while dispersoids shrank to equilibrium sizes, which are positively-related to the irradiation temperature. Weak-beam dark field micrographs show that dislocations were pinned even after 625 °C irradiations, exhibiting creep resistance strengthened by nano particles. Most dispersoids were found to be coherent to matrix after 475 °C irradiation; while $\sim 30\%$ dispersoids were not coherent after 625 °C irradiation. The evolution of dispersoid under irradiation can be understood by as a competition between radiation-driven removal and diffusion-driven recovery of dispersoid, with the latter influenced by the dispersoid-matrix interface configurations. Findings discussed in this section provides knowledge to predict nano-particle behavior under irradiation environment, which need to be carefully considered when designing radiation-tolerant materials.

## 5.1 Irradiation at Various Temperatures

It is well known that kinetic progresses are alway temperature-related. In studies of radiation response of materials, such relationship has been demonstrated. For example the peak swelling temperature as introduced in the first section as well as mentioned later in this section. Through the investigation in last section, we real-

ized that the dispersoid stability relies on the diffusion mechanism that 'heal' the dispersoids during irradiation. In a scenario of material under irradiation, in general, diffusion coefficients are attributed to thermal diffusion and radiation enhanced diffusion. And thermal diffusion coefficients are positively related to temperature. And in most cases, the total diffusion coefficient would also be increasing with temperature, as shown in Fig. 5.1 [23].

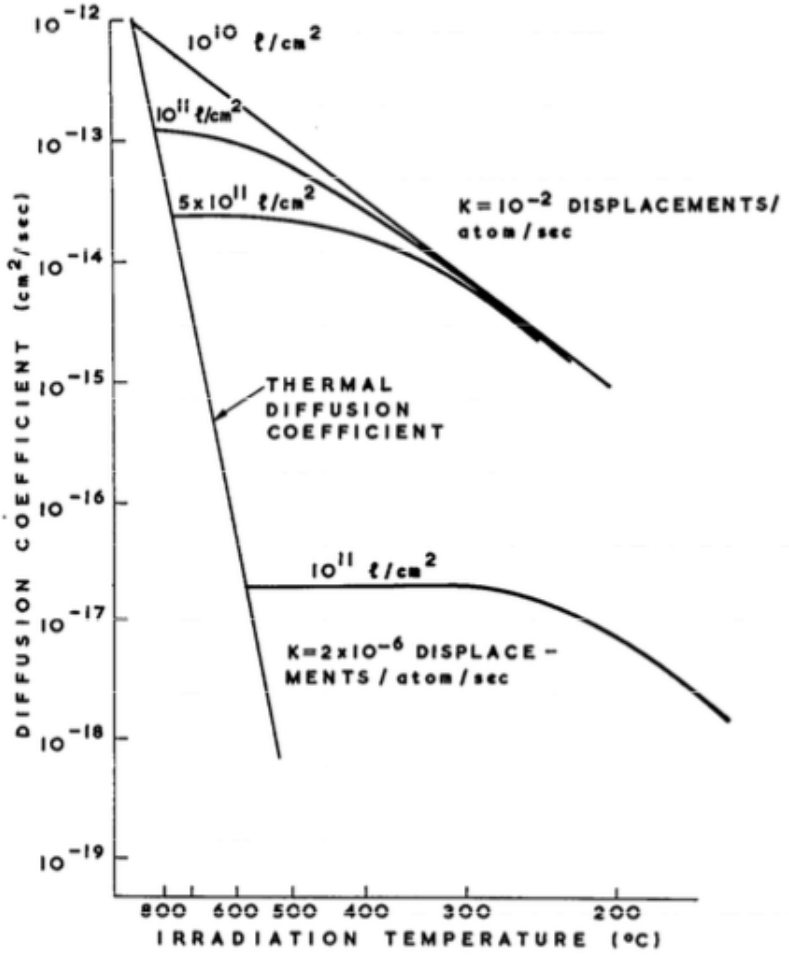


Figure 5.1: Radiation-enhanced diffusion coefficients for different dislocation densities at various damage rate [23]

In order to have a better understanding of irradiation temperature effect on microstructure changes to the 12Cr ODS, in addition to the 475 °C irradiation shown in last section, we carried out two more sets of irradiations at 325 °C and 625 °C, with each of them having two irradiations with peak damage of 100 and 200 dpa. The pre-irradiation sample preparation and experiment conditions were the same as described in last section.

## 5.2 Post-irradiation Characterizations

### *5.2.1 Grain Structure*

Figure 5.2 exhibit grain structures of samples before and after irradiations at various temperatures. In Fig. 5.2b-d, no obvious grain-size changes were observed due to irradiation at 325-625 °C, as compared to Fig. 5.2b. In addition, no obvious changes were found in either ferrite or tempered martensite structures in irradiated regions, exhibiting the radiation stability of both phases. Being able to maintain the mesoscopic structures under irradiations at elevated temperatures is very important to keep the enhanced creep strength of this material [19]. On the other hand, no void swelling was observed except for 475 °C sample. At 475 °C, more swelling occurs in ferrite grains than in tempered martensite grains, which has been reported earlier [21]. It is well known that void swelling peaks at the intermediate temperature, due to the reduction of defect mobility and the stability of vacancy loops at lower temperatures, and the vacancy flux being counterbalanced by the enhanced emission of vacancies from voids at higher temperatures [77, 6].

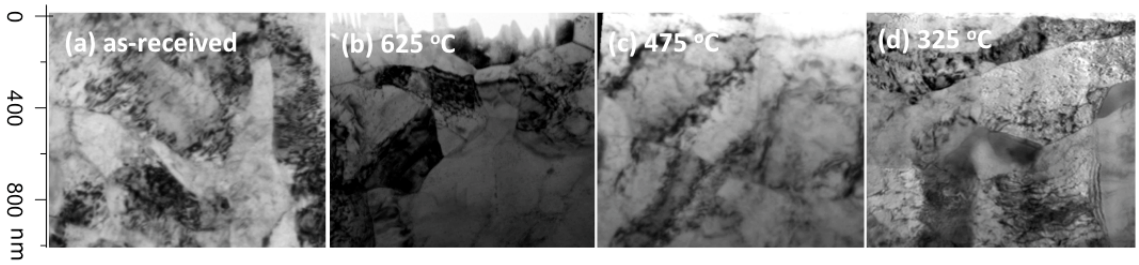


Figure 5.2: (a) Grain structure of as received sample, (b-d) irradiation surface (top) to peak dpa region (bottom) of samples receiving 200 peak dpa at 625 °C, 475 °C and 325 °C, respectively

### *5.2.2 Dispersoid Size Change*

Figure 5.3 shows TEM micrographs obtained in tempered martensite grains of samples receiving 100 and 200 peak dpa at different temperatures. Each micrograph was taken at the depth of 500 nm from the irradiating surface, so the local dpa of the regions of observation is approximately half of the peak dpa as labeled. Nano-sized dispersoids are shown as the gray spots in these conventional bright field images as a result of Z- and diffraction contrast. Compared to irradiation free sample shown in Fig. 5.3a, the size of dispersoids reduced due to damage bombardment. In addition, Fig. 5.3b-g shows that the dispersoid size is smaller at lower irradiation temperature.

Figure 5.4b exhibits dispersoid size changes correlated to depth, at different temperatures with different radiation damage levels, observed in tempered martensite grains. The corresponding damage rate at each depth is shown by Figure 5.4a. At each temperature, data points of different damage levels appear to converge. On the other hand, higher irradiation temperatures result in larger dispersoids on average. The dispersoid size begins to increase beyond ∼1000 nm, which is aligned with peak damage region simulated by SRIM, as shown in Fig. 5.4a. From the depth of ∼1000

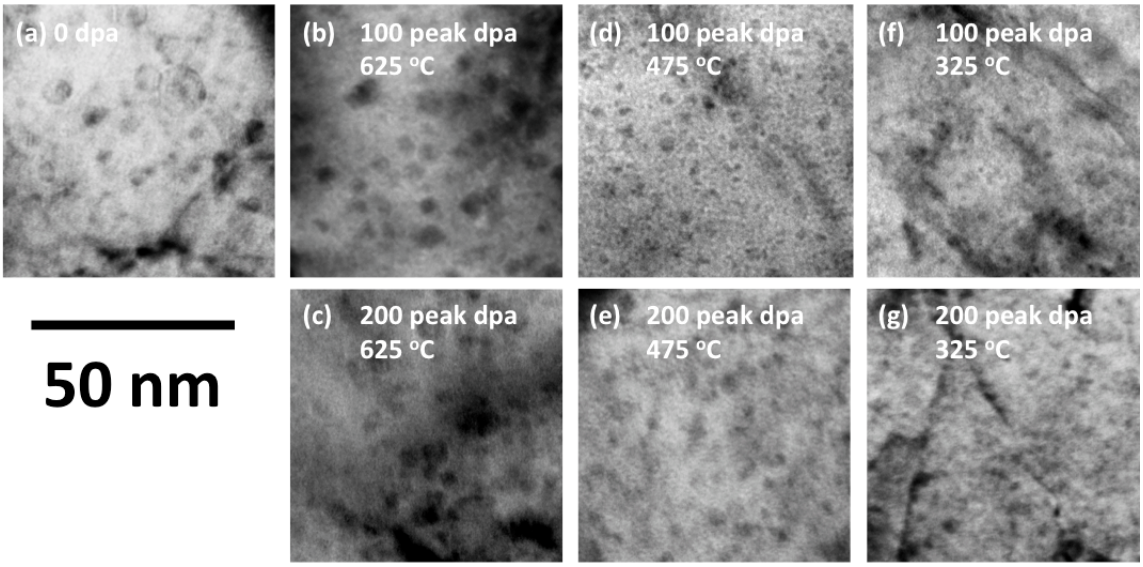


Figure 5.3: Bright field micrographs of dispersoids in tempered martensite phase under different irradiation conditions: (a) irradiation free sample, (b-c) 100 and 200 peak dpa samples irradiated at 625 °C, (d-e) 100 and 200 peak dpa samples irradiated at 475 °C, (f-g) 100 and 200 peak dpa samples irradiated at 325 °C

nm to the depth of ∼1600 nm, as dpa quickly reduced, mean dispersoid size increase back to the that of as-received condition.

Figure 5.5 plots the mean dispersoid size as a function of dpa. The temperature-dependent radiation-induced change in dispersoid size is demonstrated. In addition, at each temperature, it seems that the mean dispersoid size remains unchanged beyond a dpa of 60. This suggests that at certain stage, back-diffusion and recovery of dispersoids can counterbalance the removal of dispersoid atoms due to irradiation; and an steady-state of dispersoid distribution would be achieved.

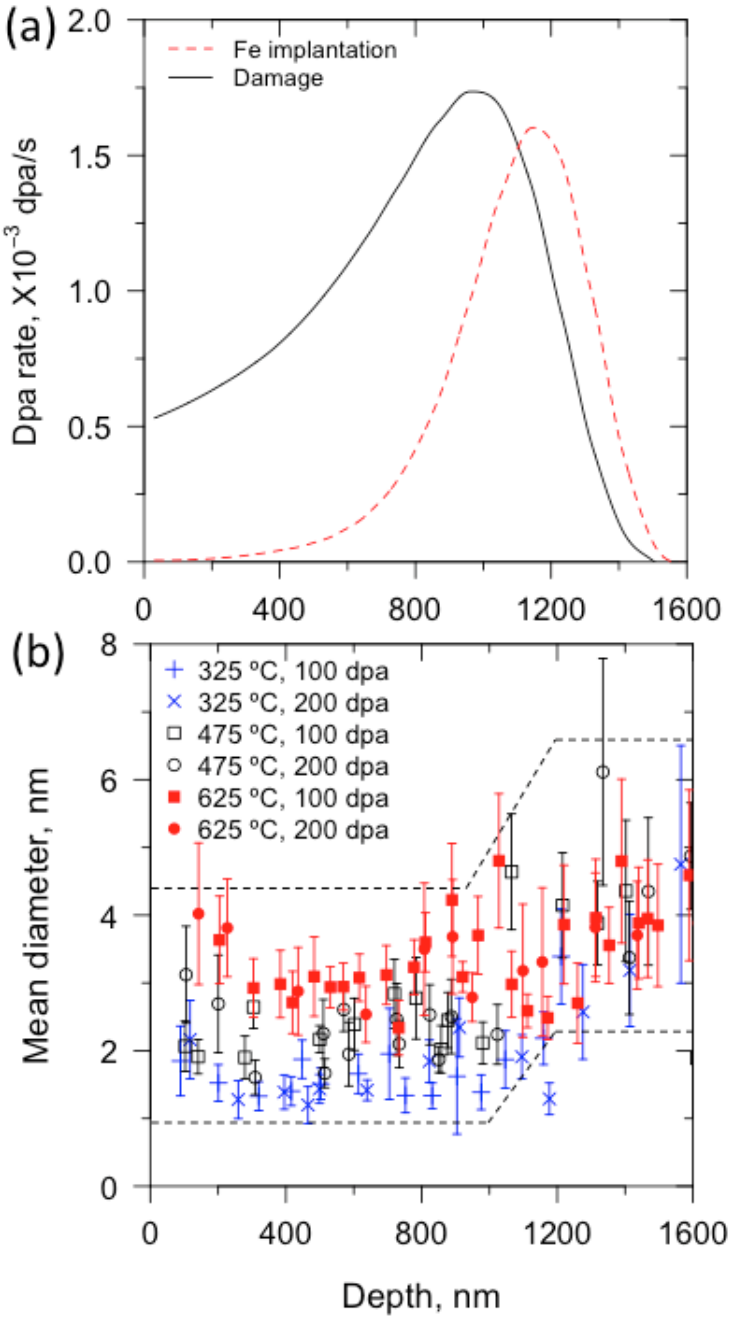


Figure 5.4: (a) SRIM simulation of 3.5 MeV self-ion irradiation into pure Fe, using a displacement threshold energy of 40 eV and the Kinchin-Pease option (b) mean dispersoid diameter in tempered martensite phase as a function of depth, under different irradiation conditions

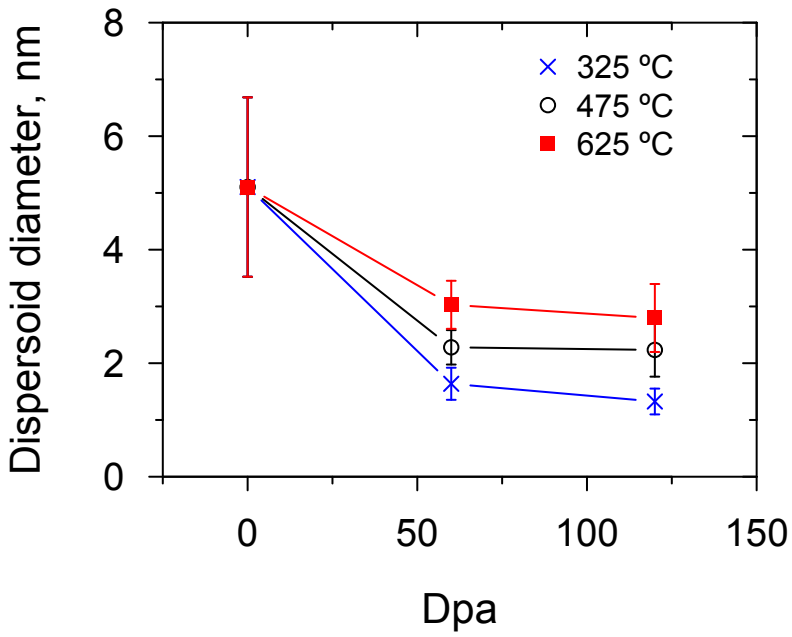


Figure 5.5: Mean dispersoid size as a function of dpa for different irradiation temperatures, generated using data obtained from 400-700 nm depth

### *5.2.3 Dispersoid Density and Coherency Change*

To enhance the diffraction contrast, a near two-beam condition was achieved, and BF and weak-beam dark field (WBDF) images were taken from randomly picked grains within regions receiving irradiation of ∼60-70 dpa at various temperatures, as shown in Fig 5.6. With $\mathbf{g}_{110}$ excited, WBDF images show prominent features such as coherent dispersoids and dislocations with burger's vectors not perpendicular to $\mathbf{g}_{110}$. Semi-coherent dispersoids were observed after 625 °C irradiation, as shown in the inserted figures in Fig 5.6c with misfit moir fringes. Semi-coherent dispersoids were not observed in any of the lower temperature irradiated samples. Arrows in Fig 5.6 highlights dislocations pinned by dispersoids in the matrix, which shows that the pinning effect of dispersoids provides enhancement to creep resistance by preventing dislocation migration at elevated temperatures up to 625 °C.

Number densities of coherent dispersoid can be obtained using WBDF images as they highlight coherent particles. Coherent dispersoid density in tempered-martensite grains before irradiation was measured to be $6.6 \pm 1.2 \times 10^{16} cm^{-3}$. As shown in table 5.1, the density appeared to slightly increase after 475 °C irradiation and decrease after 625 °C irradiation. Total dispersoid density regardless of their coherency was also estimated for samples before and after irradiation, by using BF micrographs. 325 °C irradiated sample was not included in table 5.1, because of the formation of high-density defects that will be explained later. The fraction of coherent dispersoid number to total dispersoid number is reduced in 625 °C irradiated sample compared to as-received and 475 °C irradiated sample, as shown in table 5.1.

Figure 5.7 plots distributions of dispersoid in size before and after receiving irra-

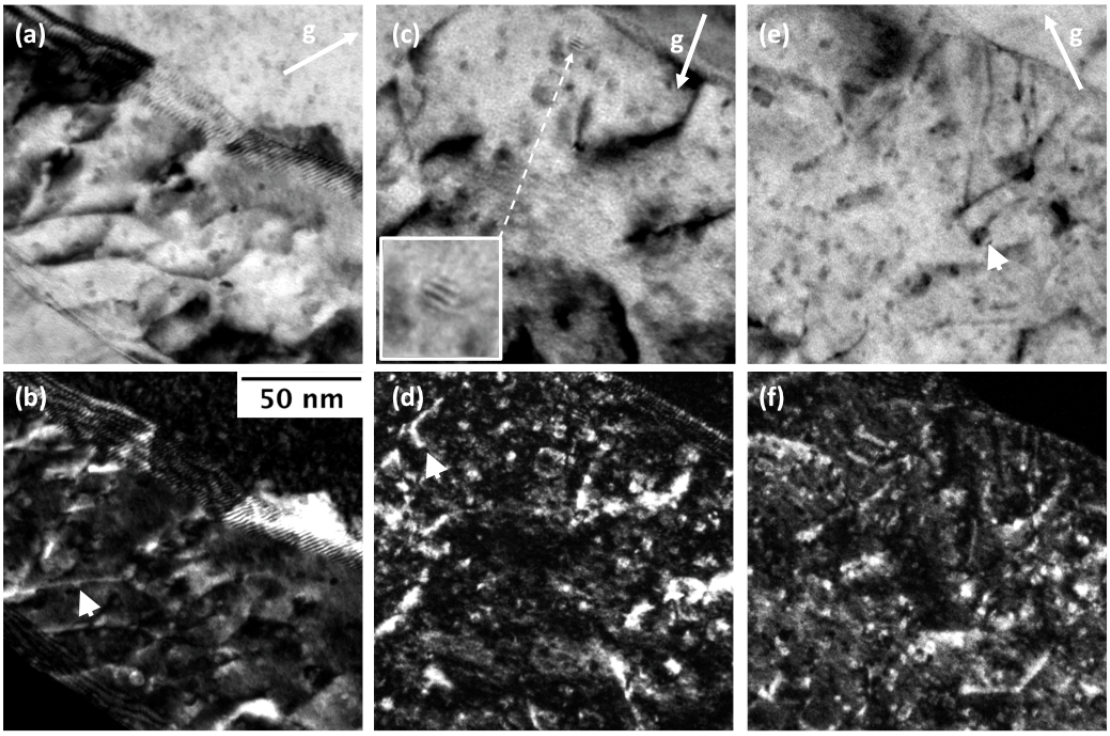


Figure 5.6: Bright field and weak beam dark field micrographs of tempered martensite grains obtained near $\mathbf{g}_{110}$: (a-b) irradiation free sample, (c-d) 625 °C irradiated sample with ∼65 dpa, (e-f) 475 °C irradiated sample with ∼65dpa

Table 5.1: Dispersoid densities in tempered martensite grains

| unit: $10^{16} cm^{-3}$ | As-received | 625 °C irradiated | 475 °C irradiated |
|---|---|---|---|
| Total dispersoid $\rho_t$ | 7.6 ± 0.6 | 5.4 ± 1.4 | 12.4 ± 2.6 |
| Coherent dispersoid $\rho_c$ | 6.6 ± 1.2 | 3.7 ± 1.5 | 11.4 ± 1.2 |
| $\rho_c$:$\rho_t$ | 87% | 69% | 92% |

diation at different temperatures, obtained from BF and WBDF micrographs of multiple randomly picked tempered-martensite grains in irradiated regions, using at least 100 particles for each category. Each group, i.e., coherent or total, was normalized over its own total number. Agreeing to observations from conventional BF micrographs, dispersoids were found to shrink in size after irradiation, with the broadness of size distribution decrease with decreasing irradiation temperature. Comparing coherent and total distributions in Fig. 5.7a, it is evident that larger dispersoid tend to be incoherent while most of the smaller dispersoids are coherent. After irradiation at 475°C, the coarse and incoherent dispersoids seemed to disappear as shown in Fig. 5.7c; however, more larger and incoherent dispersoids were found after 625°C irradiation, as shown in Fig. 5.7b.

Figure 5.8ab presents WBDF micrographs near $\mathbf{g}_{002}$ and $\mathbf{g}_{110}$ of one tempered martensite grain receiving ∼65 dpa at 325 °C. Compared to microstructures from higher-temperature irradiations shown in Fig. 5.6eg, features shown in Fig. 5.8ab are finer and denser, whose distribution is plotted in Fig. 5.8c. These features are most likely to include the so-called black spot damages, dislocation loops (as shown in the inserted micrograph in Fig. 5.8b) yttria dispersoids and other precipitates, based on previous observations in F/M steels and ODS irradiated under similar conditions [78, 11, 47, 79, 80, 33, 36]. Although it is impossible to distinguish yttria from other features due to its ultra-fine size after irradiated at 325 °C, the size distribution of yttria is part of the distribution shown in Fig. 5.8c. Compared to results of higher temperature irradiations in Fig. 5.7bc, the dispersoid, if still exist after 325 °C self-ion irradiation, has a distribution of smaller size and narrower range.

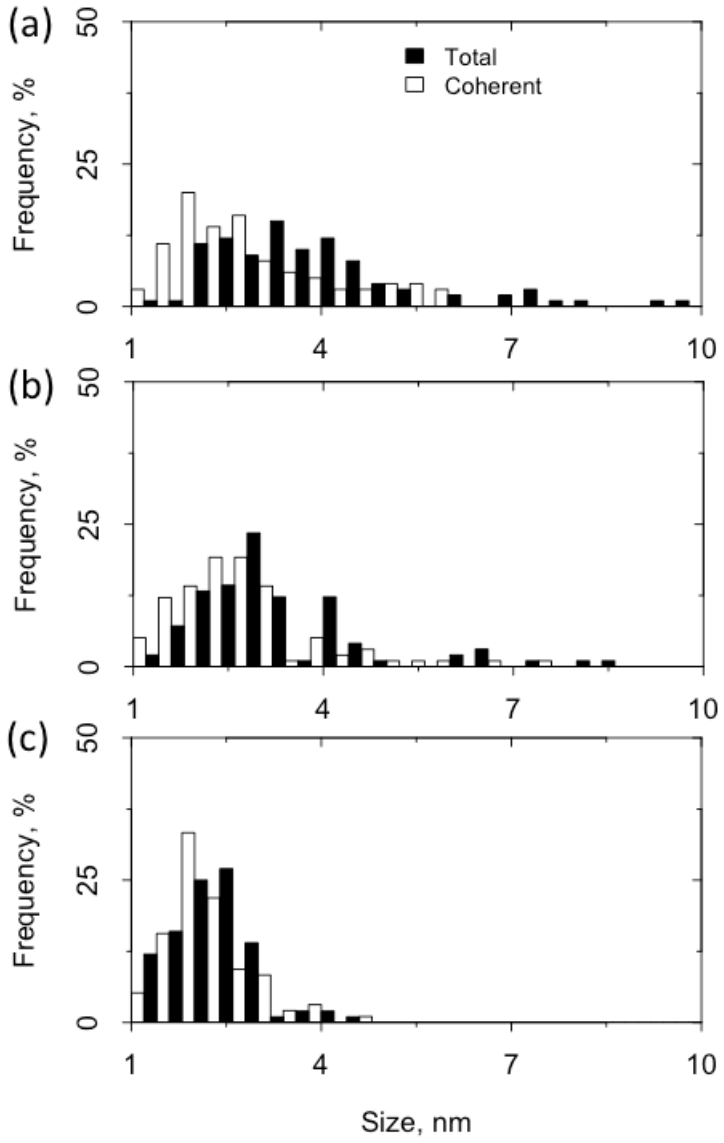


Figure 5.7: Size distributions of total and coherent dispersoid in tempered martensite phase: (a) irradiation free sample, (b) 625 °C irradiated sample, (c) 475 °C irradiated sample

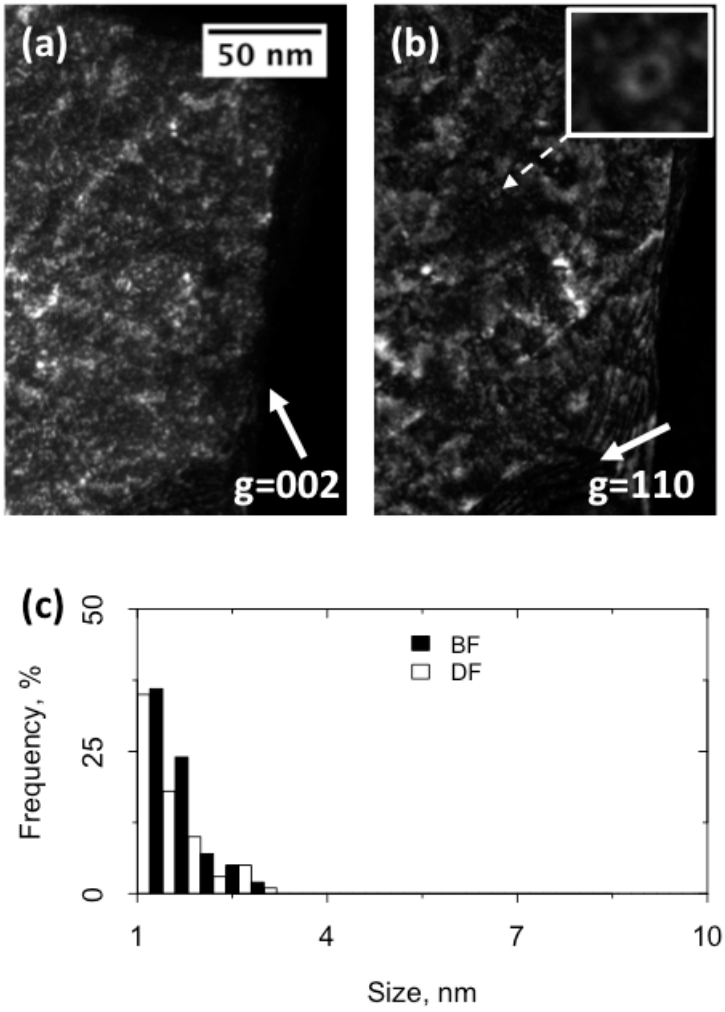


Figure 5.8: (a-b) WBDF micrographs near $\mathbf{g}_{002}$ and $\mathbf{g}_{110}$ from a tempered-martensite grain receiving ∼65 dpa at 325 °C, respectively; (c) Feature size distribution obtained from BF and WBDF micrographs

## 5.3 Discussion

### *5.3.1 Relationship Between Material Strength and Dispersoid Distribution*

The correlation of dispersoid coherency and dispersoid size has been reported in ODS alloys [21, 81, 82, 83]. In general small dispersoids tend to have various coherency relationships to matrix [21, 81] while large dispersoids tend to be semi-coherent [82] and eventually lose coherency as they become larger [21, 81, 82]. Thermal dynamically, this correlation is a result of minimization of free energy [81]. The free energy of an ideal spherical dispersoid can be described as a sum of interfacial energy and elastic energy. The interfacial energy of a spherical particle with radius r is $4\pi r^2 \cdot \gamma_i$, where $\gamma_i$ is the unit-area interface energy. For an incoherent dispersoid, the elastic energy is negligible compared to interfacial energy, given the elastic moduli of the matrix and the dispersoids are relatively close [64]. For a coherent dispersoid, however, the strain energy introduced due to the lattice misfit $\delta$ should be considered as $4\pi r^3/3 \cdot 4\delta^2\mu$ [84]. Given that coherent interface has a smaller $\gamma_i$, a competition between interface energy and elastic energy leads to smaller dispersoids taking coherency while larger dispersoids not.

ODS alloys with finer dispersoids have been experimentally observed to have higher creep rupture strength [85, 86, 87], in which dispersoids stabilize grain structures and pin dislocations to enhance the creep resistance [12, 40, 88]. The effect of pinning of particles on grain boundaries, or the Zener pinning, has been found to be inversely proportional to particle size, with coherent particles being more effective than incoherent particles [39, 89]. Meanwhile, it appears that finer dispersoids with higher number density have a stronger pinning effect on dislocations [86]. For the case of Y-Ti-O dispersoids, the elastic moduli of dispersoids are slightly larger than

that of the matrix, as shown by synchrotron X-ray diffraction during tensile tests [64]. In this scenario, incoherent particles might have less attraction to dislocations due to a repulsive contribution resulted from such moduli difference [12, 40]. In this work, evidences of pinned dislocations were observed up to an irradiation temperature of 625 °C, as shown in Fig 5.6. The presence of dispersoids without significant loss of density, after high temperature irradiation, is believed to impede dislocation climb.

### *5.3.2 Kinetics of Dispersoid Evolution Under Irradiation*

Knowing the significant role of dispersoid on enhancing creep resistance of ODS alloy, it is of great importance to understand the stability of dispersoids under irradiation at different temperatures. As exhibited in Fig. 5.4b, dispersoids reduced in size after receiving self-ion irradiations at various temperatures. Instinctively, the reduction in dispersoid is attributed to irradiation dissolution [23, 90]. R.S. Nelson proposed two mechanisms of radiation-enhanced dissolution of precipitates, namely, recoil dissolution and disordering dissolution [23]. Although not shown in this report for the sake of conciseness, irradiation induced dispersoid amorphization was shown by the same material irradiated using the same beam configuration at room temperature to a peak dpa of 100, indicating that disordering dissolution was taking place during irradiation. At elevated temperatures where diffusion occurs, disordering created within the precipitates will re-order while the disordered atoms with high concentration near the surface of precipitate will diffuse to the matrix [23]. The loss of precipitates due to irradiation is governed by:

$$\frac{dr}{d\phi} = -\psi = -l \cdot f \tag{5.1}$$

where $\psi$ is the product of damage cascade size $l$ in a dimension of distance, and a dimensionless $f$ indicating the fraction of atoms dissolved due to damage cascade. $\phi$ is radiation damage in terms of dpa. Given a constant dpa rate K, $\phi$ and time t has a linear relationship:

$$d\phi = K \cdot dt \tag{5.2}$$

On the other hand, as shown in Fig 5.5 as well as in earlier studies [21, 51], an equilibrium dispersoid size can be approached after certain amount of dpa. This indicates a recovery mechanism plays a role under irradiation environment, which is believed to be realized through diffusion. A simple treat for diffusion-driven precipitate radius growth, $dr/dt$, has been proposed as [23, 90]:

$$\frac{dr}{dt} = \frac{D}{r} \cdot \frac{3c}{4\pi c_p} \tag{5.3}$$

where $D$ is the solute diffusion coefficient, combined thermal diffusion and radiation-enhanced diffusion, $c_p$ is the solute concentration in precipitate and $c$ is the solute concentration in solution. Substituting Eq. 5.1 and Eq. 5.2 into Eq. 5.3, and considering an equilibrium situation when $dr/d\phi = 0$, the radiation-induced precipitate shrinkage is counterbalanced by the diffusion-driven precipitate growth, leading to an equilibrium precipitate size under irradiation:

$$r_e = \frac{D}{K\psi} \cdot \frac{3c}{4\pi c_p} \tag{5.4}$$

Equation 5.4 shows that under the same irradiation condition, the equilibrium dispersoid size increase with increasing diffusion coefficients. Diffusion coefficients in-

crease with temperature, which is still true but with a smaller increasing slope when radiation-enhanced diffusion plays a role. Qualitatively, dispersoids having larger sizes at higher irradiation temperatures as reported in this work and earlier [36], can be understood as the result of competition between radiation-removal and diffusion-growth. Considering that the neutron-induced damage rate in reactors is much lower compared to accelerator-induced ion irradiations, dispersoids might be undergo smaller changes in size or even coarsen under neutron irradiation [48, 42, 43].

Besides size changes, more incoherent dispersoids were observed after 625 °C irradiation compared to 475 °C irradiation, as shown in table 5.1 and Fig 5.6. It appears that the recovery of incoherent dispersoids at 475 °C was impeded. As a result, most of the observed dispersoids after irradiation at 475 °C were coherent. In addition, the increase in dispersoid density after 475 °C irradiation suggests larger dispersoids break into smaller ones and/or re-nucleation of dispersoid occurs during irradiation.

Given the size of dispersoid is in the order of nm, it would be appropriate to take account of the interface effect with high curvature nature of these particles, i.e., the Gibbs-Thomson effect. The diffusion-driven growth would then involve a term $c_r$, which is the solubility limit at the precipitate/matrix interface [91, 92]:

$$\frac{dr}{dt} = \frac{D}{r} \cdot \frac{c - c_r}{c_p - c_r} \tag{5.5}$$

$c_r$ can be estimated from the solubility limit of of a flat interface $c_\infty$, using the following equation in the case of diluted solid solution, i.e, $c_r \ll 1$, as it is in this study [93]:

$$c_r = c_\infty exp(\frac{2\gamma_i \nu_{at}}{kTr}) \tag{5.6}$$

where $\nu_{at}$ is the averaged atomic volume in precipitate, k is the Boltzmann constant and T is the temperature.

Given that $c \ll c_p$ in this study, the diffusion-induced precipitate growth in Eq. 5.5 is negatively related to $c_r$. Substituting Eq. 5.6 into Eq. 5.5, it can be known that the diffusion-driven growth of precipitates can be impeded due to high interface energy between the precipitate and the matrix; on the other hand, higher temperature and larger dispersoid size will enhance the diffusion-driven growth. Thus, at 475 °C when the averaged dispersoid size is relatively smaller, the Gibbs-Thomson effect takes place and prevent the recovery of incoherent dispersoids due to their high interface energies; at 625 °C, however, higher temperature and larger dispersoid size lead to a smaller $c_r$, allowing the incoherent dispersoids to exist under an irradiation condition.

The range of energies of coherent and incoherent dispersoid-matrix interfaces can be estimated using Eq. 5.5 and Eq. 5.6. Assuming $Y_2Ti_2O_7$ composition of the atoms, $\nu_{at} \approx 0.1\ nm^3$; $c_\infty$ was estimated using the solubility of Y in $\alpha$-Fe, which is 0.02 at.% and 0.013 at.% for 625 °C and 475 °C, respectively [94]. $c$ is $\sim$ 0.1 at.% after 475 °C and 625 °C irradiations, calculated from the dispersoid distributions before and after irradiations. The critical interface energy $\gamma_i$ at 475 °C above which Eq. 5.5 = 0 was calculated to be 0.25 $J/m^2$, providing the average dispersoid diameter after 475 °C irradiation is 2.4 nm. And the critical energy of incoherent/semi-coherent interfaces to survive after 625 °C irradiation was calculated to be 0.4 $J/m^2$, using a dispersoid diameter of 4.0 nm, where incoherent dispersoids were mostly found as shown in Fig 5.7b. Thus, coherent dispersoids should have an interface energy no larger than 0.25 $J/m^2$ in order to survive under 475 °C irradiation; on the other

hand, the interface energy of semi-coherent/incoherent dispersoids as formed under 625 °C irradiation should be larger than 0.25 $J/m^2$ while smaller than 0.4 $J/m^2$. Such estimation is in agreements with the 0.26 $J/m^2$ interface energy of coherent $Y_2Ti_2O_7$ reported by Ribis et al [95], and the 0.3-2.5 $J/m^2$ energy range of incoherent and semi-coherent interfaces reported by J.M. Howe [96].

## 5.4 Conclusions

To understand radiation response of dispersoid in a F/M ODS with tempered-martensite structure, microstructure investigations and statistics of dispersoid size, density and interfacial coherency were carried out after 3.5 MeV $Fe^{2+}$ irradiations at 325, 475 and 625 °C. The grain and sub-grain structures were found to be stabile in the irradiation temperature range of 325 °C to 625 °C with a highest peak dpa of 200. Swelling was only found at 475 °C. Higher and lower temperatures were found to suppress void formation. Compared to the irradiation free sample, dispersoids were found to shrank after irradiation, approaching to an equilibrium size that is positively related to irradiation temperatures. Dislocations pinned by dispersoids were observed after irradiations, exhibiting the creep strengthening mechanisms of dispersoids at elevated irradiation temperatures. Dispersoid-matrix coherency was observed to be influenced by dispersoid size and irradiation temperatures. Such coherency complexity is due to the higher interface energy of semi-coherent/incoherent dispersoids compared to coherent dispersoids.

# 6. SUMMARY

In this study, a series of self-ion irradiations were carried out onto a novel 12Cr ODS dual-phase alloy, which is designed to have improved high-temperature strength and radiation resistance. Primarily through the high dose irradiations at 475 °C, the radiation tolerance of this material is directly demonstrated; meanwhile, the stability of dispersoids suggests its high creep resistance should also be maintained after receiving high dpa radiation damage. On the other hand, by analyzing dispersoid changes at different irradiation temperatures, more understanding of the mechanisms of radiation removal and diffusion-driven recovery of dispersoid was gained. Particularly, the dispersoid-matrix interface configuration was shown to influence the recovery progress. Some important conclusions were summarized in the the following bullets.

Microstructure investigation of the 12Cr dual-phase ODS alloy shows:

(1) Through the equilibrium state predicted by the phase diagram together with the pinning effect of fine oxide particles on phase boundaries, the ratio of harder ferrite grains and softer tempered martensite grains could be controlled, which enhance the creep rupture strength of the material.

(2) Ferrite grains have finer and denser dispersoids whilst tempered martensite grains have a broader distribution of dispersoid in size. The coarser dispersoids found in tempered martensite grains were believed to be the result of Ostwald ripening of dispersoids lost coherency with the matrix during phase transformation.

(3) The chemical composition of most dispersoids were found to be Y-Ti-O.

(4) The coherency between dispersoid and matrix seems to be size dependent, with

smaller dispersoids tend to be coherent and larger dispersoids tend to be not.

12Cr ODS radiation tolerance studied using high damage (up to 800 peak dpa) self-ion irradiation at 475 °C shows:

(1) The grain and sub-grain structures were found to be stabile under irradiation conditions.

(2) The swelling resistance of both ferrite grains and tempered martensite grains are relatively high compared with other F/M steels or ODS alloys. The swelling in ferrite grains is at least one order of magnitude higher than it in tempered martensite grains.

(3) Dispersoids were shown to survive after high dpa damage, with an equilibrium size that is smaller than irradiation-free case approached after irradiated at 475 °C.

(4) The high swelling resistance was believed to be achieved by a combination efforts from high density grain/sub-grain boundaries in tempered martensite phase and dispersoid-matrix interface, both serving as defect trapping sites.

(5) Dispersoids were believed to stabilize grain/sub-grain structures and immobilize dislocations, which can enhance the material strength and creep resistance.

Dispersoid evolution due to ion-irradiation studied using self-ion irradiations at various temperatures shows:

(1) Up to 625 °C, dispersoids were found to reduce in size after irradiations, with the equilibrium size reached due to irradiation positively related to irradiation temperature.

(2) Diffusion was found to be the recovery mechanism for dispersoids under irradiation. The effect is positively related to irradiation temperature. When diffusion and radiation removal of dispersoid counterbalance each other, an equilibrium dispersoid

size can be reached, which is higher with higher radiation temperature and lower dpa rate.

(3) Dispersoids with smaller diameter and higher interface energy with the matrix were less favorable to diffusion-driven recovery.

# REFERENCES


[1] T. Abram and S. Ion. Generation-iv nuclear power: A review of the state of the science. *Energy Policy*, 36:4323–4330, 2008.

[2] C.E. Till and Y.I. Chang. *Plentiful Energy*. Charles E. Till and Yoon Il Chang, 2011.

[3] S.J. Zinkle and J.T. Busby. Structural materials for fission and fusion energy. *Materials Today*, 12(11):12–18, 2009.

[4] L.K. Mansur. Theory and experimental background on dimensional changes in irradiated alloys. *Journal of Nuclear Materials*, 216:97–123, 1994.

[5] F.A. Garner, M.B. Toloczko, and B.H. Sencer. Comparison of swelling and irradiation creep behavior of fcc-austenitic and bcc-ferritic/martensitic alloys at high neutron exposure. *Journal of Nuclear Materials*, 276:123–142, 2000.

[6] G.S. Was. *Fundamentals of radiation materials science: metals and alloys*. Springer, 2007.

[7] F. Wetscher, R. Pippan, S. Sturm, F. Kauffmann, C. Scheu, and G. Dehm. Tem investigations of the structural evolution in a pearlitic steel deformed by high-pressure torsion. *Metallurgical and Materials Transactions A*, 37:1963–1968, 2006.

[8] S. Raoui, B. Marini, and A. Pineau. Effect of microstructure on the susceptibility of a 533 steel to temper embrittlement. *Journal of Nuclear Materials*, 257:199–205, 1998.

[9] J. W. Morris Jr, C. Kinney, K. Pytlewski, and Y. Adachi. Microstructure and cleavage in lath martensitic steels. *Science and Technology of Advanced Materials*, 14(014208), 2013.

[10] B. L. Bramfitt and A. O. Benscoter. *Metallographer's guide*. ASM International, 2002.

[11] R. Schäublin, D.S. Gelles, and M. Victoria. Microstructure of irradiated ferritic/martensitic steels in relation to mechanical properties. *Journal of Nuclear Materials*, 307-311:197–202, 2002.

[12] V.C. Nardone and J.K. Tien. Pinning of dislocations on the departure side of strengthening dispersoids. *Scripta METALLURGICA*, 17:467–470, 1983.

[13] L. Shao, C.C. Wei, J. Gigax, A. Aitkaliyeva, D. Chen, B.H. Sencer, and F.A. Garner. Effect of defect imbalance on void swelling distributions produced in pure iron irradiated with 3.5 mev self-ions. *Journal of Nuclear Materials*, 453:176–181, 2014.

[14] Inc. E.A. Fischione Instruments. Model 200 dimpling grinder.

[15] J. Ayache, L. Beaunier, J. Boumendil, G. Ehret, and D. Laub. *Sample Preparation Handbook for Transmission Electron Microscopy*. Springer, 2010.

[16] C.A. Volkert and A.M. Minor. Focused ion beam microscopy and micromachining. *MRS Bulletin*, 32:389–399, 2007.

[17] G.E. Lloyd. Atomic number and crystallographic contrast images with the sem: a review of backscattered electron techniques. *Mineralogical Magazine*, 51:3–19, 1987.

[18] D.B. Williams and C.B. Carter. *Transmission electron microscopy: a textbook for materials science*. Springer, 2009.

[19] S. Ukai and S. Ohtsuka. Nano-mesoscopic structure control in 9cr-ods ferritic steels. *Energy Materials*, 2(1):26–35, 2007.

[20] S. Ukai, Y. Kudo, X. Wu, N. Oono, S. Hayashi, S. Ohtsuka, and T. Kaito. Residual ferrite formation in 12crods steels. *Journal of Nuclear Materials*, 455:700–703, 2014.

[21] T. Chen, E. Aydogan, J.G. Gigax, D. Chen, J. Wang, X. Wang, S. Ukai, F.A. Garner, and L. Shao. Microstructural changes and void swelling of a 12cr ods ferritic-martensitic alloy after high-dpa self-ion irradiation. *Journal of Nuclear Materials*, 467:42–49, 2015.

[22] M.B. Toloczko, F.A. Garner, V.N. Voyevodin, V.V. Bryk, O.V. Borodin, V.V. Mel'nychenko, and A.S. Kalchenko. Ion-induced swelling of ods ferritic alloy ma957 tubing to 500 dpa. *Journal of Nuclear Materials*, 453:323–333, 2014.

[23] R.S. Nelson, J.A. Hudson, and D.J. Mazey. The stability of precipitates in an irradiation environment. *Journal of Nuclear Materials*, 44:318–330, 1972.

[24] Gen iv international forum, 2009.

[25] F. Carré, C. Renault, P. Anzieu, P. Brossard, and P. Yvon. Outlook on generation iv nuclear systems and related materials r and d challenges. In *Materials issues for genertation IV systems*, page 25, 2007.

[26] D. Chen, J. Wang, T. Chen, and L. Shao. Defect annihilation at grain boundaries in alpha-fe. *Scientific Reports*, 3(1450), 2013.

[27] O.D. Sherby and P.M. Burke. Mechanical behavior of crystalline solids at elevated temperature. *Progress in Materials Science*, 13:323–390, 1968.

[28] J. Gigax, E. Aydogan, T. Chen, D. Chen, Y. Wu, W.Y. Lo, Y. Yang, and F.A. Garner. The influence of beam rastering on the swelling of self-ion irradiated pure iron at 450 °C. *Journal of Nuclear Materials*, submitted.

[29] C.H. Woo and B.N. Singh. The concept of production bias and its possible role in defect accumulation under cascade damage conditions. *physica status solidi (b)*, 159:609–616, 1990.

[30] R. Irmann. Sintered aluminum with high strength at elevated temperatures. *Metallurgia*, 49:125, 1952.

[31] R.L. Klueh and A.T. Nelson. Ferritic/martensitic steels for next-generation reactors. *Journal of Nuclear Materials*, 371:37–52, 2007.

[32] R.L. Klueh, J.P. Shingledecker, R.W. Swindeman, and D.T. Hoelzer. Oxide dispersion-strengthened steels: a comparison of some commercial and experimental alloys. *Journal of Nuclear Materials*, 341:103–114, 2005.

[33] J. Ribis and S. Lozano-Perez. Nano-cluster stability following neutron irradiation in ma957 oxide dispersion strengthened material. *Journal of Nuclear Materials*, 444:314–322, 2014.

[34] C.M. Parish, R.M. White, J.M. LeBeau, and M.K. Miller. Response of nanostructured ferritic alloys to high-dose heavy ion irradiation. *Journal of Nuclear Materials*, 445:251–260, 2014.

[35] M.K. Miller, D.T. Hoelzer, E.A. Kenik, and K.F. Russell. Stability of ferritic ma/ods alloys at high temperatures. *Intermetallics*, 13:387–392, 2005.

[36] J. He, F. Wan, K. Sridharan, T.R. Allen, A. Certain, V. Shutthanandan, and Y.Q. Wu. Stability of nanoclusters in 14ywt oxide dispersion strengthened steel

under heavy ion-irradiation by atom probe tomography. *Journal of Nuclear Materials*, 455:41–45, 2014.

[37] A. Alamo, J.L. Bertin, V.K. Shamardin, and P. Wident. Mechanical properties of 9cr martensitic steels and ods-fecr alloys after neutron irradiation at 325 °c up to 42dpa. *Journal of Nuclear Materials*, 367-370:54–59, 2007.

[38] T.R. Allen, J. Gan, J.I. Cole, S. Ukai, S. Shutthanandan, and S. Thevuthasan. The stability of 9cr-ods oxide particles under heavy-ion irradiation. *Nuclear Science and Engineering*, 151:305–312, 2005.

[39] E. Nes, N. Ryum, and O. Hunderi. On the zener drag. *Acta Materialia*, 33:11–22, 1985.

[40] V.C. Nardone, D.E. Matejczyk, and J.K. Tien. The threshold stress and departure side pinning of dislocations by dispersoids. *Acta Materialia*, 32:1509–1517, 1984.

[41] H.G. Armaki, R. Chen, K. Maruyama, and M. Igarashi. Creep behavior and degradation of subgrain structures pinned by nanoscale precipitates in strength-enhanced 5 to 12 pct cr ferritic steels. *Metallurgical and Materials Transactions A*, 42A:3084–3094, 2011.

[42] S. Yamashita, N. Akasaka, and S. Ohnuki. Nano-oxide particle stability of 9–12cr grain morphology modified ods steels under neutron irradiation. *Journal of Nuclear Materials*, 329-333:377–381, 2004.

[43] S. Yamashita, N. Akasaka, S. Ukai, and S. Ohnuki. Microstructural development of a heavily neutron-irradiated ods ferritic steel (ma957) at elevated temperature. *Journal of Nuclear Materials*, 367-370:202–207, 2007.

[44] A.G. Certain, K.G. Field, T.R. Allen, M.K. Miller, J. Bentley, and J.T. Busby. Response of nanoclusters in a 9cr ods steel to 1 dpa, 525 °C proton. *Journal of Nuclear Materials*, 407:2–9, 2010.

[45] M.-L. Lescoat, I. Monnet, J. Ribis, P. Dubuisson, Y. de Carlan, J.-M. Costantini, and J. Malaplate. Amorphization of oxides in ods materials under low and high energy ion irradiations. *Journal of Nuclear Materials*, 2011.

[46] V.A. Skuratov. Radiation stability of the ods alloys against swift heavy ion impact. *Journal of Nuclear Materials*, 442:449–457, 2013.

[47] R. Schäublin, A. Ramar, N. Baluc, V. de Castro, M.A. Monge, T. Leguey, N. Schmid, and C. Bonjour. Microstructural development under irradiation in european ods ferritic/martensitic steels. *Journal of Nuclear Materials*, 351:247–260, 2006.

[48] N. Akasaka, S. Yamashita, T. Yoshitake, S. Ukai, and A. Kimura. Microstructural changes of neutron irradiated ods ferritic and martensitic steels. *Journal of Nuclear Materials*, 329-333:1053–1056, 2004.

[49] H. Kishimoto, K. Yutani, R. Kasada, O. Hashitomi, and A. Kimura. Heavy-ion irradiation effects on the morphology of complex oxide particles in oxide dispersion strengthened ferritic steels. *Journal of Nuclear Materials*, 367-370:179–184, 2007.

[50] M.-L. Lescoat, J. Ribis, Y. Chen, E.A. Marquis, E. Bordas, P. Trocellier, Y. Serruys, A. Gentils, O. Kaïtasov, Y. de Carlan, and A. Legris. Radiation-induced ostwald ripening in oxide dispersion strengthened ferritic steels irradiated at high ion dose. *Acta Materialia*, 78:328–340, 2014.

[51] T.R. Allen, J. Gan, J.I. Cole, M.K. Miller, J.T. Busby, S. Shutthanandan, and S. Thevuthasan. Radiation response of a 9 chromium oxide dispersion strengthened steel to heavy ion irradiation. *Journal of Nuclear Materials*, 375:26–37, 2008.

[52] I. Monnet, P. Dubuisson, Y. Serruys, M.O. Ruault, O. Kaïtasov, and B. Jouffrey. Microstructural investigation of the stability under irradiation of oxide dispersion strengthened ferritic steels. *Journal of Nuclear Materials*, 335:311–321, 2004.

[53] F.A. Garner. Impact of the injected interstitial on the correlation of charged particle and neutron-induced radiation damage. *Journal of Nuclear Materials*, 117:177–197, 1983.

[54] R.L. Klueh and D.R. Harries. *High-chromium ferritic and martensitic steels for nuclear applications*. ASTM International, West Conshohocken, PA, 2001.

[55] F.A. Smidt Jr., P.R. Malmberg, J.A. Sprague, and J.E. Westmoreland. *Swelling behavior of commercial ferritic alloys, EM-12 and HT-9, as assessed by heavy ion bombardment*, volume STP 611, chapter Irradiation Effects on the Microstructure and Properties of Metals, pages 227–241. ASTM International, Philadelphia, PA, 1976.

[56] V. Bryk, O. Borodin, A. Kalchenko, V. Voyevodin, V. Ageev, A. Nikitina, V. Novikov, V. Inozemtsev, A. Zeman, and F.A. Garner. Ion issues on irradiation behavior of structural materials at high doses and gas concentrations. In *Proceedings of Accelerator Applications*, page 1, Bruges, Belgium, 2013.

[57] S. Ukai. *Metal, ceramic and polymeric composites for various uses*. ISBN 978-953-307-353-8. InTech, 2011.

[58] M. Yamamoto, S. Ukai, S. Hayashi, T. Kaito, and S. Ohtsuka. Reverse phase transformation from alpha to gamma in 9cr-ods ferritic steels. *Journal of Nuclear Materials*, 417:237–240, 2011.

[59] Y. Yazawa, T. Furuhara, and T. Maki. Effect of matrix recrystallization on morphology, crystallography and coarsening behavior of vanadium carbide in austenite. *Acta Materialia*, 52:3727–3736, 2004.

[60] ASTM E521-83. *Standard practice for neutron radiation damage simulation by charged-particle irradiation*, volume 12.02. ASTM International, 2009.

[61] J.F. Ziegler, M.D. Ziegler, and J.P. Biersack. Srim - the stopping and range of ions in matter. *Nuclear Instruments and Methods in Physics Research B*, 268:1818–1823, 2010.

[62] L.R. Greenwood and R.K. Smither. Specter: neutron damage calculations for materials irradiations. Technical Report ANL/FPP/TM-197, Argonne National Laboratory, Lemont, IL, 1985.

[63] R.E. Stoller, M.B. Toloczko, G.S. Was, A.G. Certain, S. Dwaraknath, and F.A. Garner. On the use of srim for computing radiation damage exposure. *Nuclear Instruments and Methods in Physics Research B*, 310:75–80, 2013.

[64] K. Mo, Z. Zhou, Y. Miao, D. Yun, H.-M. Tung, G. Zhang, W. Chen, J. Almer, and J.F. Stubbins. Synchrotron study on load partitioning between ferrite/martensite and nanoparticles of a 9cr ods steel. *Journal of Nuclear Materials*, 455:376–381, 2014.

[65] Y. Miao, K. Mo, Z. Zhou, X. Liu, K.-C. Lan, G. Zhang, M.K. Miller, K.A. Powers, J. Almer, and J.F. Stubbins. In situ synchrotron tensile investigations

on the phase responses within an oxide dispersion-strengthened (ods) 304 steel. *Materials Science & Engineering A*, 625:146–152, 2015.

[66] P. Dubuisson, D. Gilbon, and J.L. Séran. Microstructural evolution of ferritic-martensitic steels irradiated in the fast breeder reactor phénix. *Journal of Nuclear Materials*, 205:178–189, 1993.

[67] F.A. Garner, L. Shao, M.B. Toloczko, S.A. Maloy, and V.N. Voyevodin. Use of self-ion bombardment to study void swelling in advanced radiation-resistant alloys. In *17th International conference on environmental degradation of materials in nuclear power systems - water reactors*, Aug 2015.

[68] S. Ohtsuka, S. Ukai, M. Fujiwara, T. Kaito, and T. Narita. Improvement of creep strength of 9crods martensitic steel by controlling excess oxygen and titanium concentrations. *Materials Transactions*, 46(3):487–492, 2005.

[69] J. Gan, T.R. Allen, B.C. Birtcher, S. Shutthanandan, and S. Thevuthasan. Radiation effects on the microstructure of a 9cr-ods alloy. *JOM*, 60:24–28, 2008.

[70] B.H. Sencer and F.A. Garner. Compositional and temperature dependence of void swelling in model fe-cr base alloys irradiated in the ebr-ii fast reactor. *Journal of Nuclear Materials*, 283-287:164–168, 2000.

[71] A.M. Dvoriashin, S.I. Porollo, Yu. V. Konobeev, and F.A. Garner. Influence of high dose neutron irradiation on microstructure of ep-450 ferritic-martensitic steel irradiated in three russian fast reactors. *Journal of Nuclear Materials*, 329-333:319–323, 2004.

[72] M. Song, Y. Wu, D. Chen, X. Wang, C. Sun, K.Y. Yu, Y. Chen, L. Shao, Y. Yang, K.T. Hartwig, and X. Zhang. Response of equal channel angular

extrusion processed ultrafine-grained t91 steel subjected to high temperature heavy ion irradiation. *Acta Materialia*, 74:285–295, 2014.

[73] M. Song, C. Sun, J. Jang, C.H. Han, T.K. Kim, K.T. Hartwig, and X. Zhang. Microstructure refinement and strengthening mechanisms of a 12cr ods steel processed by equal channel angular extrusion. *Journal of Alloys and Compounds*, 577:247–256, 2013.

[74] A.O.F. Hayama, H.R.Z. Sandim, J.F.C. Lins, M.F. Hupalo, and A.F. Padilha. Annealing behavior of the ods nickel-based superalloy pm 1000. *Materials Science & Engineering A*, 371:198–209, 2004.

[75] Y. Chen, L. Jiao, C. Sun, M. Song, K.Y. Yu, Y. Liu, M. Kirk, M. Li, H. Wang, and X. Zhang. In situ studies of radiation induced crystallization in fe/$\alpha - y_2o_3$ nanolayers. *Journal of Nuclear Materials*, 452:321–327, 2014.

[76] K.C. Russell. Phase instability under cascade damage irradiation. *Journal of Nuclear Materials*, 206:129–138, 1993.

[77] F.A. Garner. Chapter 6 "irradiation performance of cladding and structural steels in liquid metal reactors". volume 10A, pages 419–543. Materials Science and Technology: A Comprehensive Treatment, VCH Publishers, 1994.

[78] D.S. Gelles. Microstructural examination of commercial ferritic alloys at 200 dpa. *Journal of Nuclear Materials*, 233-237:293–298, 1996.

[79] P.J. Maziasz, R.L. Klueh, and J.M. Vitek. Helium effects on void formation in 9cr-1movnb and 12cr-1movw irradiated in hfir. *Journal of Nuclear Materials*, 141-143:929–937, 1986.

[80] O. Anderoglu, J. Van den Bosch, P. Hosemann, E. Stergar, B.H. Sencer, D. Bhattacharyya, R. Dickerson, P. Dickerson, M. Hartl, and S.A. Maloy. Phase stability

of an ht-9 duct irradiated in fftf. *Journal of Nuclear Materials*, 430:194–204, 2012.

[81] Y. Miao, K. Mo, B. Cui, W.Y. Chen, M.K. Miller, K.A. Powers, V. McCreary, D. Gross, J. Almer, I.M. Robertson, and J.F. Stubbins. The interfactial orientation relationship of oxide nanoparticles in a hafnium-containing oxide dispersion-strengthened austenitic stainless steel. *Materials Characterization*, 101:136–143, 2015.

[82] P. Dou, A. Kimura, T. Okuda, M. Inoue, S. Ukai, S. Ohnuki, T. Fujisawa, and F. Abe. Effects of extrusion temperature on the nano-mesoscopic structure and mechanical properties of an al-alloyed high-cr ods ferritic steel. *Journal of Nuclear Materials*, 417:166–170, 2011.

[83] X. Mao, K.H. Oh, S.H. Kang, T.K. Kim, and J. Jang. On the coherency of y2ti2o7 particles with austenitic matrix of oxide dispersion strengthened steel. *Acta Materialia*, 89:141–152, 2015.

[84] D.A. Porter, K.E. Easterling, and M.Y. Sherif. *Phase transformations in metals and alloys*. CRC Press, 3rd edition, 2006.

[85] S. Ukai and M. Fujiwara. Perspective of ods alloys application in nuclear environments. *Journal of Nuclear Materials*, 307-311:749–757, 2002.

[86] S. Ukai, T. Okuda, M. Fujiwara, T. Kobayashi, S. Mizuta, and H. Nakashima. Characterization of high temperature creep properties in recrystallized 12cr–ods ferritic steel claddings. *Journal of NUCLEAR SCIENCE and TECHNOLOGY*, 39(8):872–879, 2002.

[87] P. Susila, D. Sturm, M. Heilmaier, B.S. Murty, and V. Subramanya Sarma. Effect of yttria particle size on the microstructure and compression creep properties

of nanostructured oxide dispersion strengthened ferritic (fe–12cr–2w–0.5y2o3) alloy. *Materials Science & Engineering A*, 528:4597–4584, 2011.

[88] N. Dudova, A. Plotnikova, D. Molodov, A. Belyakov, and R. Kaibyshev. Structural changes of tempered martensitic 9during creep at 650 c. *Materials Science & Engineering A*, 534:632–639, 2012.

[89] M. Mujahid and J.W. Martin. The effect of oxide particle coherency on zener pinning in ods superalloys. *Journal of Materials Science Letters*, 13:153–155, 1994.

[90] K.C. Russell. Phase instability under irradiation. *Progress in Materials Science*, 28:229–434, 1984.

[91] J.D. Robson. Modelling the overlap of nucleation, growth and coarsening during precipitation. *Acta Materialia*, 52:4669–4676, 2004.

[92] C. Hin and B.D. Wirth. Formation of y2o3 nanoclusters in nano-structured ferritic alloys: modeling of precipitation kinetics and yield strength. *Journal of Nuclear Materials*, pages 30–37, 2010.

[93] M. Perez. Gibbs–thomson effects in phase transformations. *Scripta METALLURGICA*, 52:709–712, 2005.

[94] H. Okamoto. Comment of fe-y (iron-yttrium). *Journal of Phase Equilibria*, 16:473–473, 1995.

[95] J. Ribis and Y. de Carlan. Interfacial strained structure and orientation relationships of the nanosized oxide particles deduced from elasticity-driven morphology in oxide dispersion strengthened materials. *Acta Materialia*, 60:238–252, 2012.

[96] J.M. Howe. *Interfaces in materials*. Wiley-Interscience, 1997.

# APPENDIX A

## PROCEDURE OF FIB LIFT-OUT FROM F/M STEEL USING LYRA FIB-SEM

This document serves as a general procedure of TEM specimen lift-out using TESCAN LYRA FIB-SEM on F/M steels.

1. Vent the chamber.

2. Load samples and TEM grid. The surface of the sample should be aligned with the TEM grid. When mounting the sample, the region of interests, where the TEM specimen will be lifted from, should be put closer to the edge of the sample stage.

3. Pump the chamber.

4. Confirm the nano-manipulator is in a usable condition. Set work-position of the nano-manipulator slightly higher than 9mm.

5. Find a region on the sample to carry out the lift-out. Adjust the stage so that the region is in eccentric height.

6. Tilt the stage to 55 degree so that the surface of the sample is perpendicular to the ion beam.

7. Insert the platinum(Pt) gas-injection-system(GIS). Deposit a protection layer of Pt in the region of interests, using 30 keV ion beam of $\sim$0.2 nA. The thickness of the protection layer is usually $\sim$2 microns, as shown in Fig. A.1a.

8. Put GIS back to home position.

9. Make two trenches around the protection layer, using 30 keV ion beam of a current of 7-15 nA, as shown in Fig. A.1b.

10. Polish the surface of the trench until the thickness of the lamella is between 1-3 microns, using 30 keV ion beam of a current of $\sim$1-3 nA, as shown in Fig. A.1c.

11. Tilt stage back to 0 degree so that the surface of the sample is perpendicular to

the electron beam.

12. Cut the lamella off the bulk, with a connection to the right of the lamella left, using 30 keV ion beam of a current of ∼2-3 nA, as shown in Fig. A.1d.

13. Tilt the stage to 55 degree. Recall the Pt GIS and the nano-manipulator. Approach the tip of nano-manipulator to the left-top of the lamella without touching it.

14. Deposit Pt to wield the tip of nano-manipulator with the lamella using 30 keV ion beam of ∼0.2 nA, as shown in Fig. A.1e.

15. Using 30 keV ion beam of ∼2-3 nA to cut the bridge to the right of the lamella, so that the lamella is completely off the bulk, as shown in Fig. A.1f.

16. Lift out the lamella in y direction until the lamella is completely out of the trench, as shown in Fig. A.1g. Then move the nano-manipulator in z direction until it is ∼0.5 mm above the eccentric point. Send the Pt GIS back to home position.

17. Move the stage to the TEM sample grid. Bring down the nano-manipulator and approach the lamella to one side of one of the poles on the TEM grid, as shown in Fig. A.1h.

18. Recall the Pt GIS, wield the lamella to the TEM grid with 30 keV ion beam of ∼0.2 nA, as shown in Fig. A.1i.

19. Send nano-manipulator to parking position; send GIS to home position. At this time, the lamella is mounted onto the TEM grid as shown in Fig. A.1j.

20. Start polishing lamella at a glancing angle of ±2 degrees. Start with beam current around ∼1 nA until lamella is thinned to 1000 nm. Then reduce the beam current to ∼0.5 nA before the lamella reaches to 500 nm. Reduce the beam current to ∼0.2 nA to thin the lamella down to 100 nm, as shown in Fig. A.1k.

21. Reduce the energy of ion beam to 5 keV, using ∼50 pA current to thin the lamella at a glancing angle of ±7 degrees, until the lamella appears to be electron

transparent. The lamella would look like glowing when secondary electrons generated by 10 keV electron beam were used to image, as shown in Fig. A.1l.

22. Reduce the energy of ion beam to 2 keV, using ∼20 pA to clean ion damage of both sides of the lamella at a glancing angle of ±7 degrees.

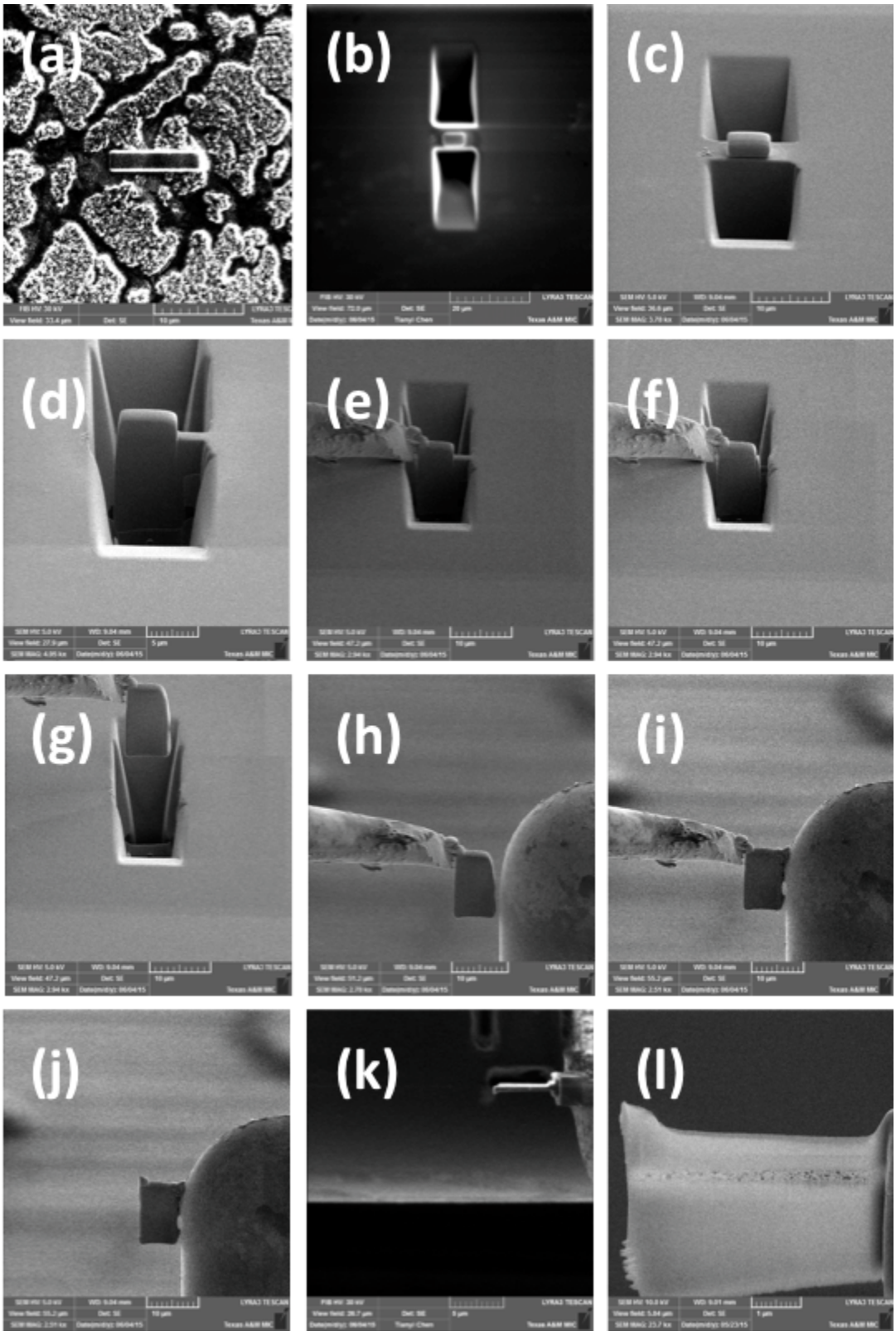


Figure A.1: Procedure of TEM specimen preparation using FIB lift-out technique